FCTUC DEPARTAMENTO DE CIÊNCIAS DA TERRA
FACULDADE DE CIÊNCIAS E TECNOLOGIA
UNIVERSIDADE DE COIMBRA

MARS PALEOTECTONIC CHARACTERIZATION USING AUTOMATIC IMAGE RECOGNITION TECHNIQUES

David Alegre Vaz

Orientador: Prof. Doutor Eduardo Ivo Cruzes do Paço Ribeiro Alves
Co-orientador: Prof. Doutor Luís Carlos Gama Pereira

Trabalho desenvolvido com o apoio de:

CGUC CENTRO DE GEOFÍSICA UNIVERSIDADE DE COIMBRA

IRSPS

FCT Fundação para a Ciência e a Tecnologia
MINISTÉRIO DA CIÊNCIA, TECNOLOGIA E ENSINO SUPERIOR

Coimbra 2010

“What we know is not much. What we do not know is immense.”

Pierre-Simon Laplace (1749-1827)

Contents

Resumo

É descrita uma nova metodologia semi-automática que permite a cartografia e caracterização automática de estruturas tectónicas na superfície de Marte. Os resultados desta cartografia foram comparados qualitativamente e quantitativamente com duas fotointerpretações tectónico-estruturais da superfície de Marte.

Esta comparação permitiu identificar alguns dos factores que podem influenciar o processo de fotointerpretação em Marte. A referida comparação permitiu ainda avaliar e validar os resultados obtidos utilizando a técnica semi-automática desenvolvida. A metodologia proposta provou ser essencialmente dependente da qualidade dos dados, sendo no entanto capaz de produzir bons resultados, mesmo com os dados altimétricos MOLA (Mars Orbiter Laser Altimeter).

A metodologia foi inicialmente testada num pequeno rift situado em Thaumasia Planum, permitindo uma segmentação e caracterização desse conjunto de estruturas tectónicas. Concluiu-se que o rift é composto por várias bacias de *pull-apart*, que se desenvolveram devido à reactivação de outras estruturas tectónicas anteriormente formadas. A geometria e distribuição espacial da deformação são compatíveis com uma zona de cisalhamento esquerda, aproximadamente Este-Oeste correspondente a uma zona de transferência entre dois blocos litosféricos distintos.

A aplicação das metodologias desenvolvidas numa região mais vasta, permitiu dar uma nova perspectiva evolutiva, focada nas relações entre os processos tectónicos e a actividade hidrológica no bordo oriental do Planalto de Thaumasia. A caracterização morfométrica apresentada, permitiu estabelecer uma segmentação mais detalhada de parte da cadeia montanhosa de Thaumasia Highlands/Coprates Rise: a zona de transferência de Melas Fossae/Protva Valles, aparenta ser uma estrutura de primeira ordem que separa um sector mais evoluído a Norte de um sector compressivo menos evoluído a Sul. Em ambos os sectores, as estruturas tectónicas identificadas apontam para uma fase inicial de um processo orogénico. Apresenta-se ainda um modelo evolutivo para o bordo oriental da região de Thaumasia.

Palavras chave: Cartografia automática de lineamentos; Quantificação das deformações tectónicas; Marte; Planalto de Thaumasia.

Abstract

A new semi-automatic technique is introduced to map and characterize tectonic features on Mars. The procedure results were compared qualitatively and quantitatively with two photogeologic-based interpretations. Some of the factors that can influence the process of lineament mapping on Mars were identified. Comparing the human mapped datasets with the semi-automatically mapped features allowed evaluating the accurateness of the semi-automatic mapping procedure. The developed semi-automatic mapping methodology proved to be mainly dependent on data quality; nevertheless, when applied to MOLA (Mars Orbiter Laser Altimeter) data, the methodology is able to produce meaningful results.

The application of this new technique to a small rift located in Thaumasia Planum allowed the segmentation and characterization of the rift. The rift is formed by several pull-apart basins developed due to the reactivation of previously formed tectonic structures. The strain spatial distribution and the overall geometry are consistent with a roughly East-West left-lateral shear transfer zone between two different lithospheric blocks.

A new perspective on the evolution of the Eastern border of the Thaumasia Plateau was given by the application of the developed tools. Clear evidences of the interplay between tectonic processes and hydrologic activity were found. The presented morphometric characterization helped to establish a more precise along-arch segmentation of part of the Thaumasia Highlands/Coprates Rise belt: the Melas Fossae/Protva Valles transfer zone seems to be a first order structure which separates a more mature sector in the North of a more undeveloped compressive structure in the South. The general structure in both areas is nevertheless more akin to an initial stage of orogenic evolution. Finally, a more detailed evolutionary scheme for the region was proposed.

Keywords: Automatic lineament mapping; Tectonic strain quantification; Mars; Thaumasia Plateau.

Agradecimentos

É com grande satisfação que vejo surgir a oportunidade de agradecer a todos aqueles que directa ou indirectamente contribuíram para este trabalho. A elaboração da tese que agora se apresenta não seria possível sem a colaboração de várias pessoas e instituições, cujo contributo foi indispensável durante os anos de trabalho que conduziram a esta dissertação.

Ao Professor Doutor Eduardo Ivo Cruzes do Paço Ribeiro Alves, o agradecimento pela orientação deste trabalho, a total disponibilidade que sempre demonstrou e as palavras de motivação que sempre me dispensou. Agradeço ao Professor Doutor Luís Carlos Gama Pereira o tempo que disponibilizou na orientação e as profícuas discussões que contribuíram para a realização deste trabalho. A companhia e assistência quase diária da Professora Doutora Maria Teresa de Abrunhosa Barata constituíram também uma ajuda preciosa

Aos três agradeço ainda a revisão do manuscrito inicial, cujas sugestões e criticas, ajudaram a melhorar.

De referir a total cooperação do Professor Doutor Gian Gabriele Ori, que me recebeu nas várias temporadas que passei em Pescara. Nessas estadias sempre recebi o melhor apoio possível, não só material mas também humano, de todos os que me acolheram: Simone Silvesto, Luca Guallini, Gaetano Di Achille (a quem agradeço os dados fornecidos), Marco Cardinale, Monica Pondrelli, Goro Komatsu, Lucia Marinangeli, Ida Dell'Arciprete, Stefania Celenza, Daniela D'Alleva. Para além destas relações de cariz mais profissional, a amizade e o auxílio do Mateo e do Edoardo fizeram com que me sentisse já em casa de cada vez que voltava a Itália.

Agradeço aos funcionários do Instituto Geofísico que sempre se mostraram disponíveis a ajudar no que fosse necessário, em especial ao Paulo pelo companheirismo e partilha de ideias. Agradece-se o apoio dado nos primeiros anos pela Rita Baptista e pela Vera Fernandes, aquando das suas passagens pelo Instituto.

Agradece-se à Fundação para a Ciência e Tecnologia o apoio financeiro que permitiu a execução do plano de trabalhos proposto. Expresso ainda gratidão pelo apoio e condições disponibilizadas pelo Centro de Geofísica da UC e pelo IRSPS.

Por último, mas não menos importante, agradeço aos meus pais, à minha família e à Ana pelo apoio incondicional ao longo de todos estes anos.

List of acronyms

MOLA	Mars Orbiter Laser Altimeter
DTM	Digital Terrain Model
HRSC	High Resolution Stereo Camera
MRO	Mars Reconnaissance Orbiter
CTX	Context Camera
HiRISE	High Resolution Imaging Science Experiment
THEMIS	Thermal Emission Imaging System
SE	Structuring Element
PMMG	Parametric Morphological Multiscale Gradient
NPMMG	Non-Parametric Multiscale Morphological Gradient
CWT	Continuous Wavelet Transform
WTMM	Wavelet Transform Modulus Maxima
GIS	Geographical Information System
D-L	Displacement-Length
NF	Normal Fault
WR	Wrinkle Ridge
MDIM 2.1	Mars Digital Image Model
IR	Infrared
LD	Line Density
LLD	Line Length Density

List of symbols

Morphological operators

$\cap$	Boolean intersection
$\cup$	Boolean union
$\vee$	Point-wise maximum
ε	Erosion operator
δ	Dilation operator
γ	Opening
ϕ	Closing
ρ	Morphological gradient
R^{δ}	Morphological reconstruction by dilatation
ρ_n^*	Parameterized multiscale morphological gradient a scale *n*
ρ^*	Non-parametric multiscale morphological gradient
WTH	White top-hat
T	Threshold operator
$DBLT$	Double (hysteresis) threshold operator
SK	Skeleton
$FILL$	Fillhole operator
$PRUNE$	Prune operator

Circular statistics

$\overline{\sigma}$	Mean azimuth
$\overline{k}$	Von Mises concentration parameter maximum-likelihood estimator
V	Circular variance

Others

oa	Overall accuracy
$\hat{k}$	Kappa index
σ_1	Principal compressive stress

Equation index

Figure index

Table index

1 Introduction

Mars formed, as the rest of the Solar System, ~4.5 Ga ago. Since then a complex evolution shaped its surface through impact cratering, intense volcanism, tectonic and erosional processes.

Today's Mars atmosphere is thin, water in liquid form is not stable at the surface and active volcanic and tectonic activity is believed to be inexistent. Geomorphologic evidences tell a very different story about ancient Mars. An active hydrosphere existed during part of Mars history, producing extensive valley networks, outflow channels, lakes, deltas and possibly an ocean in the northern plains (Parker et al., 1993; Mangold and Ansan, 2006; Di Achille and Hynek, 2010).

Three main global stratigraphic units were defined based on crater densities studies (Hartmann and Neukum, 2001). The Noachian period ended 3.5 Ga ago and was characterized by intense impact rates that produce much of the cratered South highlands. The Hesperian epoch, ended 1.8 Ga ago, and is mainly associated with the formation of most of the Northern plains and the main volcanic provinces. Terrains of Amazonian age are much less craterized and are related with the more recently formed units.

Bibring *et al.* (2006) presented an alternative stratigraphy based on mineralogical evidences. The first period, named Phyllocian, lasted until 4 Ga ago and is characterized by the occurrence of phyllosilicates formed in a water rich environment. The second period corresponds to the Theiikian, a period characterized by acidic conditions with the formation of sulfates. This period ended 3.5 years ago with the beginning of the Siderikian. During this period water was no longer available and anhydrous ferric oxides formed.

One of the most prominent features on Mars surface is the hemispheric dichotomy existent between the highly cratered South highlands and the North lowland plains (see topographic map in Figure 1.1). The nature of this dichotomy is still debated and some of the advanced explanations are: large impacts (Frey *et al.*, 2002), crust thinning due to mantle upwelling (Wenzel *et al.*, 2004) and even plate tectonics (Sleep, 1994).

During the first 500 Ma an active core dynamo produced strong remnant crustal magnetic anomalies (Acuña et al., 1999). Those anomalies form large E-W stripes with alternating polarities. This pattern of stripes has been compared with the magnetic anomalies associated with the formation of oceanic crust (Connerney et al., 2001; Connerney et al., 2005), which imply a plate tectonic event early in the planet's history. Another hypothesis, that also requires plate mobility in ancient Mars, is the one proposed by Fairén *et al.* (2002), that relates the formation of the anomalies with a terrain accretion process. Since strong photogeologic evidences that support those hypothesis were not yet found, other formation mechanism were advanced to explain the formation of the magnetic anomalies: magnetization by a monopolarity dipole followed by partial demagnetization associated with volcanism and hidrotermalism (Sprenke and Baker, 2000); dike intrusion (Nimmo, 2000) and more recently, the anomalies were associated with hot spot tracks linked with a possible lithospheric drift (Kobayashi and Sprenke, 2010).

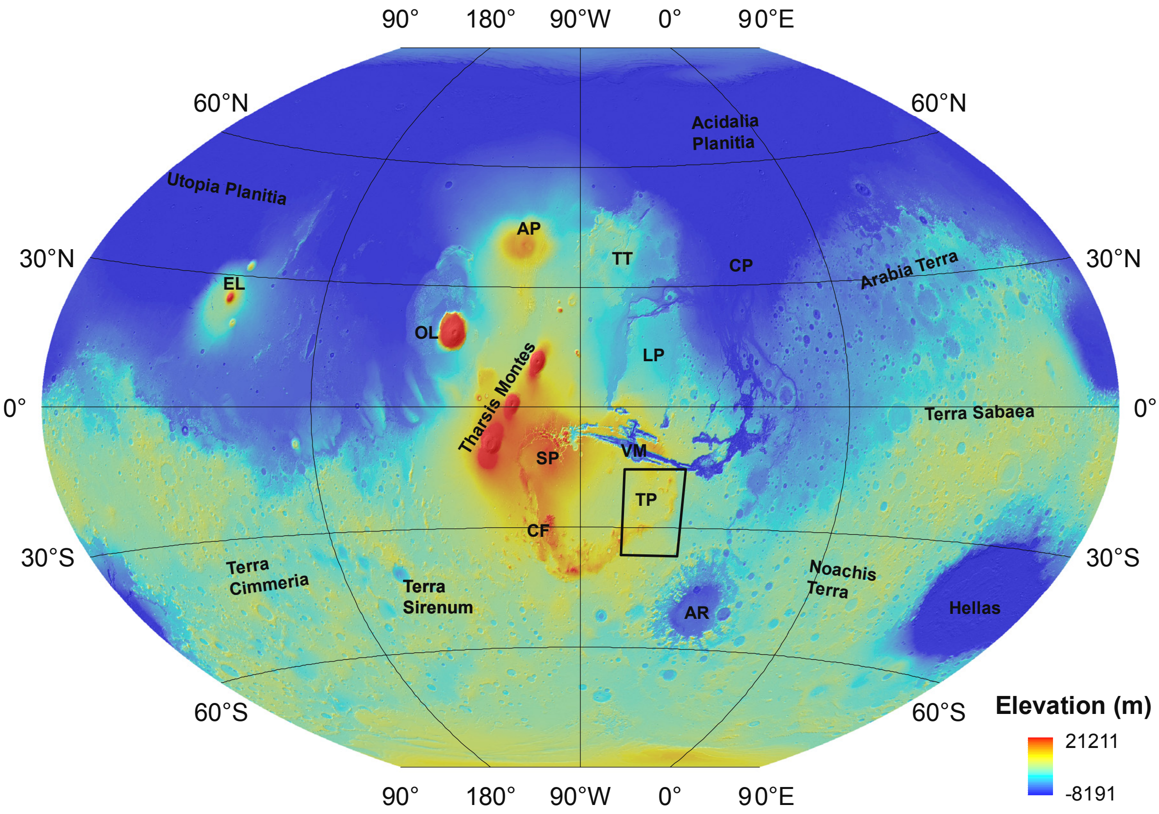

Figure 1.1 - Tharsis centered Mars topographic map with some of the key structures and provinces labeled: EL – Elysium Mons, OL – Olympus Mons, AP – Alba Patera, TT – Tempe Terra, SP – Syria Planum, CF – Claritas Fossae, VM – Vallis Marineris, TP – Thaumasia Planum, LP – Lunae Planum, AR – Argyre, LP – Chryse Planitia. The framed area of Thaumasia Planum will be analyzed in this dissertation. Excluding this map, which was built using a Winkel III projection, the remaining maps in this work were made using a Mercator projection.

Tharsis is a volcanic province with some of the largest volcanic edifices in the Solar System. The formation of Tharsis initiated during the Noachian and spans great part of Mars history. It forms a large topographic bulge (Figure 1.1) that controlled the formation of many of the tectonic structures that develop within and in the periphery of the region (Anderson et al., 2001).

1.1 Tectonic background

A well developed plate tectonics regime, with creation and subduction of crust in divergent and convergent plate boundaries, is not evident on Mars (Solomon et al., 2005). Sleep (1994) proposed a model involving several plates and a plate tectonics regime, but photogeologic evidences do not support that model. Nevertheless, a rich array of tectonic structures is widespread through the surface. Several rift systems cut large areas and pervasive compressive structures, essentially under the form of wrinkle ridges, are present over large portions of the crust.

Tharsis and Elysium regions concentrate must of the tectonic and volcanic activity on Mars. Tharsis tectonic structures are mostly arranged in radiating sets of grabens and concentric sets of compressive wrinkle ridges. Several centers of tectonic activity on Tharsis have been identified by Anderson *et al.* (2001) relying on statistical analysis of mapped tectonic structures to test a radial distribution of the underlying stresses. The same procedure, applied to the Eastern hemisphere, allowed the identification of other four centers located nearby Elysium and Utopia Planitia (Anderson et al., 2008). Those results arise from the structural mapping of tens of thousands of tectonic structures, and from the assumptions that stresses were perpendicular to compressive structures and parallel to distensive structures, in a pure shear scenario.

Remote stresses related with isostatic forces, flexural uplift and lithospheric loading due to the volcanic activity related with Tharsis formation are the most invoked mechanisms to explain the observed tectonic structures on Tharsis (Banerdt et al., 1982; Solomon and Head, 1982; Schultz and Tanaka, 1994; Mège and Masson, 1996). The identification of several transcurrent structures South of Vallis Marineris by Anguita *et al.* (2001) resulted in a more complex model, involving lithospheric horizontal mobility and a phase of thick-skinned tectonics during the Noachian, followed by thin-skinned style of deformation during the Amazonian.

A differential block movement in a context of a Noachian-Hesperian orogeny as been later proposed for explaining the complex tectonic assemblage of the Thaumasia highlands (Anguita et al., 2006). Montgomery et al. (2009) linked the evolution of this province with a possible weak salt basement detachment, responsible for the sliding of the Thaumasia block.

1.2 Motivation

Any Mars paleotectonic study relies on the mapping and characterization of the tectonic structure existent on the surface. This mapping has been traditionally made manually, through the photogeologic interpretation of satellite imagery. This is a time consuming process, potentially subjective and until now only capable of a two dimensional analysis, not taking full advantage of the excellent topographic datasets existent for the planet.

The most important contribution of this work is the establishment of a new semi-automatic procedure that introduces an integrated framework for the mapping and analysis of large portions of the planet. The proposed methodology relies on several image analysis techniques and besides the mapping, comparable to the mapping obtained by the traditional method, allows a full morphometric characterization of any kind of scarp on the surface. This step-forward corresponds to the general idea of passing from a classic two dimensional analysis, to the inclusion of a third dimension attached to the mapped features as morphometric parameters. Several practical applications of this idea are presented. The automatic strain estimation associated with the more abundant kinds of tectonic structures on Mars (normal faults and wrinkle ridges) is perhaps the more interesting, since they are methodologies easily applied to large areas, and that numerically characterize the paleo-strains on Mars.

All the described methodologies use as input MOLA altimetry data. Despite the limited spatial resolution that can be obtained from this dataset, it remains the only dataset that covers the entire surface, with high accuracy and almost constant quality. Other elevation sources exist with better spatial resolutions, namely the altimetry derived by stereophotoclinometry. Those datasets offer a more detailed view of the surface, but lack until the moment a uniform good coverage of large areas, the main factor that induced the development of the automatic mapping and characterization tools. All the presented analysis was made using MOLA data but there are not technical restrictions, besides data quality, for the analysis of other topographic datasets using the same methodologies.

The East Thaumasia plateau region was used during this work as a workbench for developing, testing and applying the set of developed tools. The choice of this area can be justified with technical and scientific arguments.

Technically, since MOLA data quality decreases with latitude, a low latitude area was preferred so that the methodologies were tested in the worst possible scenario. The presence of a varied arrangement of tectonic structures, distensive as well as compressive, was also a key element for choosing that area.

The Thaumasia plateau has focused much of the tectonic investigations on Mars in recent years. Several models, supported by different mappings, were proposed for the evolution of this plateau. Important horizontal movements and large scale thrusting/buckling are the most puzzling elements recognized in the region. Those tectonic signatures tend to approach Mars and Earth tectonics, and terms as "lithospheric block" or "plate" are now being used to describe the evolution of this province.

1.3 Dissertation structure

The dissertation is divided in three main chapters. In chapter 2 the mapping procedure is introduced and the automatic normal strain estimation technique is presented, validated and applied to a concrete case. This led to the proposal of a new tectonic model to explain the observed strains and fault patterns on a small rift located North of Thaumasia Planum.

In chapter 3, the mapping results are compared with two published photo-interpretations, so that the algorithm accuracy is assessed and some of the weaknesses of the traditional photogeologic approach are highlighted.

Finally, a full analysis of the mapped structures on the East Thaumasia highlands is presented in chapter 4. The compressive strains associated with the wrinkle ridge formation are deeply analyzed through the introduction of a new methodology: the implementation of an automatic procedure to analyze the strains associated with wrinkle ridges. The importance of the recognition of the sense of horizontal shear associated with oblique tectonic structures, related with a simple shear style of deformation, is investigated. A close relation between the hydrologic flow patterns and the tectonic evolution of the region is shown. The objective of this chapter is to demonstrate the potentialities of the developed framework, as an integrated way to perform planetary mapping.

Each of the referred chapters follows a same generic intern structure, with a detailed introduction, methodology/results, discussion and conclusion. It is hoped that this segmentation helps the reader by keeping close to each other introductory material and conclusions for each topic/chapter. A final summary with the main achievements is presented in chapter 5 and hints for further work are portrayed in chapter 6.

2 Analysis of a Thaumasia Planum rift through automatic mapping and strain characterization

2.1 Introduction

Imagery datasets constitute the basis for tectonic studies on Mars. Tectonic lineaments are usually mapped and classified manually according to their structural significance (Anderson et al., 2001; Bistacchia et al., 2004; Borraccini et al., 2007; Fernández and Anguita, 2007). Several factors can influence the results of this tectonic analysis. Physical factors such as data spatial resolution, illumination conditions or the use of imagery from different sensors can potentially lead to different photointerpretations.

The arduous and tedious work of lineament mapping is also dependent on the experience and personal style of the interpreter. A good example of the importance of those factors can be seen when comparing Hauber and Kronberg (2001) Tempe Fossae Rift structural map with the more recent map by Fernández and Anguita (2007). Both interpretations were made using Viking imagery with similar spatial resolutions. In the first case, the authors had chosen to make a more schematic interpretation, mapping only the major structures which greatly improve the interpretability of their map. Fernández and Anguita (2007) performed a more exhaustive mapping of the fault scarps, which in some cases produced an excess of lineaments that hinder the visualization of the tectonic pattern. This example illustrates the concept of scale dependence. Despite similar spatial resolution of the data, a different scale of analysis is an important factor that can influence the interpretations.

More important than these differences in style are the very different interpretations derived from both maps of the Tempe Rift. Fernández and Anguita (2007) proposed an oblique rift model in opposition with the continental rift model related with the uprise of a small mantellic plume proposed by Hauber and Kronberg (2001).

On the Earth the task of lineament mapping is also considered a subjective task (Wise, 1982) but several automatic approaches have been developed (Oakey, 1994; Koike et al., 1998; Tripathi et al., 2000; Argialas and Mavrantza, 2004; Masoud and

Koike, 2006) and human and physical factors that can influence the final results have also been studied (Podwysocki et al., 1975; Smith and Wise, 2007).

Imagery is important for mapping tectonic features but topographic data have been widely used for the characterization of these structures. Topographic data allowed the estimation of strains (Mège and Masson, 1996; Borraccini et al., 2005; Colton et al., 2006) and modeling (Watters, 2004; Masoud and Koike, 2006) of the different tectonic structures.

Several automatic methodologies have been applied on Mars for studying several geomorphologic features using remote sensing data. Terrain classification (Bue and Stepinski, 2006), drainage networks mapping (Stepinski and Collier, 2004) and crater counting (Bandeira et al., 2007; Bue and Stepinski, 2007) are some of the automated tasks. An automatic method for lineament extraction from MOLA (Mars Orbiter Laser Altimeter) data has been previously outlined (Vaz et al., 2007; Alves et al., 2008; Vaz et al., 2008). Since then several improvements have been implemented, such as classification and morphometric characterization of the identified lineaments, which conducted to a new automatic method of strain estimation for distensive structures that will be presented in this chapter.

The automatic lineament mapping algorithm will be described and strain estimation derived from the mapping results is presented. A detailed strain analysis of a Thaumasia Planum rift is performed.

2.2 Geological and tectonic background

The Thaumasia Planum region is formed by older ridged plain materials (unit *HNr*) of Noachian to Early Hesperian age (Dohm and Tanaka, 1999; Dohm *et al.*, 2001b). It is located in the eastern part of the Thaumasia Plateau, between Melas Dorsa and Coprates rise (Figure 2.1).

The tectonic evolution of the Thaumasia Plateau has been widely debated. Schultz and Tanaka (1994) recognized the compressive nature of the South Tharsis region and Dohm and Tanaka (1999) held that the plateau resembles the structural style of Earth intra-continental plateaus with large-scale anticlines forming the marginal ancient highlands. A thick-skinned followed by a thin-skinned episodes were proposed by Anguita *et al.* (2001) in a scenario where the Thaumasia Plateau slides as part of an independent lithospheric block. The idea of a Noachian-Hesperian orogeny, with the outer highlands acting as thrusts was later introduced by Anguita *et al.* (2006). A differential movement between two Thaumasia subunits was proposed. A southern unit thrusting to the South (forming the Southern Highlands) and a Northern unit thrusting to the East along the Coprates rise.

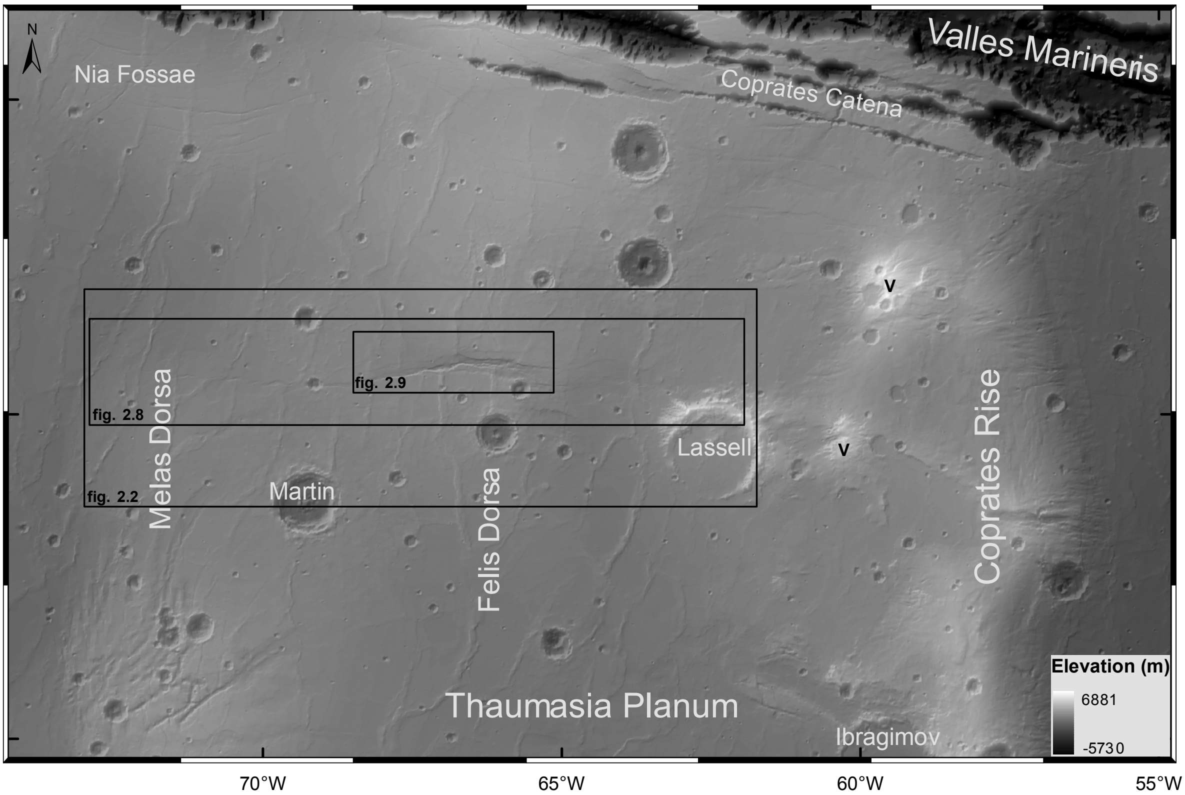

Figure 2.1 - Shaded relief topography of the studied area. Two degraded volcanic cones are marked with (V).

Topographic loading is usually invoked as a mechanism to explain the Thaumasia block ESE sliding and Montgomery *et al.* (2009) suggested the existence of a continental-scale basal detachment related with salts or salt-rich deposits.

The area analyzed in this work corresponds to a small rift system, comprised between Melas Dorsa and Lassell crater (Figure 2.1), an area characterized by ~EW grabens that cut pre-existent ~NS wrinkle ridges (Figure 2.2). The oblique nature of this rift is particularly evident in the western part, where grabens present en-echelon geometries denoting a clear transtensive regime related with an EW sinistral shear zone (Borraccini et al., 2007).

The rift is sub-parallel to Valles Marineris and it has been proposed that during Early Hesperian those structures acted as left-lateral transfer zones accommodating differential movements of the Thaumasia Plateau (Webb and Head, 2002; Borraccini et al., 2007). More recently this tectonic array has been interpreted by Montgomery *et al.* (2009) as a boundary between the main Thaumasia block and another smaller "plate" named Thaumasia Minor. The sinistral transtensional regime was also recognized in the western part of the rift and a possible transpresional regime was proposed to exist in the eastern section of the rift.

2.3 Data

The use of altimetry data for mapping geomorphologic structures allows a morphometric characterization that imagery alone cannot provide and has also the advantage of avoiding possible biases related with illumination conditions. Two main sources of topographic data are available for Mars: digital terrain models (DTMs) derived from stereophotogrammetry and MOLA laser altimetry (Zuber et al., 1992).

Stereo DTMs are mainly obtained from imagery acquired by the High Resolution Stereo Camera (HRSC) (Neukum et al., 2004) and the two cameras aboard Mars Reconnaissance Orbiter: Context Camera (CTX) (Malin et al., 2007) and High Resolution Imaging Science Experiment (HiRISE) (McEwen et al., 2007). The resolution and quality of the stereo DTMs can change according to acquisition conditions and even with the stereo matching algorithms used (Heipke et al., 2007).

Despite the better spatial resolution of stereo-derived DTMs (Kim and Muller, 2009), MOLA data coverage is still more complete and consistent, making it ideal for regional mapping. Integration of both kinds of datasets through data fusion seems a promising technique (Lin et al., 2010).

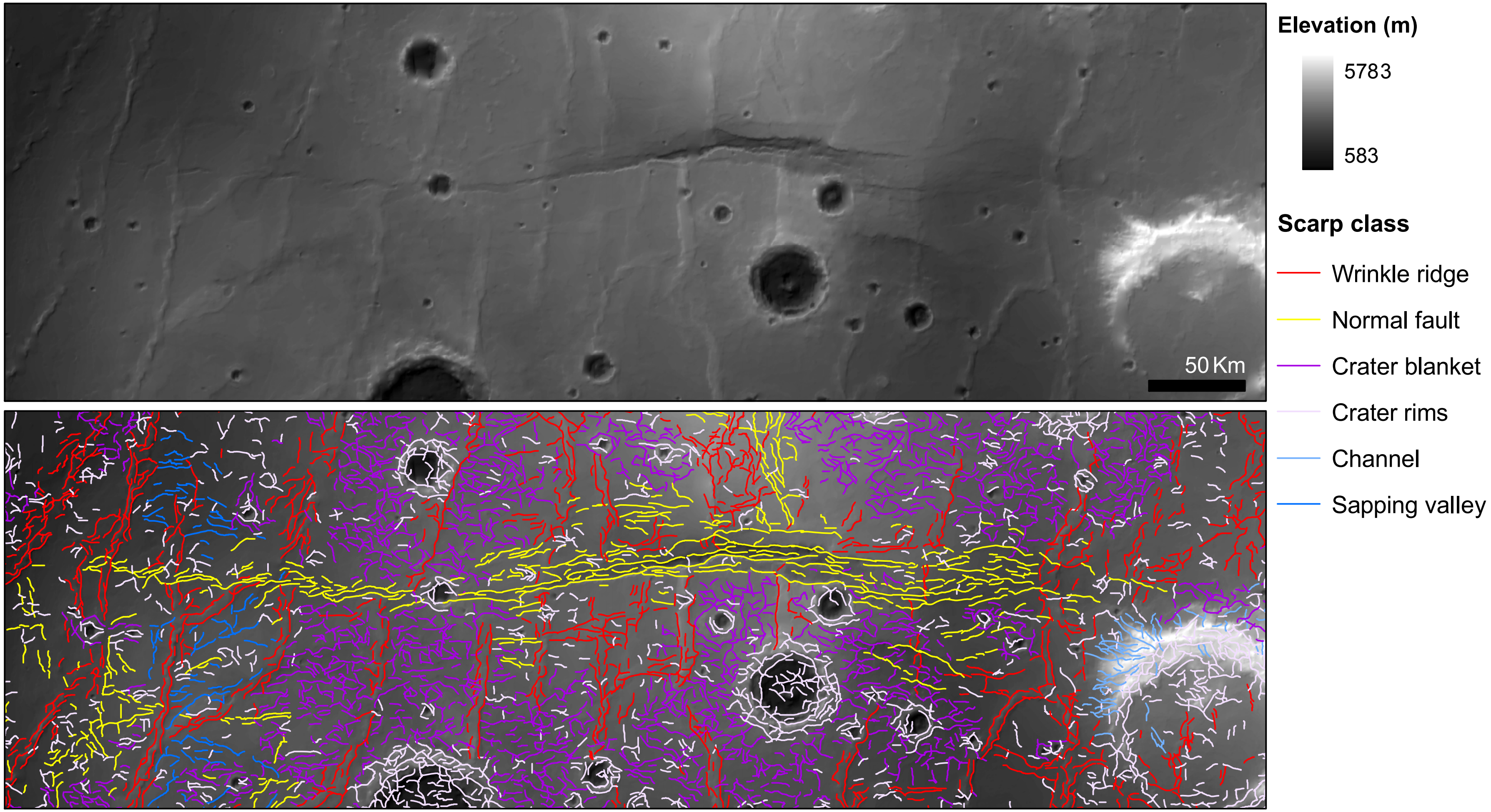

Figure 2.2 - MOLA shaded relief and classified lineaments representing topographic discontinuities on Mars surface. Each scarp was automatically extracted from MOLA data and manually classified according to their geomorphologic meaning using THEMIS infrared, HRSC and CTX imagery. See annex 1 for the complete mapping of the East Thaumasia region.

2.3.1 MOLA data

The size of MOLA shots footprint is approximately 150m and distance between shots is 300m (Smith et al., 2001). MOLA precision experiment data records were used to interpolate a DTM with ~231 m/pixel resolution, following the procedure described by Okubo et al. (2004) and applying the natural neighbor interpolation method (Abramov and McEwen, 2004). Pixels in the obtained DTM have a mean distance to a MOLA shot of 652±639m. The MOLA tracks are oriented approximately N-S which creates systematic linear interpolation artifacts that are more relevant when the distance between tracks increases. These artifacts are one of the challenges when using MOLA data, but if an algorithm is capable of handling this problem it will certainly be more robust when applied to higher quality DTMs.

2.3.2 Synthetic data

The topography of a set of synthetic grabens with different dimensions and strikes was constructed (Figure 2.3a). Displacement values were measured from a 60.3 km fault scarp centered at 15.95ºS latitude and 61.86ºW longitude using MOLA profiles. A superellipse function defined as:

$$|x/a|^n+|y/b|^n=1 \qquad \text{(Eq. 2.1)}$$

with $n=1.4$ was fitted to the data. Maximum throw (D_{max}) is obtained using the linear relation measured from the analyzed fault scarp ($D_{max}=L/600$ where L is the fault length). Circular or elliptical functions are often used to model displacement-length functions (Peacock and Sanderson, 1997; Polit et al., 2009) but those correspond to the particular case of a superellipse with $n=2$. The generated synthetic fault scarps are all scaled versions of the real tectonic feature and the spatial resolution of the synthetic model is the same of the MOLA DTM.

To understand the impact of MOLA data gaps in the algorithm output, the synthetic dataset was sampled along a pattern of MOLA tracks and a DTM was interpolated using the same procedure used to derive the MOLA DTM (Figure 2.3a').

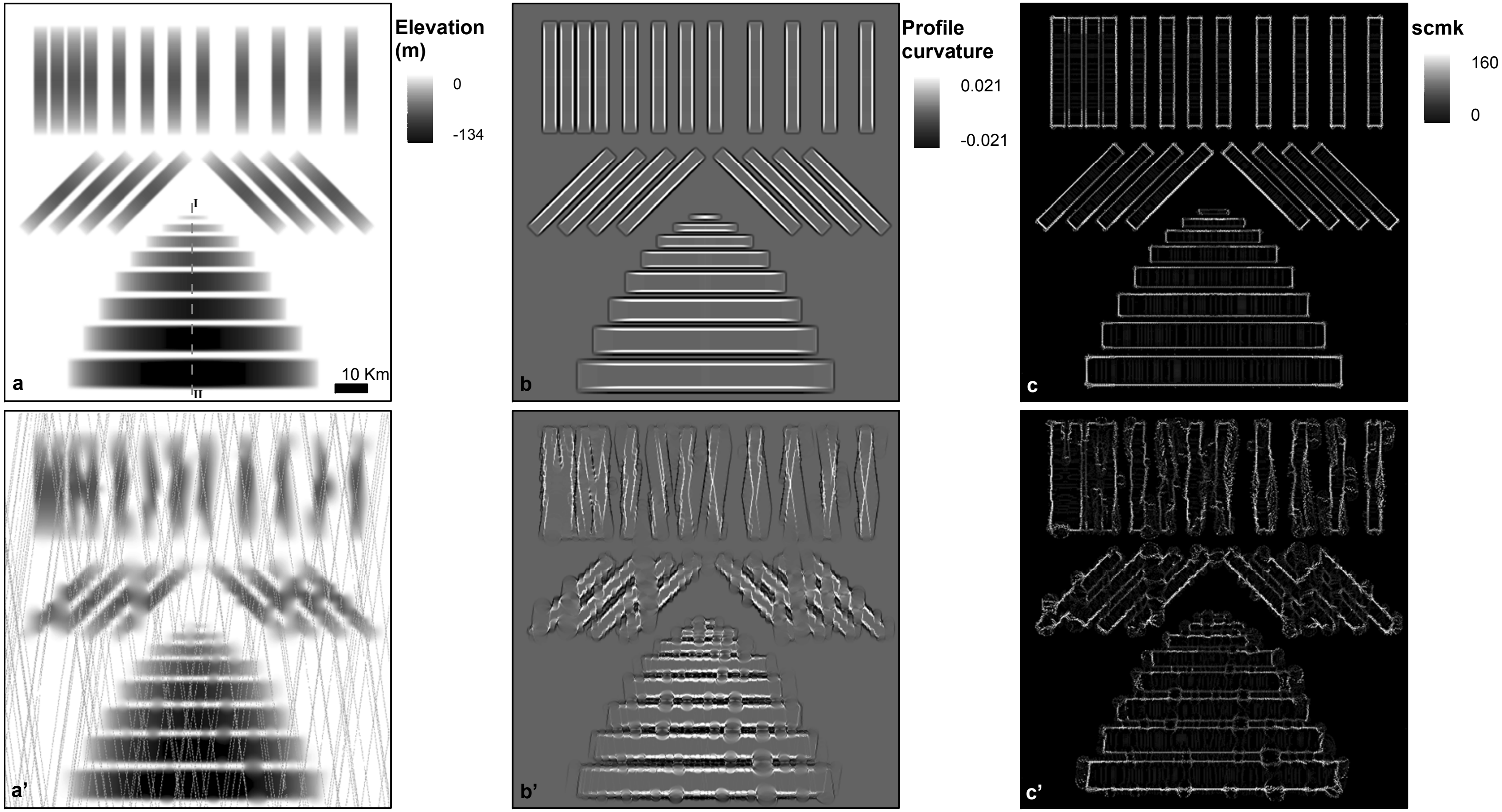

Figure 2.3 – Synthetic graben topography scarp markers; (a) synthetic graben topography (see section 2.3.2 for explanation); (a’) synthetic graben topography sampled and interpolated using MOLA data tracks mask; (b and b’) profile curvature for (a) and (a’) datasets; (c and c’) main scarp marker *scmk* (see section 2.4.1 for explanation). Note the effect of MOLA data gaps on the elevation profile curvature values (b and b’). The *scmk* is more noise tolerant and represent better the scarps (data gaps are less evident in plate c’ when comparing with b’). Note that the location of the North-South striking scarps are best constrained in (c’) than in (b’).

2.4 Methodology

The scheme in Figure 2.4 summarizes the main steps followed to achieve automatic scarp extraction from altimetry data.

Scarps are segmented using two multiscale approaches: wavelet transform edge analysis and the morphological multiscale gradient. Segmented scarps are classified according to their dip direction and vectorization is achieved after the application of several morphological transforms that reduce scarp markers to one pixel width lines.

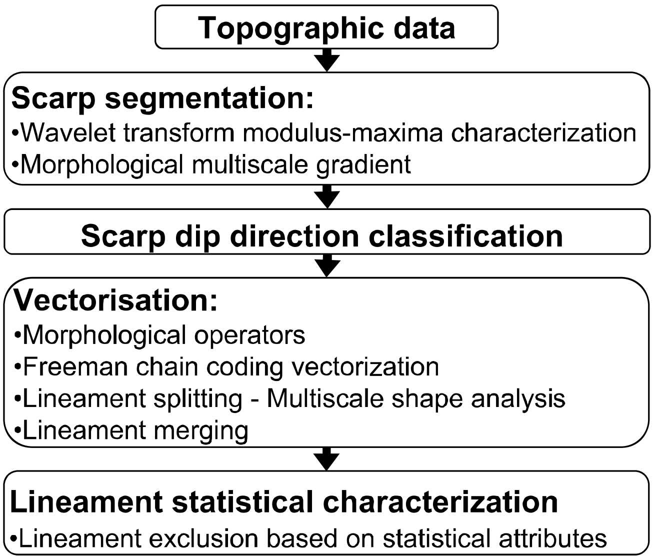

Figure 2.4 - Main steps of the methodology used to scarp extraction from MOLA data.

2.4.1 Scarp markers

2.4.1.1 Non-parametric multiscale morphological gradient

Morphological operators are extensively used in this work and commonly used operators are not formally defined. Mathematical morphology nomenclature used in this work is the same adopted by Soille (2002).

One of the morphometric parameters that can be extracted from a DTM and that is used as a scarp marker, is the height of the scarps. The height of a scarp can be computed using mathematical morphology operators such as the morphological gradient that returns the maximum height variation inside a neighborhood defined by a structuring element (SE). A problem arises when defining the size of the SE since scarps can have different horizontal extents: if the SE is smaller than the scarp horizontal extent, heights will be underestimated; if the SE is too large there is the risk of merging small scarps.

To handle this problem the parameterized morphological multiscale gradient (PMMG) defined at scale *n* as:

$$\rho^{*}_{nB} = \rho_{nB} . T_{[1,t_{ma}]} \varepsilon_{(n-1)B} WTH_{nB\rho B\rho} \qquad \text{(Eq. 2.2)}$$

is applied to the DTM. This operator ensures that the gradient values will have a minimum thickness. Since real scarps have different widths, it is necessary to compute the point-wise maximum of a set of PMMGs at scales *n* minor than the maximum scarp horizontal extent defined by the user. This operation corresponds to the non-parametric multiscale morphological gradient defined as:

$$\rho^{*} = \bigvee_{nB} \rho^{*}_{nB} \qquad \text{(Eq. 2.3)}$$

and will give scarp heights independently of their horizontal extent (Soille, 2002). At this point, since we are only interested in producing a scarp marker, the structuring element *B* is a disk. Linear SEs allow the directional measurement of the height of the scarps and will be used for measuring accurately the height of normal fault scarps so that extension could be estimated.

2.4.1.2 Wavelet edge analysis

Little (1994) used wavelet analysis to enhance and extract fault scarps from bathymetric data. The first derivative of the cubic B-spline function has been used as mother wavelet and allowed scarp identification also on Mars (Vaz et al., 2006; Alves et al., 2008). This technique provides good results but since the analysis is done only at one selected scale the results are highly dependent on the scale of analysis and more subject to the influence of noise (namely to the data gaps existent between MOLA tracks).

It has been shown that Earth topography fits a model constituted by the convolution of singularities with a multifractal noise (Gagnon et al., 2006). The characteristics of this noise are the same for continental margins, oceanic and continental crust; only the degree of smoothing of the singularities varies, this variation being responsible for the different topographic patterns on our planet. Having this model in mind a wavelet multiscale edge characterization has been implemented since this methodology is capable of singularity detection and characterization (Mallat and Hwang, 1992; Evertsz et al., 1995; Venugopal et al., 2006).

The continuous wavelet transform (CWT) is defined as:

$$T_{\psi}[f](b,a) = \frac{1}{|a|}\int f(x)\psi\left(\frac{x-b}{a}\right)dx, \quad a > 0, b \in R \qquad \text{(Eq. 2.4)}$$

where ψ represents the function used as mother wavelet. Scale and location are represented by parameters a and b (Mallat, 1989; Venugopal et al., 2006). The first derivative of the Gauss function is used as mother wavelet since it is a function that permits the computation of the continuous CWT and is anti-symmetric which produce higher magnitudes of the CWT coefficients associated with signal discontinuities (Kumar and Foufoula-Georgiou, 1997).

The 1D scale-space filtering procedure described by Evertsz et al. (1995) is adopted here. It consists of scanning the gridded MOLA DTM in four directions (E-W, N-S, NE-SW and NW-SE) in order to obtain 1D profiles (Figure 2.5a). The wavelet transform modulus maxima (WTMM) lines are extracted from the profile CWT using the zero-crossings of the transform second derivative (Mallat and Hwang, 1992) (Figure 2.5b). A 2D analysis is also possible (Mallat and Zhong, 1992; Mallat and Hwang, 1992) but the 1D approach is simpler and computationally less demanding than the 2D case where the WTMM form surfaces in the scale-space (Evertsz et al., 1995).

Three parameters are measured from the identified maxima lines in the scale-space plane: the general maxima scale, the Hölder exponent and the maximum scale at which a maximum line exists (Evertsz et al., 1995). The parameters are subsequently gridded using the location of the maxima lines at the lowest scale under analysis (Evertsz et al., 1995). The fact that the measured multiscale parameters are gridded using the location of the maxima lines lower scale ensures a better spatial location of the topographic discontinuities.

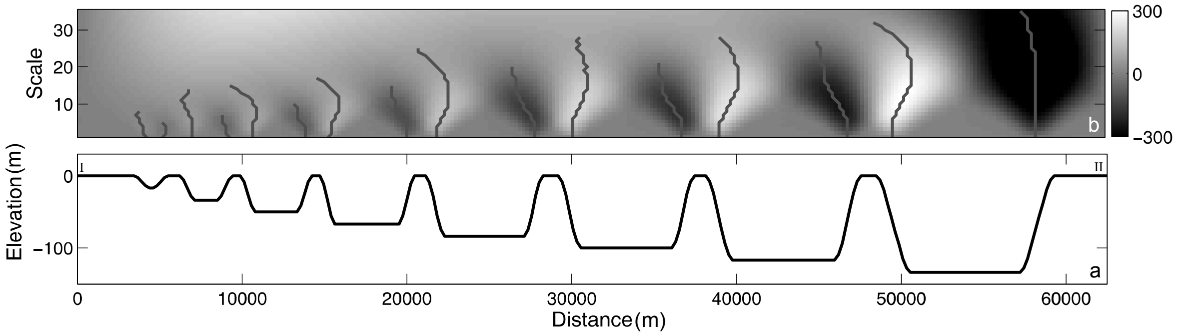

Figure 2.5 - Continuous wavelet transform and wavelet transform modulus maxima (WTMM) lines of a topographic profile; (a) synthetic fault scarp altimetry (see Figure 2.3a for profile I-II location); (b) wavelet transform coefficients and extracted WTMM lines (gray lines). Several characteristics of the WTMM such as the general maxima scale, the Hölder exponent and the maximum scale at which a maximum line exists (Evertsz et al., 1995) are used to identify and characterize the topographic discontinuities. Note the changing characteristics of WTMM lines with scarp magnitude/spacing variation.

The Hölder exponent $h(x_0)$ is related with the regularity of the discontinuities and characterizes the local roughness of the topography. In the present case since the used wavelet has only one vanishing moment $0 < h(x_0) < 1$. Lower values of the Hölder exponent correspond to sharper discontinuities and higher values to smoother ones (Evertsz et al., 1995; Venugopal et al., 2006). The Hölder exponent is especially important because it allows the segmentation of areas where the MOLA data are interpolated and that correspond to smoother areas. The spatial variation of this parameter can also be useful for defining different roughness units which seem to correlate well with geological units (Orosei et al., 2003).

The general maxima scale can be used to compute the local "frequency" of the signal (Mallat and Hwang, 1992) and the maximum scale that a WTMM line achieves allows the segmentation of the more important discontinuities and reduces the impact of noise.

The discontinuity strength is the CWT coefficient at $a=1$ and corresponds to the local first derivative (Evertsz et al., 1995). This parameter is replaced by the gradients obtained using two orthogonal wavelet based filters, which permit the identification of the dipping direction of the topographic discontinuities (Little, 1994).

2.4.2 Treshold and vectorization

The scale-space threshold introduced by Evertsz et al. (1995) was modified so that outputs are directional and the height of the scarps is also included in the threshold scheme. The threshold parameters are defined interactively for a small area using a graphical user interface and are then applied to the entire area.

Let *wscl* be the sum of the wavelet regional maxima and the wavelet edge maximum scale, *scmk* is the main scarp marker created according to:

$$scmk = \rho^{*} \vee \left(wscl.t/wscl_{max} \right) \qquad \text{(Eq. 2.5)}$$

(Figure 2.3c and Figure 2.3c'). In other words, *wscl* is linearly stretched until a maximum value *t* and a point-wise maximum ensure the replacement of lower values of ρ^{*} by the stretched values of *wscl*. The purpose of this operation is to enhance the extremities of the scarps where $\rho^{*} \to 0$.

Let $wstrg_{\alpha}$ be the wavelet strength along the direction α. The sign of the horizontal and vertical components gives the dip direction of the scarps (Little, 1994). This attribute is used to segment the scarps in four dipping directions, North, South, East and West by applying a hysteresis threshold (*DBLT*) after a white top-hat transform (*WTH*) that restrains the extent of the gradients (Soille, 2002).

The Hölder exponents (*h*) are also segmented so that smoother discontinuities are eliminated.

The final scarp marker f_{α} with the scarps that dip to α is given by

$$f_{\alpha} = DBLT_{[t_1 \le t_2 \le t_{max}]}\left[WTH\left(wstrg_{\alpha} \right) \right] \cap DBLT_{[t_1 \le t_2 \le t_{max}]}\left(scmk \right) \cap T_{[0,\, t]}\left(h \right) \qquad \text{(Eq. 2.6).}$$

Four binary matrices are obtained with the scarps that dip to one of the geographic quadrants. A second directional segmentation is performed by computing the mean vector magnitude and direction for each binary object. The final dip direction attributed to each pixel corresponds to the direction of the maximum mean magnitude (for a different approach based only in the area of the binary objects see Alves et al., 2008). The fact that this direction segmentation is performed for an area instead of an isolated pixel makes the process more robust to noise.

At the end of this step eight binary images are created from the directional segmented matrix using a 45º angular bin. The following sequence of morphological operators is independently applied to those directional binary matrices so that objects are reduced to lines with one pixel width.

Small objects are eliminated and objects that are close to each other are merged by applying a closing transform with a line SE with 3 pixels length. This operation is followed by the removal of small and non-linear holes (an opening by reconstruction is applied to the identified holes using a line SE with 10 pixels length). A skeleton operation by the letter *L* of Golay's alphabet is performed and the objects are reduced to one pixel width lines (Soille, 2002). The morphological operators used until this point can be written as:

$$g = SK_L\{f \cup \gamma_R[FILL(f) - f]\} \qquad \text{(Eq. 2.7)},$$

where

$$f = \phi_B(f_\alpha) \qquad \text{(Eq. 2.8)}$$

and f_α is the starting binary image with the scarps that dip to α. The azimuth of the line SEs used is perpendicular to each α.

The skeletonization produces many small branches that are eliminated by the application of a pruning. This operation will remove *n* points from the extremities of the skeletons and simultaneously reduces the initial length of the lines. This problem can be handled by adding back some of the removed branches using the endpoints of the pruned skeleton as markers according to

$$k = PRUNE^{(n)}(g) \cup R^{\delta}_{[g \backslash PRUNE^{(n)}(g)] \cup Y}(Y) \qquad \text{(Eq. 2.9)}$$

where

$$Y = ENDPOINT\lfloor PRUNE^{(n)}(g) \rfloor \qquad \text{(Eq. 2.10)}$$

and *n* denotes the size of pruning (Soille, 2002).

The resultant skeletons are vectorized throughout the application of the Freeman chain coding technique (Freeman, 1961). Note however, that in the case of complex objects (with more than two endpoints) the longest segment is first extracted and vectorized using the identification of the longest geodesic path (Soille, 2002). This step is important because, after the vectorization, the extracted lineaments are submitted to a multiscale shape analysis where line segments are split using the identified high curvature points (Antoine et al., 1996). The uniformly striking segments are finally merged using a directional and distance tolerance. Better results are obtained when several (four are used in the present work) merging operations are sequentially performed with decreasing directional (45º, 25º, 10º and 5º) and increasing distance tolerances (2, 4, 6 and 8 pixels). The extracted lineaments, that correspond to the normal faults scarps, are presented in Figure 2.6a and Figure 2.6a'.

2.4.3 Morphometric characterization

Several morphometric attributes are then computed for each identified scarp creating a scarp database. Length and azimuth are statistical parameters usually obtained from digitized lineaments (Schultz, 2000; Borraccini et al., 2007). The proposed automatic mapping approach guarantees a pixel-based georeferentiation. It ensures that the profile curvature value along the lineament trace tends to zero; in other words, the extracted lineaments are accurately located in the middle of the scarps, in the points where the profile curvature approximates zero. This fact ensures that it is possible and meaningful to extract other morphometric parameters from the DTMs, relating them with each individual scarp. Parameters such as the mean slope, mean aspect or mean height (Figure 2.6a and Figure 2.6a') measured across each scarp can be easily extracted from the DTM and stored on a database.

When extracting any morphometric parameter derived from MOLA data some problems are present due to the preferential orientation of the data profiles and to the effects of interpolation in the gaps between data tracks. A buffer of 700 m is used so that measurements are only taken on pixels located closer to the MOLA tracks.

This spatial restriction aims to diminish the effect of interpolation artifacts, but the main problem remains. MOLA data gaps could break lineament continuity leading to an over-segmentation of the lineaments (compare extracted lineaments on Figure 2.6a and Figure 2.6a'). This over segmentation is less evident for EW scarps due to the NS preferential orientation of the MOLA tracks. Those problems are specific of MOLA data and better quality DTMs should not present this kind of problems.

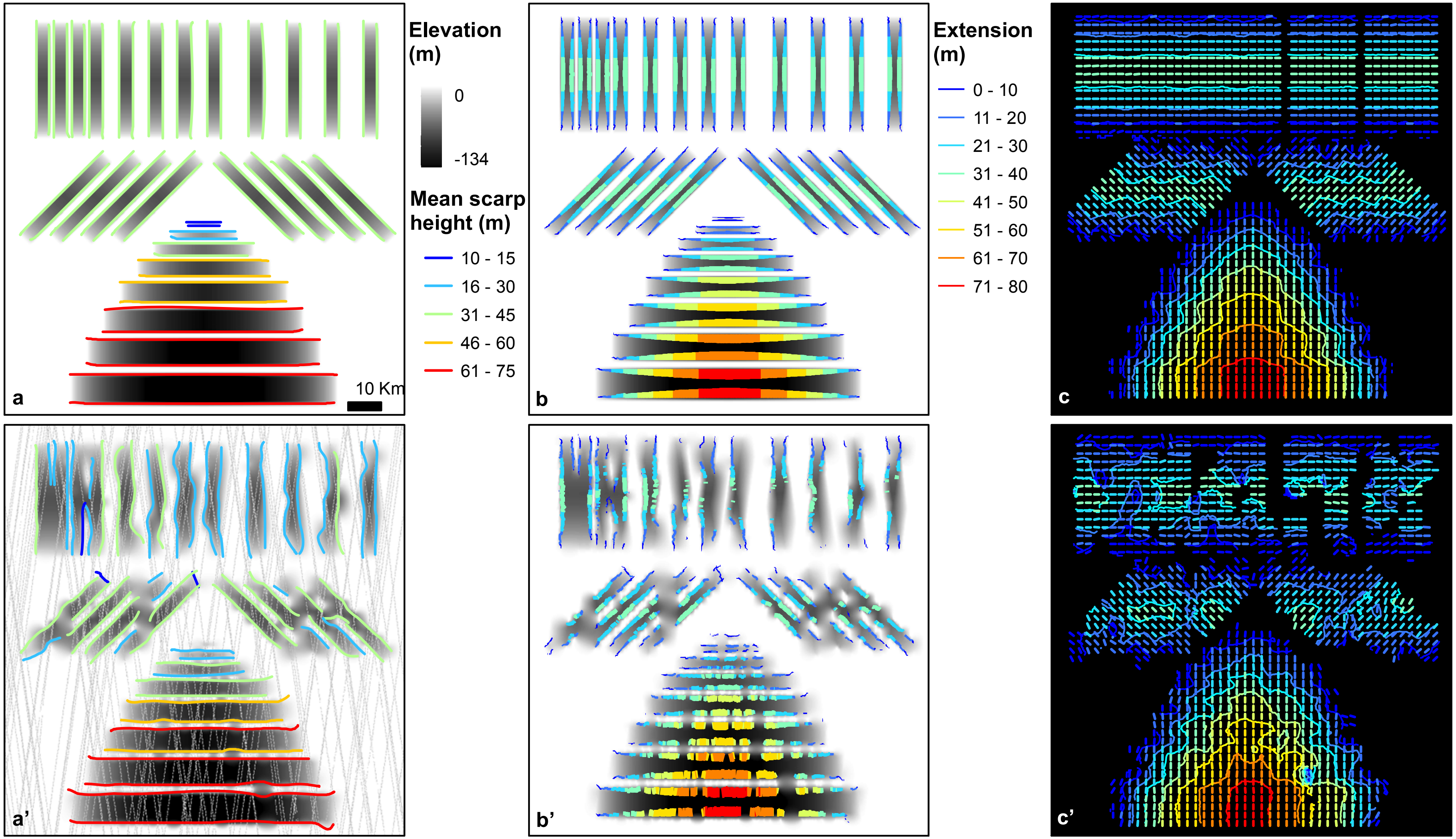

Figure 2.6 – See next page for full legend.

Figure 2.6 – Identified fault scarps and estimated extension vectors; (a) extracted lineaments from synthetic graben topography (color scale represent the mean scarp height); (a') lineaments extracted from degraded DTM (data tracks used on DTM interpolation arerepresented in light gray); (b) extension vectors estimated for the normal faults (see text for explanation); (b') extension vectors computed from the degraded DTM, note that a spatial buffer was used to exclude those vectors associated with larger interpolated areas; (c and c') extension vector fields associated with the modeled normal faults. Note that despite the limitations imposed by the data gaps, estimated magnitude and azimuth of the strain vectors in chart (c') agree with those computed in plate (c). The preferential ~North-South alignment of the data tracks makes that the proposed methodology is more effective in characterizing East-West striking features.

A morphometric parameter of particular interest for tectonic purposes is the angle of dip and the dip direction of the scarps measured from tip to tip. Those parameters are obtained by dividing each lineament in two equal segments and by computing the 3D centroid for each segment. The dip direction and dip angle are computed between those centroid points using geodetic measurements, avoiding all the issues related with the type of map projection used. Those two parameters can be useful for identifying regional high amplitude topographic trends that could occur superimposed on the high frequency tectonic patterns.

Other datasets such as magnetic or gravimetric anomalies are also important for tectonic analysis (Spagnuolo et al., 2008) and could be integrated in the database attaching the values of the anomalies for each scarp using the available gravimetric and magnetic models of Mars (Lemoine et al., 2001; Connerney et al., 2005).

2.4.4 Scarp classification

Despite the initial interest in mapping only tectonic features, the algorithm extracts all the topographic discontinuities present in the DTMs, which permits a thematic morphometric analysis once the lineaments are classified according to their genetic and geomorphologic nature.

On a GIS environment the automatically recognized scarps were overlaid on the available imagery datasets and a user has classified each scarp according to their geomorphologic meaning and characteristics (a scarp could be classified for example as a normal fault, and the sense of shear or the degree of degradation of the scarp could also be recorded). This phase of classification still relies on the human judgment and interpretation, but in this case the user is just prompted to classify the recognized structures since the effort of digitizing the features is completely eliminated.

The proposed algorithm does not discriminate a priori any kind of geomorphologic feature, which forces the user to classify and integrate the totality of features on the area. This may be seen as an advantage as it constrains the user not to focus only in one kind of geomorphologic feature but to take into account the relations between several aspects of the topographic signal. For instance, a user who is only interested in the tectonic characterization of a specific area will be forced to integrate in the analysis other factors responsible for the creation of topographic discontinuities such as erosion, fluvial/glacial activity, cratering or volcanism for example.

Figure 2.2 shows the resulting thematic classification of the mapped lineaments. Several classes were defined by a user using the context information offered by imagery. The obtained lineament database constitutes the basis for the following strain analysis. Only the analysis of normal faults is presented but this database can by itself constitute the starting point for other methodologies focused on other geomorphologic features using the obtained morphometric parameters. See annex 1 for the complete lineament map of the East Thaumasia region.

2.4.5 Extension estimation

A simple model that assumes non-rotational fault planes with a constant dip along the faults has been commonly applied on Mars (Hauber and Kronberg, 2001; Borraccini et al., 2005; Spagnuolo et al., 2008). The vertical throw d associated with each fault scarp is usually measured on topographic profiles normal to the strike of the faults. The extension D is computed according with

$$D = d/tan_{\alpha} \qquad \text{(Eq. 2.11)}$$

where α represents the dip angle. Note that the obtained values are always minimum values since deposition in the base of the scarps is always neglected.

It has been shown above that the automatic mapping and morphometric characterization of any scarp is possible. For the purpose of normal faults' extension estimation the parameter of interest is the elevation difference between the base and the top of the fault scarps (the altitude difference between the hanging-wall and the footwall). In section 2.4.1.1 the use of the non-parametric multiscale morphological gradient (NPMMG) for measuring scarps height has been introduced.

For the scarp recognition algorithm an isotropic SE yields better results but for morphometric analysis a linear SE ensures a more precise estimation (the use of a circular SE would increase the measured values). The database is queried so that only lineaments, whose strike is comprised within an angular interval are selected at each iteration (in the given examples an interval of 20º is employed for a total of nine iterations).

The NPMMG is computed using a line SE perpendicular to the strike of the selected lineaments. It is the same principle behind the manual interpretation of the topographic profiles but in this case the process is completely automatic and the topographic profiles are replaced by the linear SE. The maximum size of the line used as SE is the only necessary input. This size must surpass the maximum horizontal extent of the scarps under analysis, otherwise there is the risk of underestimating the height of the scarps. In the given examples a maximum size of 3km was used.

The identified lineaments that were classified as normal fault scarps are used to extract the values of the NPMMG used to compute the regional extension associated with a particular normal fault. The extension vector azimuth is computed by averaging the DTM aspect angle in the vicinity of scarp segment (in all the presented examples four neighbor pixels are used).

The second parameter necessary to compute extension is the fault plane dip angle (α). Fault scarp slope is one of the morphometric parameters obtained from the DTM and can be used in cases where scarp degradation is not evident. An important factor that can influence the measured slopes is the smoothing of highly sloped areas due to the coarse resolution and to footprint size of MOLA data (Kim and Muller, 2009).

In the analyzed rift a mean slope of 2.9±1.9º was computed, which indicates fault scarp degradation and/or slope smoothing. For this reason, a constant dip of 60º was assumed for the synthetic and real examples. This is a value frequently used to compute extension on Mars (Hauber and Kronberg, 2001; Borraccini et al., 2005; Spagnuolo et al., 2008). Note however that this angle corresponds to a theoretical value; since low-angle normal faults are common on Earth (Wernicke, 1995) extension values can be underestimated.

At this point, it is possible to estimate the extension as well as appreciate the spatial variation of the extension for each fault scarp since the extension is computed for the entire scarp extent. This spatial variability of extension is well illustrated by the extension vectors shown in Figure 2.6b.

2.5 Discussion

2.5.1 Synthetic datasets

In Figure 2.7a the measured normalized displacement-length (D-L) scaling function, of all the scarps present in Figure 2.6a, is compared with the D-L scaling function used to model the scarps (see section 2.3.2). In this ideal case the D-L scaling function was accurately estimated. For the case of Figure 2.6a' DTM, the over segmentation of the lineaments due to the MOLA data gaps causes that the D-L relation could only be estimated on some selected scarps whose continuity was not affected (the six bottom EW scarps where selected to produce Figure 2.7b chart and a 900 meters buffer was used to avoid larger data gaps bias). Note however the larger dispersion and the slight shift to the left of the measures caused by the underestimation of the lineaments length (scarp extremities are especially sensible to MOLA data gaps affecting the measured length). This problem can be avoided by centering the D-L curve of each fault, using the measured maximum displacement and assuming a symmetric D-L curve.

Figure 2.6b and Figure 2.6b' shows the displacement vectors computed along the fault scarps. Note the effect of the 900 m buffer on selecting only the vectors located on areas with good data coverage (smooth areas corresponding to DTM interpolation artifacts are excluded from the analysis).

Strain vectorial fields are computed by averaging the obtained extension vectors on a circle of 2.5 km radius for a 1.5 km cell grid (Figure 2.6c and Figure 2.6c'). From the analysis of both vectorial fields is possible to conclude that, despite the limitations imposed by the MOLA track gaps, the described methodology is able to estimate the magnitude and azimuth of the strain vectors. Those results are conditioned by the orientation of the tectonic features under analysis since strains related with ~NS striking faults could be underestimated or even ignored when using MOLA data (in future work, a quantitative analysis of this directional bias will be presented). In both cases it is possible to identify the main areas affected by a larger extension as well as to characterize the direction of that extension.

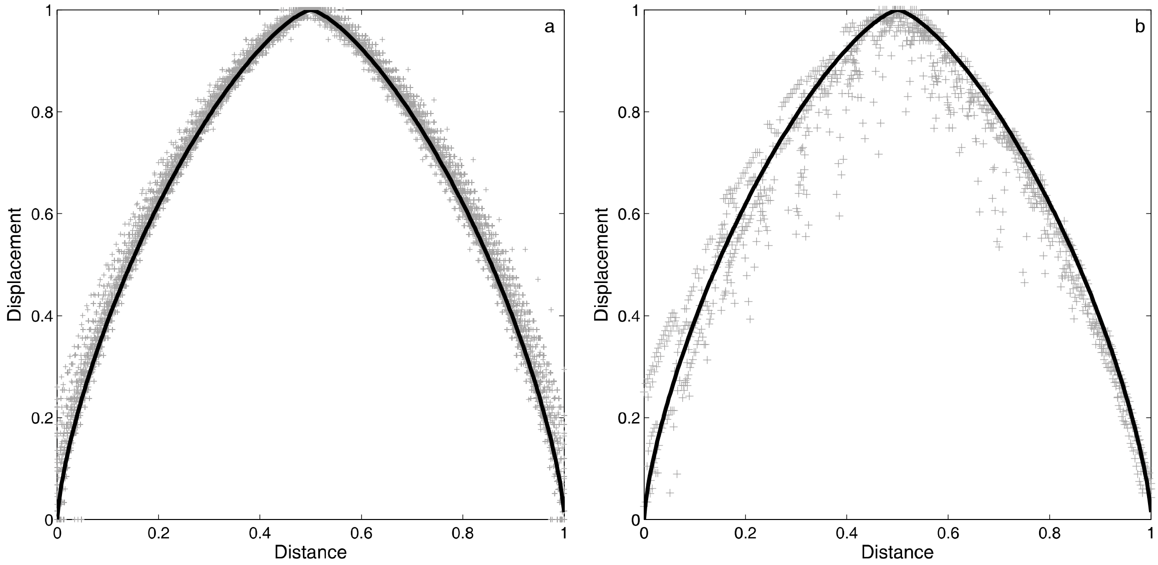

Figure 2.7 – The black lines represent the original normalized displacement-length (D-L) scaling function used to produce the fault scarps topography. Chart (a) gray symbols represent the measured D-L scaling functions for all the identified scarps present in Figure 2.6a. The six bottom EW scarps of Figure 2.6a' were selected to produce chart (b) (data gaps make this selection necessary due to the over-segmentation of the extracted lineaments). In both cases the measurements approximate the D-L original curve. This fact proves the efficiency of the proposed method for estimating the extension from the measurement of the vertical throw along the fault scarps.

In the analysis of the synthetic dataset only a pure shear scenario was considered (where σ_1 is aligned with the fault traces) despite normal faults presenting en-echelon geometries being relatively common on Mars (Bistacchia et al., 2004; Borraccini et al., 2007; Fernández and Anguita, 2007) denoting the important role of transtensional regimes on Mars. If a complete characterization of the displacement associated with a normal fault on a simple shear scenario could be difficult, the rotation of the displacement vectors, in cases where transtension is evident, could be used to approximate the oblique extension directions.

2.5.2 North Thaumasia Planum rift

From the analysis of Figure 2.2 and Figure 2.8a maps, it stands out that a younger ~EW set of normal faults intersect all the pre-existing structures, namely the set of NS-NNE wrinkle ridges that are locally affected by a right-lateral strike-slip movement responsible for the offset of some wrinkle ridges. A maximum dextral offset of 14km is observable in Figure 2.9a, between wrinkle ridge segments II and II', but displacement is not constant for all wrinkle ridges (compare I-I' with II-II' displacements). This suggests that this shear zone is related with a lateral accommodation structure that acted unevenly during the formation of the wrinkle ridges. An older structure that affects the basement may be involved, and may be responsible for this dextral accommodation zone. The location of this shear zone coincides with the location of the rift, which indicates that the rift development was conditioned by the presence of those pre-existent fractures.

Grabens striking N-NW are likely posterior to the wrinkle ridge formation, but their geometry is still consistent with a dextral shear related with a σ_1 striking ~NW-SE. The stress field responsible for those features is compatible with the possible south-eastward movement of the Thaumasia Plateau during Noachian to Early Hesperian times (Webb and Head, 2002; Anguita et al., 2006).

The following analysis will be centered only on the strains related with the last distensive episode, responsible for the formation of the rift. A left-lateral component is more evident in the western part of the rift where sigmoidal en-echelon grabens occur (Borraccini et al., 2007; Montgomery et al., 2009).

A detailed strain analysis is presented in Figure 2.8c and Figure 2.8d. The mean scarp azimuth along the rift is shown in Figure 2.8b (a 0.1º longitude moving average was used) and the rift axis mean azimuth (89.8 ±0.3º) was defined as the scarps mean azimuth weighted by the mean vertical throw for each scarp.

Eight rift domains were identified from the analysis of the faults azimuth curve, defining a sequence of zones with alternating fault trends. A first-order segmentation corresponds to the alternating areas with ~75-80º and ~110º striking faults (Figure 2.8a). A second-order segmentation is obtained from some of the inflection points of the azimuth curve in Figure 2.8b (boundaries between sectors I, II and III – dashed boundary lines).

Sectors I, II and III display a maximum obliquity between the fault trend and the rift axis of -15º (obliquity angles are positive clockwise from the rift axis). Local obliquity variations, in those regions, appear to be spatially correlated with the wrinkle ridge location (note that azimuth oscillations are located nearby wrinkle ridges). This suggests that pre-existent wrinkle ridges could be responsible, at some degree, for obliquity variations along the rift since their presence may have influenced the stress field trajectories.

In zones IV and V ~75-80º and ~110º fault sets are superimposed, which lead to the reduction of the absolute obliquity values (notice the color code on Figure 2.8a).

Figure 2.8c and Figure 2.8d shows the extension vectors for the North and South dipping normal faults. Strain is more intense in sectors IV, V and VI but strain partition is not symmetric particularly along the central part of the rift. Strain of South dipping faults is higher between zones V and VI. North dipping faults accommodate higher extension values on rift zones IV and V. This same asymmetric strain signature has been recognized in transtensional pull-apart basins, where graben polarity change along strike forming negative flower structures (McClay and Dooley, 1995; Wu et al., 2009).

Profiles P1 and P2 (Figure 2.9) show the shifting rift geometry in zone V. In P1 and P2, the main faults dip toward North and South, respectively. In both cases the rift blocks are tilted toward the main normal fault possibly forming sinistral negative flower structures with opposite polarity.

Faults in zone VI are characterized by a maximum obliquity angle of 18° and strain for North and South dipping faults decrease eastward.

Rift zone VII has an obliquity angle of -8º and the extension is splayed on a wider area forming a sigmoid structure that connects with neighboring rift segments through soft-linked accommodation zones (McClay and White, 1991). The strain partition is also asymmetric in this rift segment. Strain seems to be mainly accommodated by South dipping faults.

Obliquity angles in the easternmost rift segment increase eastward reaching 22° near Lassell crater. Strain also decreases when the rift reaches the rim of Lassell crater. This apparent decrease in strain could be due to the deposition of volcano-sedimentary materials on the rift floor. Faults seem to cross the highly dissected Lassell crater North rim. East of Lassell a volcano presenting eroded flanks probably covers the faults, which are again visible more to the East with a ~125° azimuth (Figure 2.10). The location of this volcano, aligned with the rift, suggests that its formation could be linked with the ascension of magma along the described fault system.

Another bend seems to occur as faults cut Coprates rise eastern border with an azimuth of ~90° (see Figure 2.1 for context). Despite presenting the same pattern of alternating striking segments, fault scarps are increasingly degraded when approaching Coprates rise eastern edge.

The strain decreases eastward from sectors III to I. The en-echelon left-stepping faults in these zones may correspond to an early stage of the rift formation (Wu et al., 2009) which implies a possible East-West migration of the tectonic activity.

Despite the strong evidences for a transtensive regime, extension vectors presented in Figure 2.8c and Figure 2.8d only represent the normal component of the real displacement vectors. This perfectly represents the case of a soft linkage scenario, where strike-slip and oblique faults are not present and accommodation zones are responsible for rift polarity changes. McClay and White (1991) analogue modeling of oblique rifting produced this kind of patterns with a total absence of oblique and strike-slip faults. Note however that their analogue experiments generate rifts with a uniform width reflecting the simple geometry of the underlying base detachment in the experimental apparatus.

A constant rift width is clearly not the case of the rift depicted in Figure 2.8a. Rift width, fault arrangement and strain distribution present important along-strike variations, making the fault pattern more similar to the normal fault arrays responsible for the formation of more complex pull-apart basins as those modeled by Wu *et al.* (2009) and McClay and Dooley (1995). This indicates that a strike-slip component, although not estimated, can be present as described in analogue experiments (Tron and Brun, 1991; Schlische et al., 2002; Wu et al., 2009), as well as in the analysis of oblique extensional provinces such as the Dead Sea fault system (Brew et al., 2001; Wu et al., 2009) or the East Anatolian fault system (Aksoy et al., 2007). This suggests that at least some of the normal faults may have an oblique displacement component.

All the observations described so far agree with a complex left-lateral transtensive regime for the entire rift. The ~75-80º faults acted first as dextral strike-slip faults during the wrinkle-ridge formation phase. A subsequent tectonic inversion was responsible for transforming these pure dextral strike-slip faults in extensional structures that possibly accommodate some left-lateral motion. Pull-apart basins probably display characteristic negative flower structures as predicted by Webb and Head (2002) (Figure 2.9). Clear evidences for any transpressive regime in the eastern part of the rift, as hypothesized by Montgomery et al. (2009), were not found.

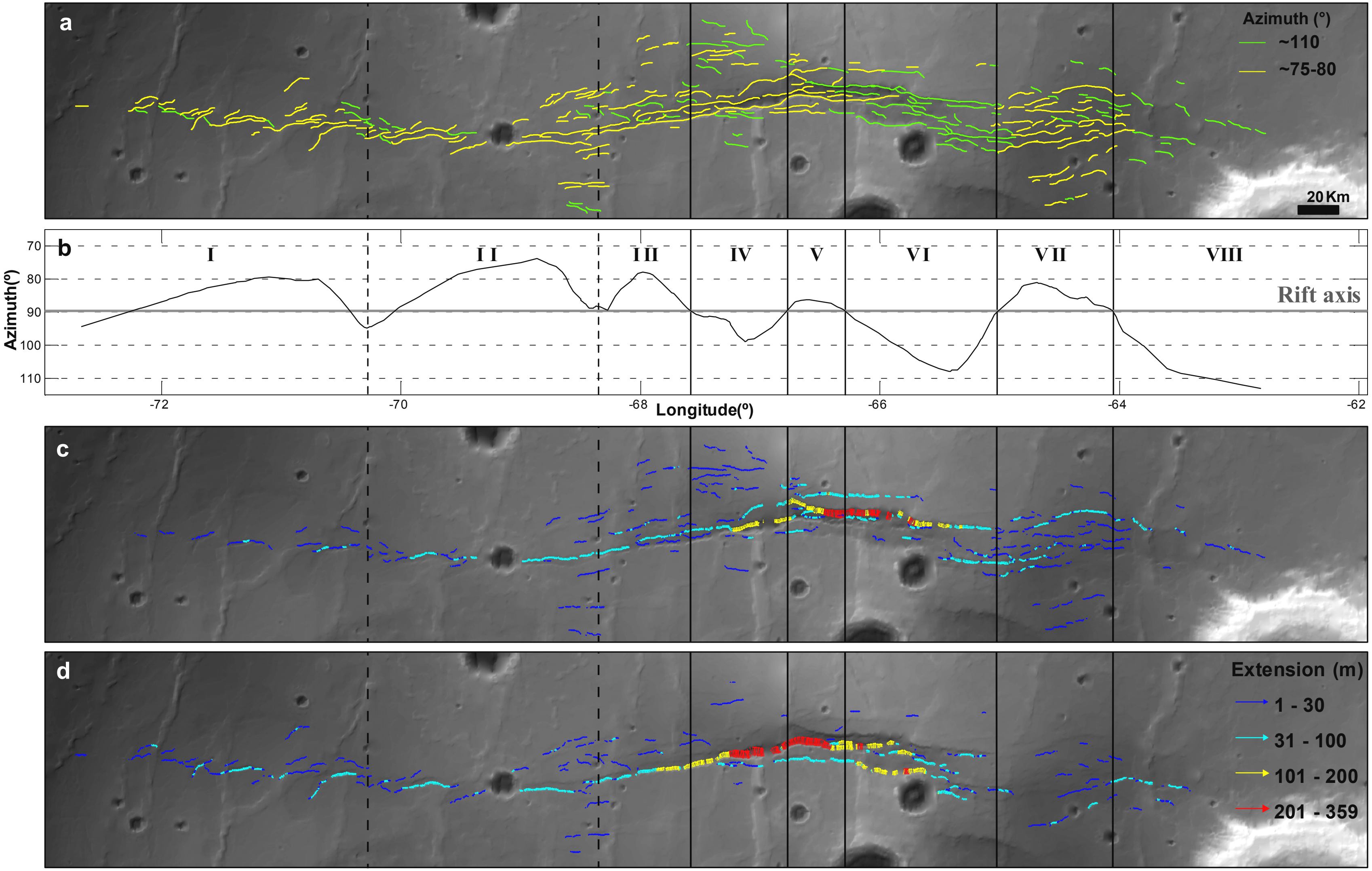

Figure 2.8- See next page for full legend.

Figure 2.8 - North Thaumasia Planum rift strain analysis (see Figure 2.1 for context); (a) two distinct fault sets striking ~75-80º and ~110º; (b) fault azimuth diagram computed on a 0.1° longitude sliding window (mean rift axis azimuth is 89.8 ±0.3º); (c) South dipping normal faults extension vectors; (d) extension vectors associated with North dipping faults. From the azimuth curve eight rift zones were identified. Those zones correspond to breaks in the mean azimuth curve related with alternating striking fault. Dashed boundary lines between zones I, II and III correspond to minor trend variations (see text for discussion).

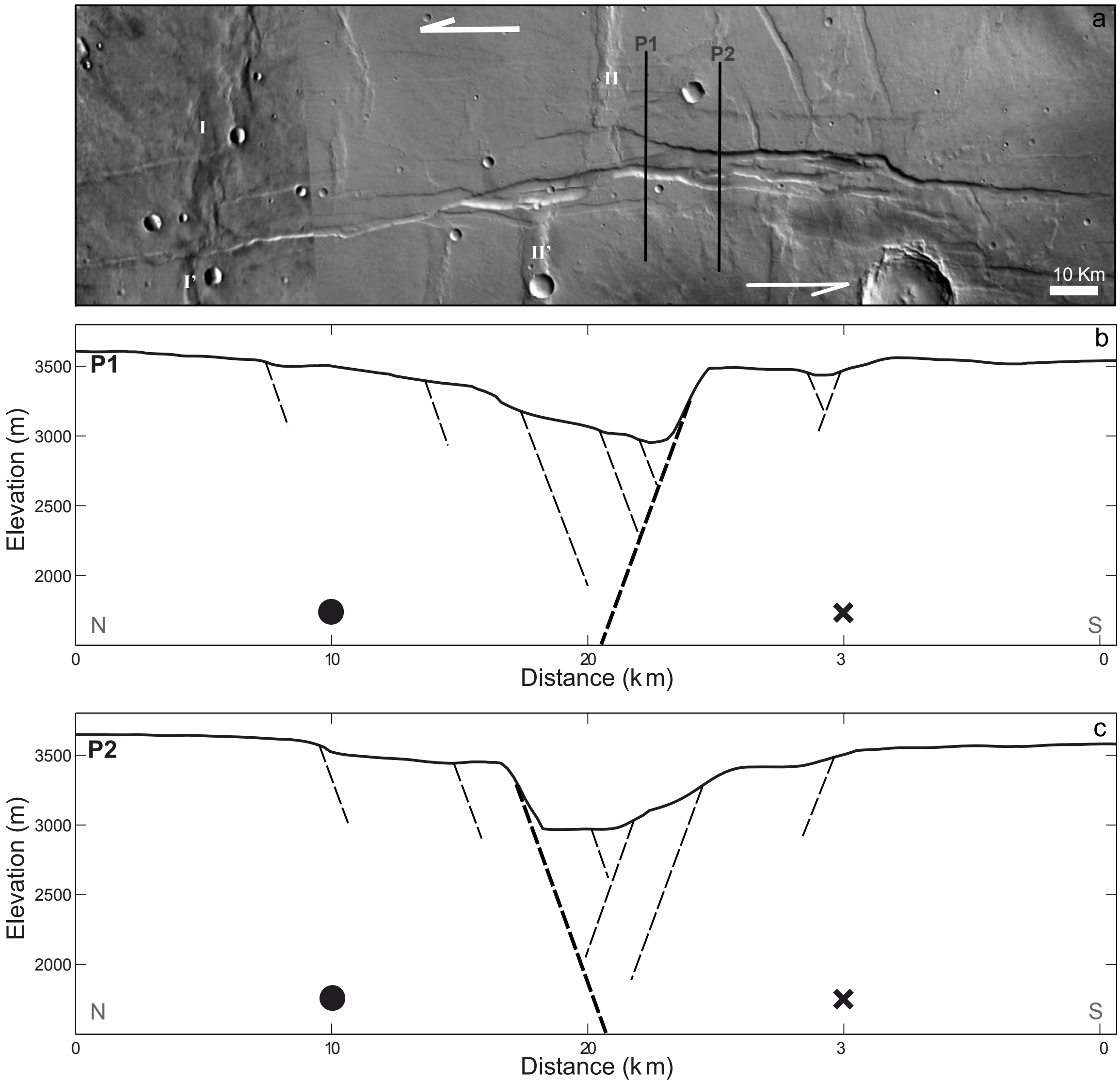

Figure 2.9 - Central part of the rift (see Figure 2.1 for context). (a) THEMIS (left) and HRSC (right) images of the central part of the rift. I-I' and II-II' labels correspond to two wrinkle ridge segments unevenly affected by a right-lateral shear related with the wrinkle ridge formation. White arrows show the relative motion sense of the distinct blocks during rift formation; (b and c) Schematic North-South profiles illustrating the along strike shifting rift polarity. This polarity change is interpreted to be associated with a left-lateral negative flower structure (thicker fault planes represent the dominant fault on each rift segment). Black circle denotes motion outward from the plane of cross section and X represents motion into the plane of cross-section. Faults are represented as planar surfaces with an inferred constant dip angle, even though normal faults

associated with transtensional pull-apart basins can present a more listric nature, with dip angle decreasing with depth (Wu et al., 2009).

The overall geometry and strain distribution is consistent with a possible East-West migration of the deformation. Rifting occurs along pre-existent structures forming pull-apart basins. This scenario is coherent with a sinistral transfer zone located between two different blocks. The Coprates rise edge between these blocks also presents different azimuths, which also supports a differential behavior of the buckling/thrusting between the two blocks (Figure 2.10).

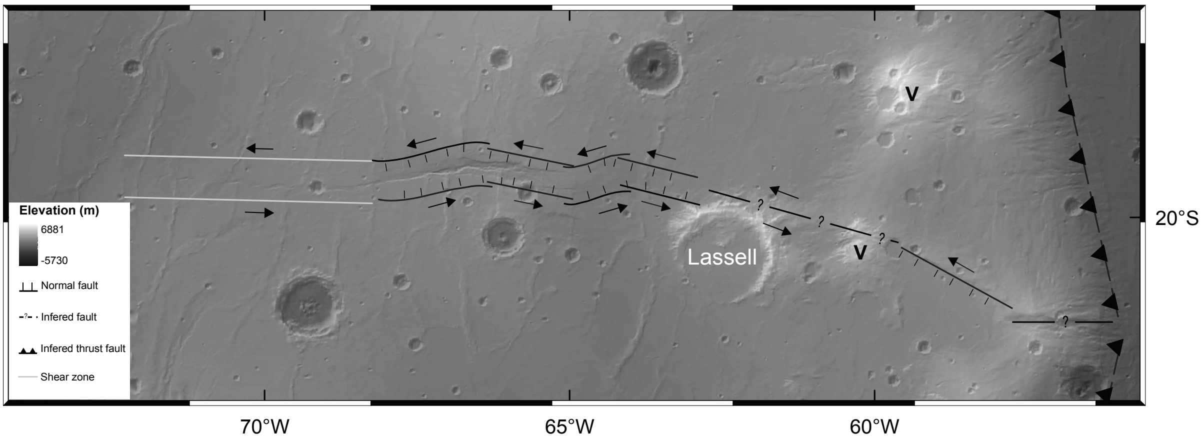

Figure 2.10 - Synoptic tectonic model proposed for the formation of the described rift. Arrows show the relative motion sense between the blocks. The central part of the rift seems to be linked with a more diffuse corridor located East of Lassell crater, which crosses a volcano (V) and reaches the Coprates rise edge. The central rift is composed of alternating striking pull-apart basins. Strains decrease eastward and the easternmost rift section is formed by an en-echelon graben array formed inside a left-lateral shear zone. This zone may correspond to an initial rift formation phase, which implies an East-West migration of the deformation. The overall pattern is consistent with a differential movement accommodation zone between two distinct blocks individualized during Coprates rise thrusting.

2.6 Conclusion

Tectonic structures were automatically mapped using the presented technique. Manual classification constitutes the main obstacle to a complete automation of the lineament mapping process. A supervised classification process using the compiled morphometric attributes will in the future be applied for the automation of this classification stage.

The analysis of synthetic normal fault topography demonstrates that the proposed methodology is capable of automatic extension estimation. The simplicity of the fault model used, the uncertainties related with the amount of sedimentary/volcanic infill and the characteristics of MOLA data make the presented methodology only effective for a relative analysis of the strain spatial distribution associated with the normal faults on Mars surface.

The application of the developed methodologies to the North Thaumasia Planum rift supports the conclusion that this tectonic assemblage corresponds to a differential movement accommodation zone between two distinct blocks. The rift is composed by several segments of pull-apart basins possibly presenting negative flower-structures formed by the reactivation of older strike-slip faults during an inversion episode. An East-West migration of the deformation is proposed, linked to a final stage of the Coprates rise building up.

Pull-apart basins formed along strike-slip extensional step-overs are Earth possible analogues. Pull-apart basins on Earth are generally linked with major strike-slip fault systems such as the North Anatolia transform fault (Barka et al., 2000; Armijo et al., 2002), the East Anatolia (Aksoy et al., 2007) or the Dead Sea fault systems (Brew et al., 2001; Wu et al., 2009). The given examples are all linked with the extrusion of the Anatolia-Aegean block due to the collision of Arabia and Eurasia plates.

The recognition of pull-apart basins, associated to a left-lateral transtensional regime, nearby and subparallel to Valles Marineris, may suggest a similar origin to the Vallis Marineris troughs. A Middle-late Noachian pure extensional episode followed by an Early Hesperian left-lateral reactivation was hypothesized by Borraccini et al. (2007) for the formation of Vallis Marineris. The presented analysis could not exclude that sequence of events, but a unique long-lasting transtensional episode may be more plausible in the context of an eastward differential sliding of the diverse Thaumasia Plateau blocks. The application of the same described techniques to other rift systems can help to better constrain the strains associated with the formation of the Thaumasia Plateau.

3 Tectonic lineament mapping on Mars: comparing methodologies and datasets

3.1 Introduction

Regional lineament mapping constitutes the base for tectonic interpretation on Mars and constitutes one of the standard inputs for the creation of geological and geomorphologic maps. Image mosaics are usually employed, and lineaments are manually digitized and classified by a user (Geographical Information Systems – GIS, are nowadays used to manage all the process).

Several factors can influence the interpretative results, some of them subjective (such as the user experience/motivation or style) but others easily quantifiable, such as the type and spatial resolution of the used datasets. Mosaic artifacts and illumination conditions can also influence the interpretation.

This comparative work will focus in the analysis of the tectonic features mapped in the Thaumasia Planum region (Figure 3.1), a region that presents a rich and varied record of tectonic activity spanning Noachian and Hesperian times (Dohm and Tanaka, 1999).

The present work compares three different mapping efforts. The first two datasets were obtained by the traditional method of photointerpretation using different imagery datasets. The objective of comparing those datasets is to constrain some of the causes that can influence the lineament mapping and subsequent tectonic interpretation.

The third case corresponds to a semi-automatically dataset obtained. An automatic algorithm to extract and characterize all the scarps present on the surface has been applied. The extracted lineaments were then classified by a user according to their significance. The aim is to evaluate the accuracy and possible bias associated with the automatic recognition procedure.

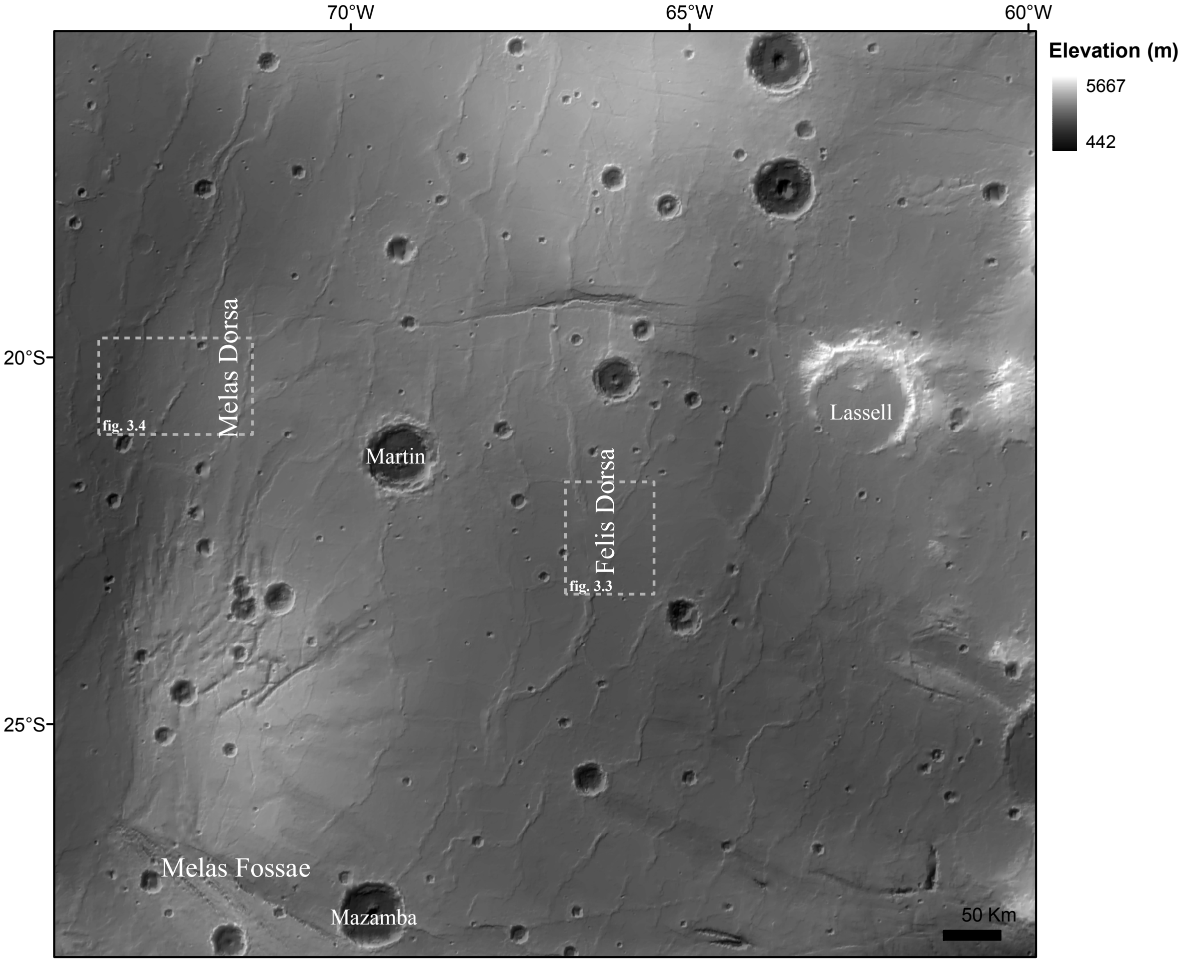

Figure 3.1- Shaded relief topography of the studied area. Dashed areas correspond to the regions shown in following figures.

3.2 Data and methodology

Dataset I corresponds to a section of the paleotectonic map of the Thaumasia region (Dohm and Tanaka, 1999; Dohm *et al.*, 2001b).

Dataset II corresponds to the detailed tectonic analysis of the eastern margin of the Thaumasia Plateau presented by Borraccini et al. (2007).

Finally, dataset III present the tectonic features automatically extracted and classified as described in the previous chapter.

3.2.1 Dataset I

Dohm and Tanaka (1999) mapped tectonic lineaments using Viking images and a 1:2,000,000-scale photomosaic base. The lineaments were then compiled on a GIS database at 125 m/pixel spatial resolution.

Several typologies of compressive tectonic features were originally defined (mare-type wrinkle ridge, narrow subdued ridge, subdued mare-type wrinkle ridge, etc.). Those typologies characterize in more detail the different morphologies of the structures. The Authors did not report strike-slip faulting or identify shear sense.

The main attributes attached to each lineament are length, trend, age and the stratigraphic unit to which it belongs.

For comparison purposes only two classes will be used, normal faults (NFs) and wrinkle ridges (WRs), including respectively all the types of distensive and compressive structures.

3.2.2 Dataset II

The mapped structures in dataset II correspond to the more detailed structural mapping made by Borraccini et al. (2007). The Authors used Viking MDIM 2.1 mosaic (231.4 m/pixel), THEMIS infrared daytime mosaic (100 m/pixel) and a HRSC mosaic with 50 m/pixel spatial resolution datasets to map tectonic lineaments on a GIS platform.

Borraccini et al. (2007) put emphasis in the recognition and characterization of the features from a structural rather than morphological point of view. Three main categories, NFs, WRs and strike-slip faults were used to classify the mapped lineaments. Oblique NFs and WRs as well as pure strike-slip faults, were recognized in the studied area. A two level classification consisting in the type (NFs or WRs) and the recognition of horizontal shear associated with the tectonic lineaments was adopted (the shear sense was not defined).

In the present comparison only two classes will be used, NFs (including all the pure and oblique distensive features) and WRs (enclosing all the pure and oblique compressive structures). Pure strike-slip faults were distributed between the two classes depending on the context on which they appear.

The attributes computed for each lineament were length and mean trend.

3.2.3 Dataset III

Dataset III was generated semi-automatically. All the mapped lineaments were automatically derived from a MOLA (Mars Orbiter Laser Altimeter) (Zuber et al., 1992;

Smith et al., 2001) digital terrain model (DTM). A DTM with ~231 m/pixel was interpolated from the MOLA precision experiment data records following the procedure described by Okubo et al. (2004) applying the natural neighbor interpolation technique (Abramov and McEwen, 2004).

The algorithm presented in chapter 2 proved to be capable of automatic extraction of the topographic discontinuities present on Mars surface. Lineaments accurately mark the inflexion points of the scarps (the point of the scarps where the profile curvature is zero) which allow the computation of several morphometric attributes for each scarp (Vaz et al., 2008).

The automatic procedure of scarp recognition is fully automated and reproducible. Then a user performs a classification stage on a GIS environment by superimposing the identified lineaments on the available imagery. THEMIS daytime infrared (100 m/pixel), HRSC imagery (25 m/pixel) and CTX imagery (10m/pixel) were the used datasets. Images were not mosaicked so that overlapping areas were always available and mosaic artifacts were avoided.

The algorithm extracts all the scarps present in the DTM. Tectonic processes are not the only ones that generated scarps on the surface of Mars. At a regional scale, other processes such as cratering, erosion or volcanism produced scarps also recognizable at the DTM spatial resolution. Besides the classification of the tectonic related scarps, a wider classification of all the scarps according to their genetic origin was performed.

The classification scheme of dataset II was extend for the tectonic scarps. A three level classification scheme allowed the registration of the type of structure, the degree of preservation (if the scarps presented clear signs of erosion) and the inferred sense of horizontal shear related with oblique features (left- or right-lateral). Pure strike-slip faults were not recognized. By definition, pure strike-slip faults do not produce a strong topographic signature, which implies that they will not be recognizable by the automatic algorithm unless they displace other structures producing linear scarps. This makes that only oblique distensive and compressive tectonic features were identified.

Only the first level of classification, the type of structure, will be compared in this chapter.

3.3 Qualitative comparison

At a first glance, all the three maps in Figure 3.2 seem similar. Several patches presenting predominantly NFs or WRs are common to all the datasets. The NFs located in Melas Dorsa and Melas Fossae are visible in all the datasets. An East-West array of NFs is also clearly visible between Melas Dorsa and Lassell crater (the same rift system analyzed in section 2.5.2). Three separated regions with NFs are also recognizable in the northern border of the analyzed area in the three datasets.

The spatial distribution of the regions with WRs and the overall North-South trend for the majority of the WRs are a common mark between the three datasets. The spacing between WRs consistently decreases eastward on the three cases despite dataset III presenting a higher number of lineaments.

A greater correspondence is evident between datasets I and II. Due to the lower spatial resolution of the image mosaics used to map the structures in dataset II, more structures and better detail is obtained. Note, however, the different criteria used to map the WRs in Figure 3.3d and e. WRs are represented only with one long line segment in dataset I, while individual scarps were discriminated in case II. Only one of the scarps is mapped when WRs appear to be asymmetric (Figure 3.3e). Those observations reflect, not only, the different spatial resolution of the used imagery data, but also, a regional vs. local mapping approach.

One NE-SE striking WR is not completely represented in dataset II. One possibility is that the mapping of this particular area was performed using the HRSC image presented in the Figure 3.3a (it is not possible to know certainly which dataset, or datasets, were used on a particular area). Note the differences between the HRSC and THEMIS images (Figure 3.3a and b). The referred WR is more evident in the THEMIS data due to the different sub-solar angles (the direction of the Sun at the time the image was acquired). In the HRSC image, sub-solar angle is approximately parallel to the missing WR which could justify the non-recognition of this structure.

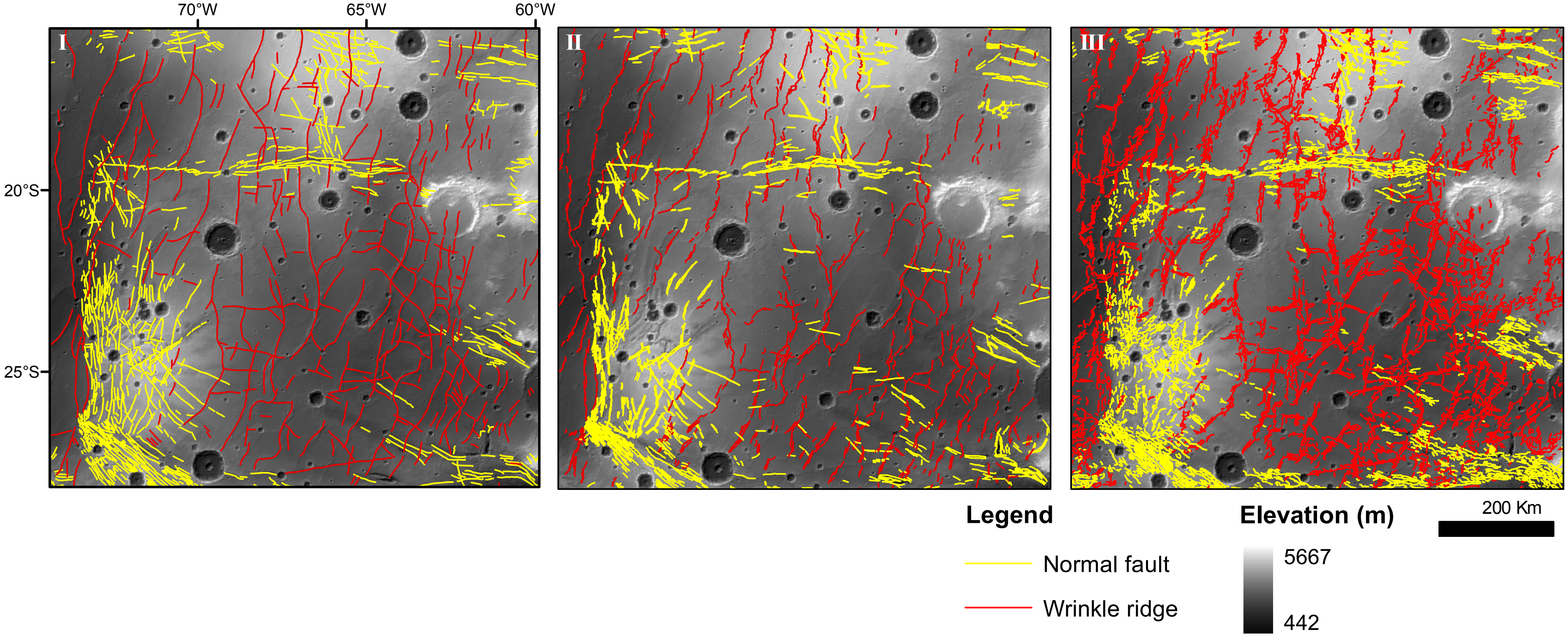

Figure 3.2 – The three compared datasets: I - paleotectonic map of the Thaumasia region (Dohm and Tanaka, 1999; Dohm *et al.*, 2001b); II – Borraccini et al. (2007) structural mapping; III – semi-automatically derived lineament map. Lineaments representing tectonic features in Mars surface are superimposed in MOLA shaded relief topography.

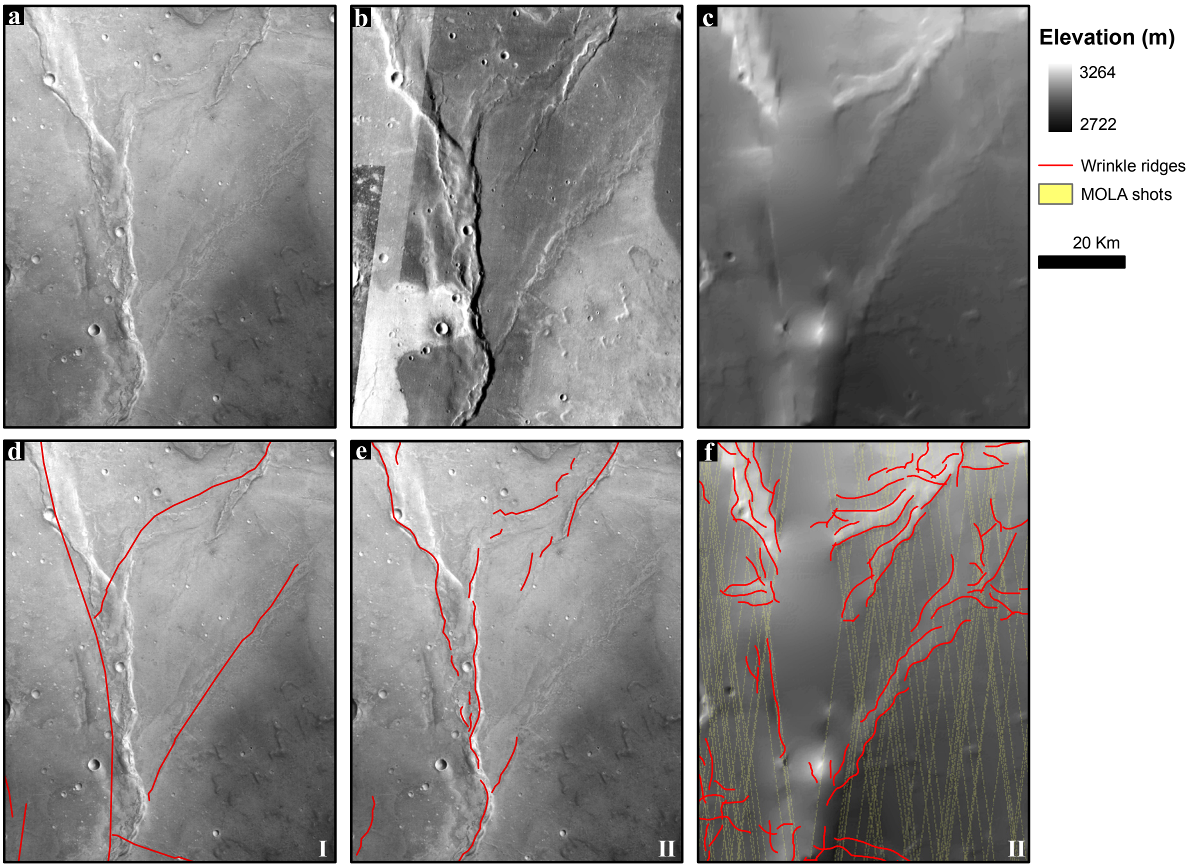

Figure 3.3 - HRSC image (a); THEMIS infrared imagery (b), MOLA shaded relief topography (c); dataset I mapped WRs and HRSC image (d); dataset II WRs and HRSC image (e); dataset III mapped WRs, MOLA shaded relief topography and MOLA data shots location (f). See text for discussion.

The comparison of the mapped tectonic features in this region illustrates well one of the parameters that can influence the photointerpretation: the different illumination conditions can mask some of the structures, depending on their preferential trend. This unconstrained parameter can introduce a directional bias on the final mapping results, making relevant the use of different images acquired with different illumination conditions.

MOLA data is not influenced by illumination conditions; however, coarse resolution and data interpolation gaps have an effect on the mapping results. Lineament continuity is affected, with the consequence that each WR is decomposed on a set of scarps. Altimetry data allow the definition of even the secondary corrugations that form the more complex WRs (Figure 3.3f).

The main problem that is visible in Figure 3.3f is the lack of part of the larger ~N-S WR. Only the East-dipping scarp is identified due to a larger gap between the

MOLA tracks. The gaps sizes are variable, but all have a NS trend due to the same approximate trend of the MOLA tracks. Thus, a directional bias is expected, leading to the underestimation of the ~NS striking features (see section 3.4.4 for a bias estimation and correction).

The obtained lineaments, shown on dataset III, coarsely represent the features identifiable from higher resolution imagery. Nevertheless, at a regional scale, MOLA data provide the possibility of a full morphometric characterization that could be used, as shown in chapter 2, for strain estimation purposes.

In dataset III WRs scarps are systematically mapped. The two main bounding scarps, presenting opposite dipping directions, are always recognized as are secondary scarps related with more complex WRs. The same is not true for the lineaments of dataset II. The two bounding scarps are only mapped where WRs symmetry is apparent. Deducing asymmetry from imagery alone should also be avoided since illumination bias could lead to misinterpretations (compare the apparent asymmetric geometry of the WRs in Figure 3.3a with the THEMIS image and MOLA altimetry of Figure 3.3b and e).

A set of NNE-SSW WRs and three sets of grabens (striking NS, NW-SE and EW) are the tectonic features observable in Figure 3.4. The same WRs are present in datasets I and II, although dataset II shows more segmented lines.

In Figure 3.4e only one line represents WRs. Figure 3.3e and Figure 3.4e show that, for dataset II, a unique mapping criterion was not followed across the entire area.

For the region depicted in Figure 3.4 the NFs in dataset I correspond approximately to the same NFs present on dataset II. Some EW grabens are absent in dataset II, but present in the eastern region displayed in Figure 3.4d and partially on Figure 3.4f. There are also cases of unique features, only present in one of the datasets exist.

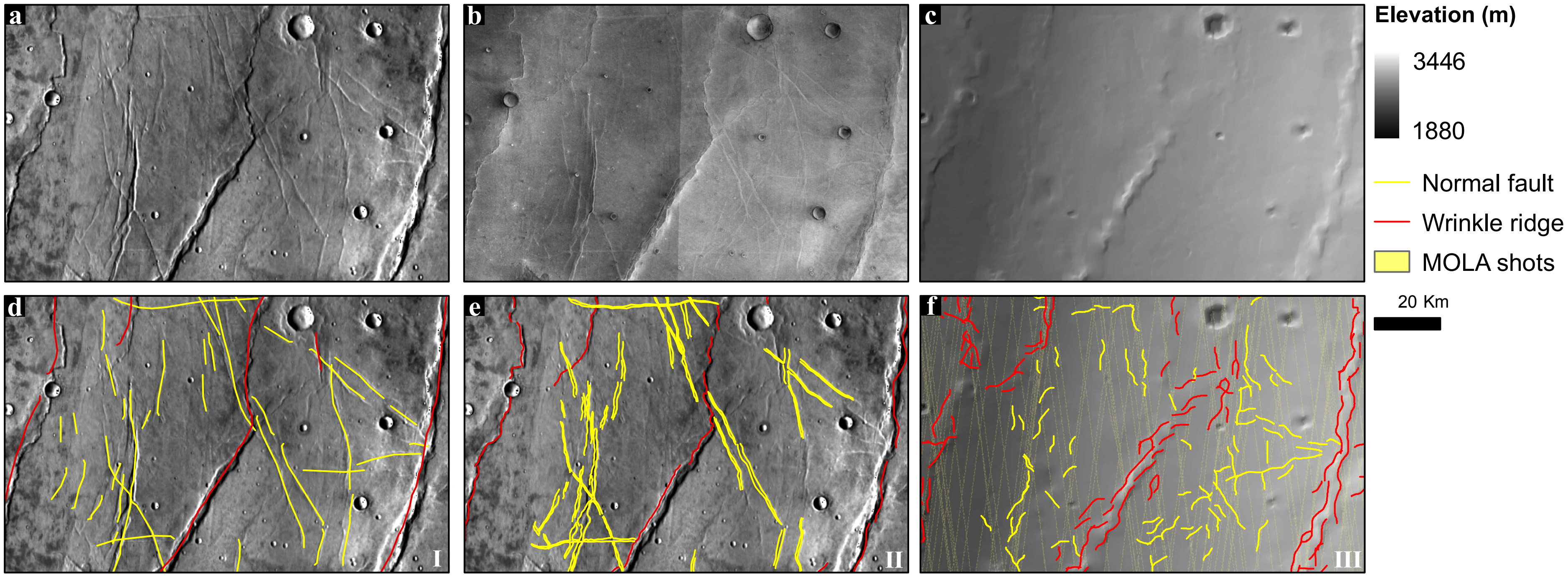

Figure 3.4 - THEMIS infrared images (a); HRSC images (b), MOLA shaded relief topography (c); dataset I and THEMIS IR image (d); dataset II and THEMIS IR image (e); dataset III, MOLA shaded relief topography and MOLA data shots location (f). See text for discussion.

Lines in dataset I represent grabens and not individual NFs. On the contrary, NFs are individualized in dataset II, at least doubling the number of recognized structures. When compared with datasets I and II, dataset III (Figure 3.4f) presents a different array of tectonic features. WRs are better represented than NFs since DTM resolution does not allow the recognition of the majority of the narrow grabens. The widths of the grabens in this region, do not exceed 1.5 km, thus the fault-bounded depressions are not fully recognizable from MOLA DTM (Figure 3.4c). Smaller scarps are only partially identified in regions where track gaps are narrow.

Datasets I and II seem more closely related among them when compared with dataset III. The main differences between datasets I and II arise from the level of detail and the criteria used to map the tectonic features.

At a regional level, all the major structures represented in datasets I and II are also present in dataset III. Locally, dataset III lineaments are influenced by the quality and resolution of the MOLA DTM.

3.4 Quantitative comparison

Despite the differences in style and scope of the three presented datasets a quantitative comparison was performed by evaluating the accuracy in the location of the mapped lineaments and lineament density.

A comparative directional analysis is also presented. Directional statistics are by far the more relevant parameter, since fault strikes are tightly linked to the stress fields responsible for their formation.

3.4.1 Map consistency

Confusion matrices are commonly used to evaluate the accuracy of pattern recognition techniques (Tso and Mather, 2001). In remote sensing studies, classified matrices are usually compared with ground truth datasets or reference datasets. As shown in the qualitative analysis, the two photointerpretations present differences, making difficult the choice of a unique reference dataset. To address this problem and at the same time perform the quantitative evaluation of the semi-automatic algorithm, both datasets (I and II) are used as reference datasets.

The confusion matrices will be used to access not only the accuracy of the semi-automatically derived lineaments, but also to compare the two photointerpretations. Since a unique ground truth dataset was not defined, all the computed accuracy values are values of relative accuracy.

Rasterisation and downsampling to a common spatial resolution allows to reduce the impact of the different interpretation styles, and to reduce the impact of the different imagery and altimetry spatial resolutions used for mapping the lineaments. The rasterisation and downsampling will have two major implications: an additional class will be necessary (defining the locations where NFs and WRs exist in a same pixel area) and the parameters derived from the confusion matrices will vary with the chosen pixel size. The analysis is performed at 3 km/pixel and 10 km/pixel so that the impact of varying spatial resolutions can be evaluated (Figure 3.5).

Two parameters will be used to infer the degree of agreement between the mapped lineament spatial distributions, Kappa index ($\hat{k}$) and overall accuracy (*oa*). The *oa* usually yields higher rates of agreement than $\hat{k}$. The comparative assessment of measures of map accuracy presented by Liu et al. (2007) discourages the use of the $\hat{k}$ (because of the impossibility to evaluate the correctness of the model of chance) and recommends the use of the *oa* as a primary standard measure of map accuracy.

The overall accuracy is defined as:

$$oa = \frac{\sum_{i=1}^{r} x_{ii}}{N} \cdot 100 \qquad \text{(Eq. 3.1)}$$

where r is the number of classes, x_{ii} is the (i, i) element of the confusion matrix (the elements on the main diagonal of the matrix) and N the number of samples. Values range from 0 to 100%, with 100% denoting a perfect agreement between the mapped classes.

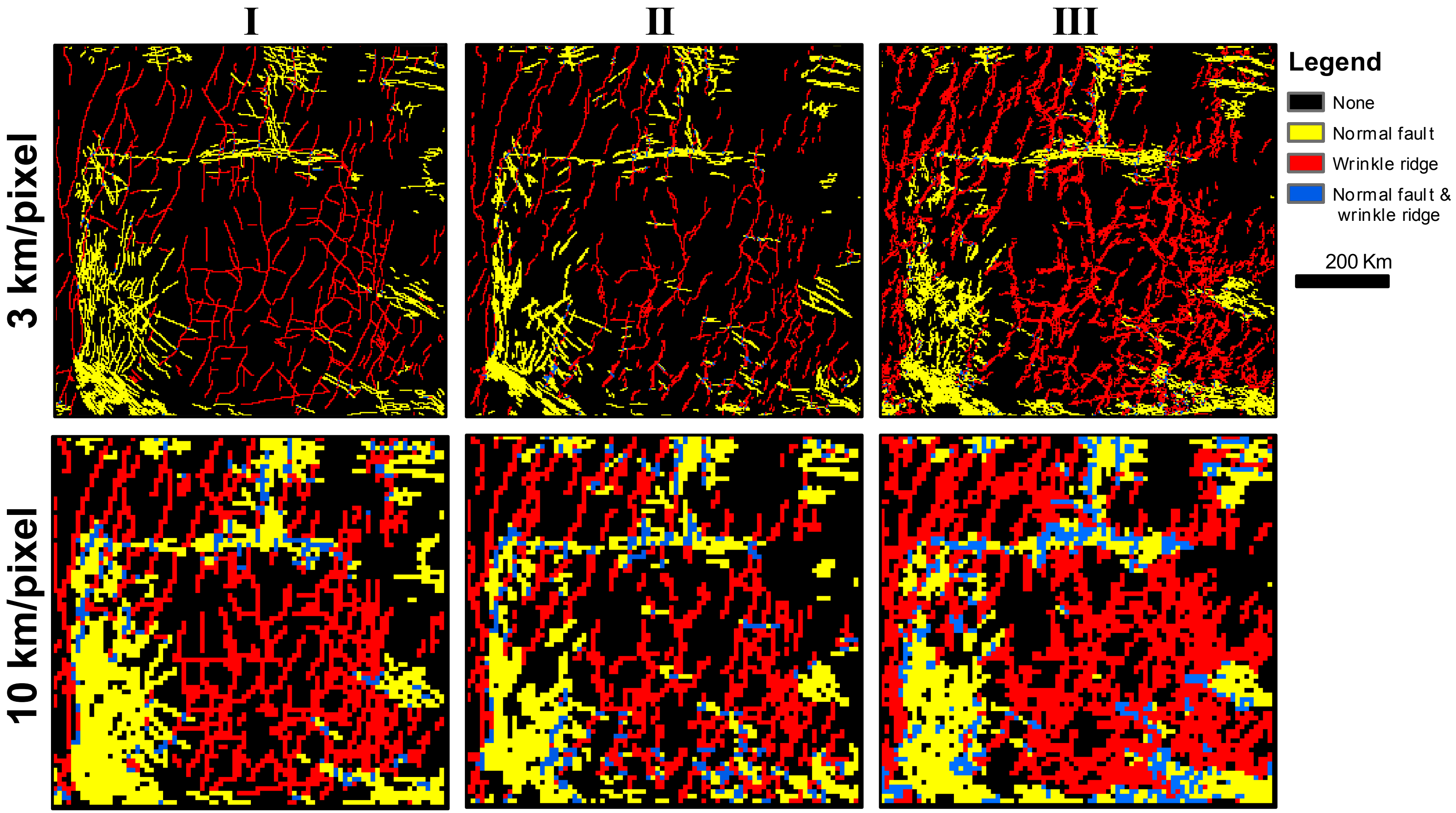

Figure 3.5 - Rasterization and downsampling of the datasets I, II and III (from left to rigth). Two spatial resolutions, 3 and 10 km/pixels are presented in the first and second rows. Rasterization and downsampling of the WRs and NFs lineaments originates a third class (NF&WR) representing the areas where both classes are present. Class “none” correspond to the absence of any mapped feature on a certain area.

Kappa index was computed according to

$$\hat{k} = \frac{N\sum_{i=1}^{r} x_{ii} - \sum_{i=1}^{r}(x_{i+} \cdot x_{+i})}{N^2 - \sum_{i=1}^{r}(x_{i+} \cdot x_{+i})} \qquad \text{(Eq. 3.2).}$$

The partial totals of row i and column j correspond to x_{i+} and x_{+i} (Tso and Mather, 2001). Kappa index gives a measure that indicates if the confusion matrix is significantly different from a random result (Smits et al., 1999). Kappa values range from 0 to 1, with 1 denoting a perfect agreement and 0 a random non-agreement case.

Table 3.1 presents the percentage of pixels on each class. Class "none" is the more frequently represented for the two resolutions of analysis and for the three datasets. Percentages for datasets I and II display a higher affinity when compared with the percentages obtained for dataset III. The main difference is the percentage of pixels classified as "WR" that in case III present approximately the double percentage of the "WR" pixels in datasets I and II.

Overall accuracy values indicate a higher accuracy rate between datasets I and II (82 and 72% for 3 and 10 km/pixel). Lower values are obtained for the cases where dataset III accuracy is evaluated. Comparable accuracy values were obtained for the I-III and II-III cases (74-76% and 67-66% for the 3 and 10 km/pixel respectively).

Table 3.3 $\hat{k}$ values can be considered low for all the compared datasets and resolutions. For the 3 km/pixel case, the range of the obtained values indicates a fair strength of agreement between the three datasets, using the nomenclature proposed by Landis and Koch (1977). Higher and comparable degrees of agreement correspond to the evaluation of datasets I-II and II-III. For the 10 km/pixel case, values correspond to a moderate strength of agreement. At this scale of analysis, a higher agreement is found between datasets I and II. Dataset III agrees equally well with datasets I and II ($\hat{k}$ of 0.51 and 0.49 respectively).

In all the datasets the "none" class exceeds by far the percentage of the other classes (see Table 3.1). Overall accuracy and Kappa index do not compensate unequal class sizes (Smits et al., 1999), but since the *oa* only takes into account the values in the main diagonal of the confusion matrices, it should be more affected by different class sizes. The values of $\hat{k}$ increase with increasing pixel dimension, but the contrary behavior is observed for the *oa* that surprisingly decreases. In fact, a higher disparity between the values of *oa* and $\hat{k}$ exists for the 3 km/pixel resolution, a case for which the class percentages are more unbalanced. These observations support the view that $\hat{k}$ may be a more robust parameter for estimating the agreement degree for the presented cases.

Table 3.1 - Pixel class percentage. Note the much higher proportion of the "none" class in all the cases and the higher differences between the percentages of pixels in the "WR" class.

	3 km/pixel			10 km/pixel		
	I	II	III	I	II	III
None	82.7	83.7	70.4	53	58	38.5
NF	8.9	8.2	10.8	19.4	16.4	17
WR	8.2	7.6	18.1	23.9	20.7	36.4
NF&WR	0.2	0.5	0.7	3.7	4.9	8.1

Table 3.2 - Confusion matrices for the images of Figure 3.5. The matrices allow the comparison of each dataset with the other two, allowing not only to assess the quality of the semi-automatically extracted lineaments, but also to compare both photointerpreted datasets. Four classes were defined according to the tectonic features mapped at each pixel: normal faults (NF); wrinkle ridges (WR); normal faults and wrinkle ridges (NF&WR correspond to cases where more than one type of structure is contained on a same area); non-existence of any feature (none). The analysis was performed at 3 and 10 km/pixel spatial resolutions. Matrices diagonal values (gray cells) correspond to the true positives (areas belonging to the same class in the compared datasets). See Table 3.3 for the overall accuracies and kappa index derived from the matrices.

3 km/pixel						10 km/pixel					
II - I	None	NF	WR	NF&WR	Total	II – I	None	NF	WR	NF&WR	Total
None	57668	3379	3501	68	64616	None	3097	405	497	38	4037
NF	2852	3259	193	46	6350	NF	215	820	46	63	1144
WR	3178	136	2506	34	5854	WR	335	46	1003	57	1441
NF&WR	174	88	110	28	400	NF&WR	42	79	118	105	344
Total	63872	6862	6310	176		Total	3689	1350	1664	263	
III - II	None	NF	WR	NF&WR	Total	III - II	None	NF	WR	NF&WR	Total
None	50880	1990	1413	83	54366	None	2464	131	76	8	2679
NF	4359	3761	122	82	8324	NF	372	737	33	39	1181
WR	9130	454	4232	181	13997	WR	1076	104	1220	143	2543
NF&WR	247	145	87	54	533	NF&WR	125	172	112	154	563
Total	64616	6350	5854	400		Total	4037	1144	1441	344	
III - I	None	NF	WR	NF&WR	Total	III - I	None	NF	WR	NF&WR	Total
None	49499	2701	2131	35	54366	None	2295	208	168	8	2679
NF	4448	3689	129	58	8324	NF	263	857	19	42	1181
WR	9628	331	3978	60	13997	WR	1020	82	1365	76	2543
NF&WR	297	141	72	23	533	NF&WR	111	203	112	137	563
Total	63872	6862	6310	176		Total	3689	1350	1664	263	

Table 3.3 - Overall accuracy and Kappa index of agreement for Table 3.2 confusion matrices.

	3 km/pixel			10 km/pixel		
	I - II	II - III	I - III	I - II	II - III	I - III
oa	82,18	76,31	74,05	72,14	65,68	66,81
$\hat{k}$	0,39	0,39	0,34	0,54	0,49	0,51

3.4.2 Unique recognitions

The qualitative comparison allowed the identification of several structures that were only present in one of the datasets. An approximate measurement of the ratio of those unique structures can be derived from the confusion matrices, by computing for each class in one dataset the percentage of pixels misclassified as "none" class.

This allows to evaluate which dataset possesses more unique features, in other words which dataset possess a higher degree of information since “none” pixel areas correspond to areas where tectonic activity was not recognized. Note however that, as expected, the absolute values are highly sensitive to resolution differences (see Table 3.4).

Table 3.4 - Partial and total percentages of misclassified pixels in “none” class for each dataset on the six confusion matrices of Table 3.2. Total column correspond to the join percentage for NF, WR and NF&WR classes.

		3 km/pixel				10 km/pixel			
		NF	WR	NF&WR	Total	NF	WR	NF&WR	Total
I-II	I	49,2	55,5	38,6	52,1	30,0	29,9	14,4	28,7
	II	44,9	54,3	43,5	49,2	18,8	23,2	12,2	20,2
II-III	II	31,3	24,1	20,8	27,7	11,5	5,3	2,3	7,3
	III	52,4	65,2	46,3	60,1	31,5	42,3	22,2	36,7
I-III	I	39,4	33,8	19,9	36,5	15,4	10,1	3,0	11,7
	III	53,4	68,8	55,7	62,9	22,3	40,1	19,7	32,5

Positive recognition of unique tectonic structures between datasets I and II have similar total ratios. For the 3 km/pixel case, 52.1% of the misclassified pixels in dataset

I were not mapped in dataset II as any tectonic structure. A 49.2% ratio was computed for the proportion of misclassified pixels in dataset II not mapped in dataset I. For the higher spatial resolution case, 28.7% versus 20.2% ratios were considered unique recognitions for datasets I and II respectively.

When compared with dataset II, dataset I consistently presents a higher percentage of unique positive recognitions. Higher differences between unique recognition ratios correspond to NFs (49.2 - 44.9% and 30.0 - 18.8% for 3km and 10km cases). This fact is clearer in the 10 km/pixel representation of Figure 3.5, where large areas with NFs in dataset I are absent in dataset II.

Dataset III has the higher ratio of unique recognitions when confronted with the other two datasets (62.9% and 60.1% of new recognitions when compared with datasets I and II at 3 km/pixel resolution). This is surely related not only with the positive identification of new tectonic features, but also with the more complete mapping of the WRs morphologies (Figure 3.3). In fact, WRs ratios for dataset III are the highest ones, which is clearly visible in the larger extent of WRs pixels in the 10 km/pixel representation in Figure 3.5.

3.4.3 Lineament density

Lineament density was evaluated for a 3km/pixel grid using a circular kernel with 40 km radius. The two types of mapped structures, WRs and NFs were analyzed simultaneously. Two different densities were computed: line density (LD) corresponds to the number of lines per area unit while line length density (LLD) corresponds to the line length per area unit. The first density evaluates the degree of fragmentation of the mapped lineaments while the second is useful for a local assessment of the total length of the mapped lineaments.

Dataset III has the higher values of LD (Figure 3.6d to Figure 3.6f) dispersed over a wider area. LD values increase from dataset I to III but all the LD local maxima of datasets I and II are also recognizable in dataset III. This agrees with the qualitative evaluation made in section 3: different mapping criteria produce different numbers of mapped lines.

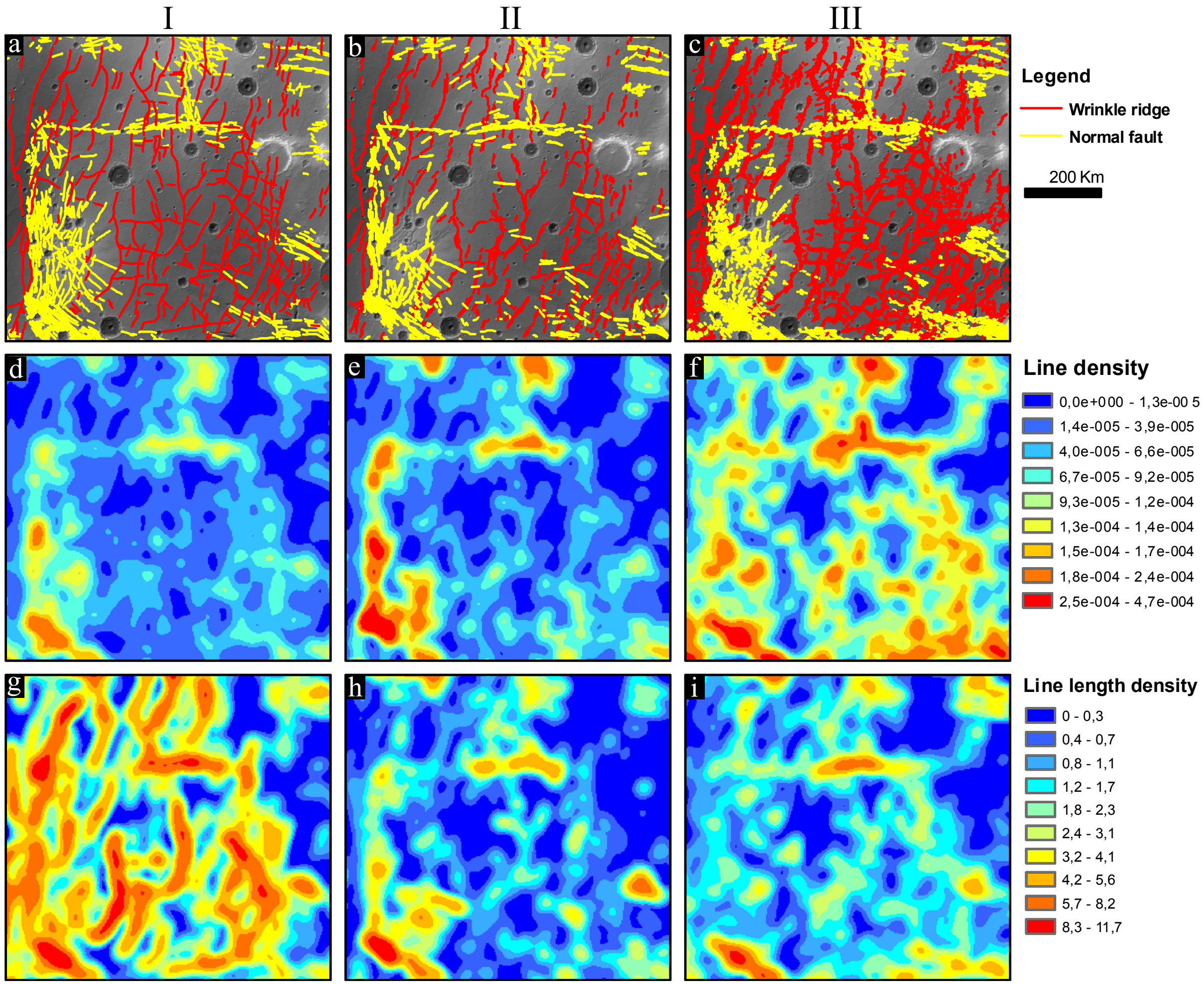

Figure 3.6 – Mapped tectonic structures for dataset I, II and III (Figure 3.6a to Figure 3.6c). Line densities computed for a 3 km/pixel grid, using a circular kernel with 40km radius. Two different densities were computed: line density (LD) corresponds to the number of lines per square meter (Figure 3.6d to Figure 3.6f) while line length density (LLD) correspond to the line length per square meter (Figure 3.6g to Figure 3.6i).

Dataset I presents a very different LLD arrangement (Figure 3.6g), this is due to the fact that mapping was performed using longer line segments. A higher number of common features are recognizable between datasets II and III. The analogous location and intensity of the local maxima is noticeable. Some exceptions are the local maxima located north of Melas Fossae (eastern border of the analyzed area), missing in dataset III LLD map (see Figure 3.6h and Figure 3.6i). This is the same area described in Figure 3.4, characterized by narrow ~NS striking grabens that were not fully mapped by the semi-automatic procedure.

A correlation attempt between LLD values was made for descriptive purposes only (Figure 3.7). For a perfect correlation between the LLD values, plotted values should be located along a straight line with slope 1 (the dashed lines in Figure 3.7 plots). A linear regression was performed in order to rank the correlation degree between the three datasets.

A lower degree of correlation exists between dataset I LLD and the other two analyzed datasets. Dataset I LLD is clearly biased, consistently presenting higher values when compared with datasets II and III (this is reflected in lower values of a in the I-II and I-III case). A better correlation exists between datasets II and III (higher value of a and lower root mean squared error). In this case, the regression analysis indicates higher values of LLD for the dataset II.

It is possible to conclude that dataset II presents the higher LLD values, and that a higher correlation exists between the measured LLD for datasets II and III.

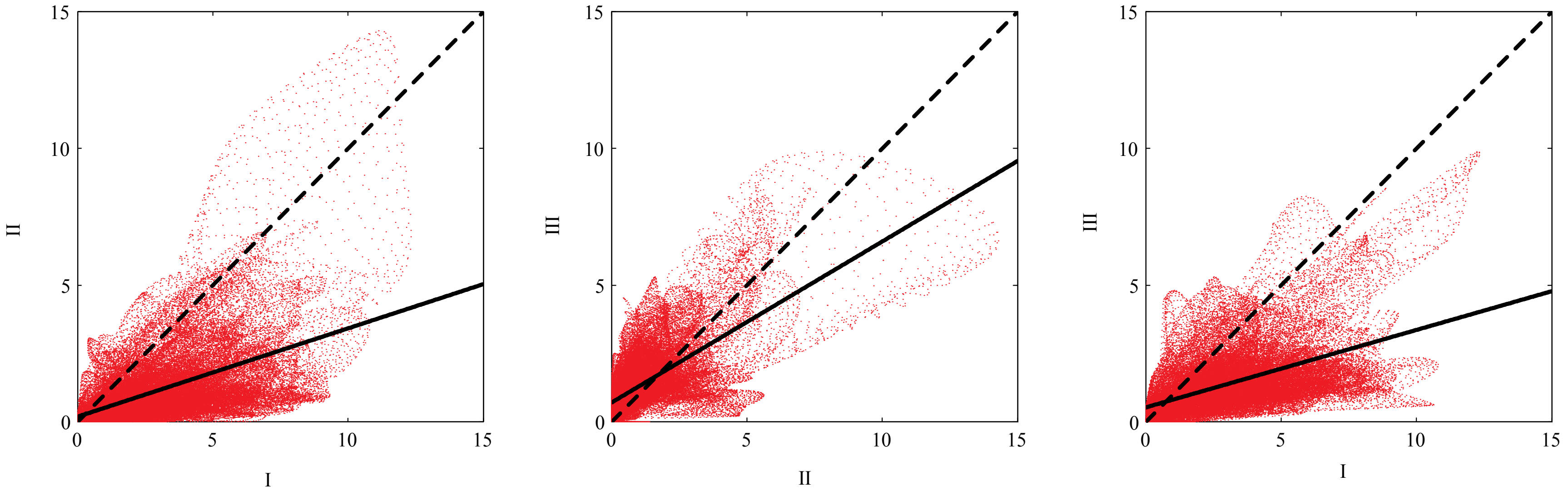

Figure 3.7 – Feature space of the line length density values shown in Figure 3.6g to Figure 3.6i for the combinations of datasets I, II and III. Dashed lines correspond to a perfect correlation case while thick lines correspond to the linear regression lines obtained for comparative correlation purposes.

Table 3.5 - Parameters for the LLD fitted linear models (with the form *f*(*x*)= *a***x*+*b*) between the three datasets shown in Figure 3.7. RMSE stands for the fitting root mean squared error.

	a	*b*	RMSE
I - II	0,32	0,19	1,14
II - III	0,59	0,71	0,88
I – III	0,28	0,53	1,01

3.4.4 Directional analysis

Length weighted rose diagrams are one of the methods commonly employed to study the tectonic stress fields orientations and intensities from remote sensing data (Wilkins and Schultz, 2003; Bistacchia et al., 2004; Borraccini et al., 2007). All the plots presented in this work refer to length weighted circular histograms with 3° bins. WRs and NFs were analyzed separately because their trend is differently related with the orientation of the principal stress (σ_1).

Geodetic measurements of length and azimuth where taken for the three datasets. Considering that, measuring the azimuths between the extremities of the polylines would not take into account the azimuth variation of sinuous lines, the computed azimuth for each line corresponds to the length-weighted mean azimuth measured between all the polyline nodes.

As pointed in section 3.3, a directional bias may be present in dataset III due to the preferential orientation of the MOLA ground tracks. Since the automatic algorithm extracts all the scarps, one possibility is to study the bias related with the mapping of crater scarps. Craters are nearly isotropic circular structures with scarps presenting a variety of lengths and heights. This make them ideal to estimate the circular bias associated with the mapping of any other feature. This circular bias is latitude dependent, since spacing between MOLA tracks decreases poleward. Thus, should the semiautomatic procedure be applied to the entire planet, a differential correction should be used according to the latitude of analysis.

Asymmetric and highly degraded craters, as well as craters not completely contained in the analyzed area were excluded from the directional analysis (see Figure 3.8 map). If no bias were present, a uniform distribution would be expected for the circular distribution in the rose diagram on Figure 3.8 rose diagram. Rayleigh uniformity test excludes the hypothesis of uniformity at a 95% confidence level (Mardia and Jupp, 1999; Jones, 2006).

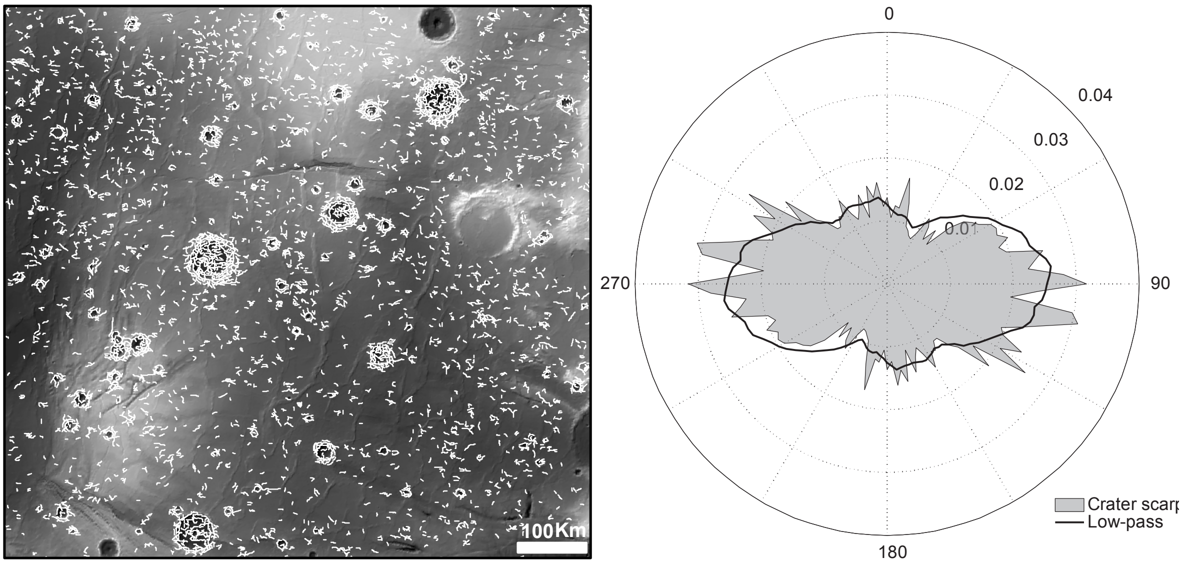

Figure 3.8 – Lineaments classified as crater scarps (left map) used to generate a corrective circular distribution. Note that craters located in the map border as well as highly degraded craters were excluded from the analysis. Length weighted circular distribution for the crater scarps (grey patch in the right circular diagram). Circular distribution represented by a black line correspond to the circular distribution used to correct the directional bias associated with MOLA data. This distribution was obtained by aligning the mean vector of the measured distribution with the E-W axis and by applying a low-pass mean filter.

A mean azimuth of 97.7° was obtained for the crater scarps distributions. This indicates that NS striking crater scarps are underestimated, which agrees with the overall assumption, that any NS scarps would be underestimated by the automatic mapping procedure when using MOLA derived DTMs. Assuming that crater scarps shall not present a preferential strike, it is possible to use the measured strike distribution of the crater scarps to correct the circular distribution of any other class of scarp.

A 7.7° rotation is performed, to align the circular distribution with the EW axis, and a low-pass filtering is used to smooth the crater scarp circular distribution (Figure 3.8 black line). The difference between the obtained distribution and a uniform circular distribution is subtracted from the circular frequencies obtained for the tectonic features. Figure 3.9 shows the measured and corrected length weighted circular distributions for the NFs and WRs. As expected, the correction increases the relative weight of ~NS features, rectifying the circular bias due to the MOLA gaps. With the correction the mean azimuths are displaced toward the North-South axis and the circular variance values change (Table 3.6).

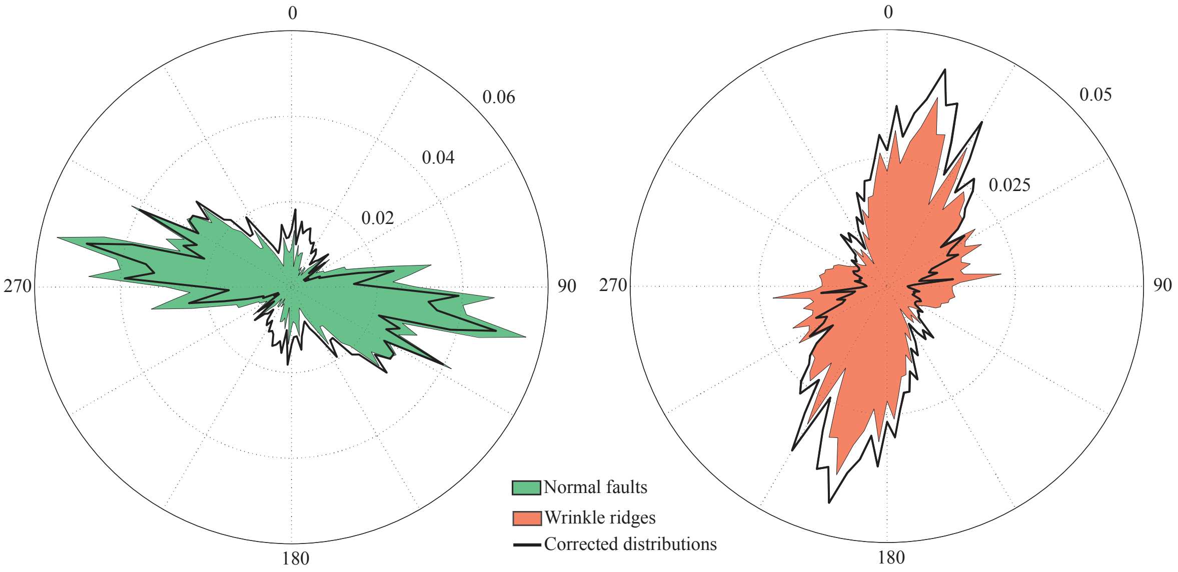

Figure 3.9 – Dataset III length weighted circular distributions (patches). Black lines represent the bias corrected distributions using Figure 3.8 circular distribution obtained from the crater scarps circular distribution. Note that the correction has the general effect of increasing the frequencies of North-South trending features, rectifying the expected circular bias due to the preferential orientation of MOLA data tracks.

Table 3.6 - Circular statistics for the corrected and uncorrected circular distribution of Figure 3.9. Mean azimuth ($\overline{\sigma}$), von Mises concentration parameter maximum-likelihood estimator ($\overline{k}$) and circular variance (V) are the depicted statistical parameters.

	NF			WR		
	$\overline{\sigma}$	$\overline{k}$	V	$\overline{\sigma}$	$\overline{k}$	V
Uncorrected	106,1	1,0	0,5	28,5	0,6	0,7
Corrected	116,3	0,6	0,7	16,7	0,9	0,6

Circular distributions of NFs and WRs are multimodal for all the datasets, which denotes a complex tectonic evolution of the Thaumasia Plateau province.

For NFs, three modes (0°, 100° and 130°) with similar maximum frequencies are recognizable in diagrams I and II of Figure 3.10. Those same trends are also recognizable in dataset III diagram, but presenting different relative strengths. A 50-60º minor local maximum is best seen in dataset III, despite it also being present in dataset II.

In dataset III, higher frequencies are associated with a 100° striking mode, being 130° and 0° modes characterized by lower frequencies. There are two alternative explanations for these lower frequencies in dataset III: the applied circular bias correction is not sufficient, and those azimuths are still underestimated, or this difference is real, and the semi-automatic procedure is recognizing a slightly different circular distribution for the NFs.

The circular distribution of WRs is much simpler. It is mainly composed by a large maximum centered at 15°. The main difference is the increasing circular variance from datasets I to III. Less evident minor modes striking 80-90° and 135° are also present in all the datasets.

A 5° interval is enough to include all the mean azimuth values computed for the WRs. A higher mean azimuth dispersion exists for the NFs case since computed values are comprised in a interval of ~12°, between dataset III (116.3°) and datasets I-II mean trends (128.5°-126.2°). The reason for the NFs higher differences can be related with the different strength ratios between the identified common modes.

The number of mapped lineaments increased from dataset I to III and the total length percentage of NFs and WRs varies between the datasets. Those variations can be attributed to the different spatial resolutions of the used datasets, as well as to with the different mapping criteria.

Despite the differences of used datasets and approaches, circular statistics of datasets I and II are surprisingly similar (Table 3.7). A 2° difference between mean azimuths for datasets I and II shows that a survey as that portrayed in dataset I is able to accurately represent the circular distribution of tectonic features at a regional scale. This suggests that for stress field recognition at a regional level, higher resolution mapping may be unnecessary since a regional mapping effort is able to identify the same circular trends.

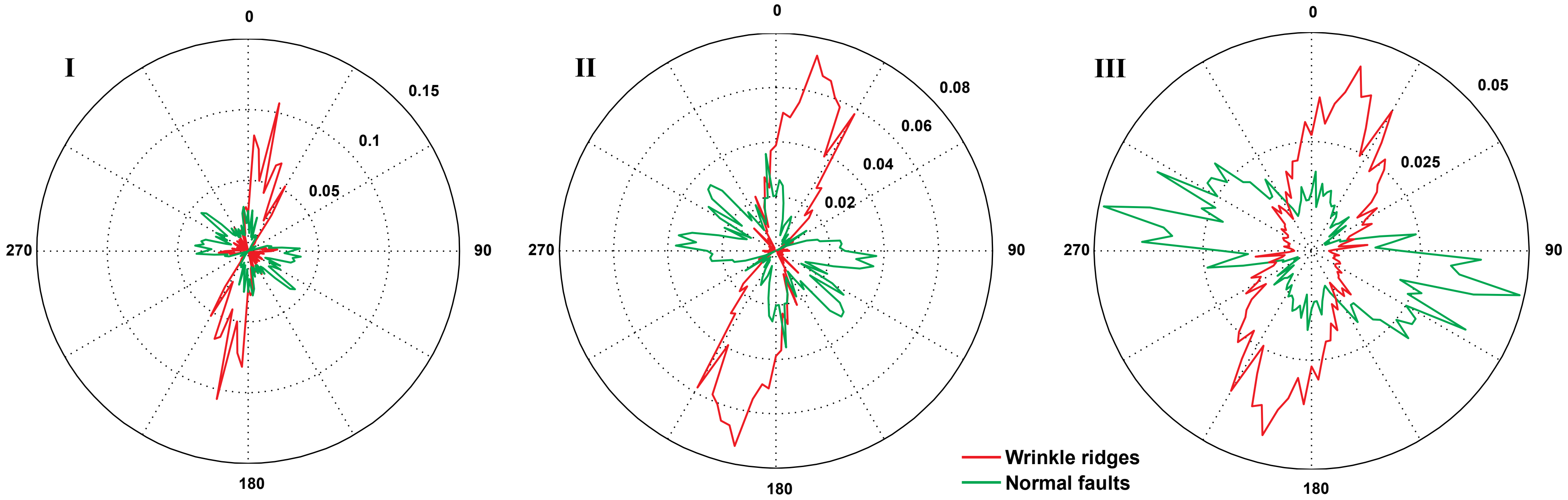

Figure 3.10 – Circular distributions for the WRs and NFs mapped in datasets I, II and III. Circular distributions presented for dataset III are those corrected for the directional bias (see Figure 3.9).

Table 3.7 - Circular statistics for the NFs and WRs of the three datasets. Dataset III mean azimuth ($\bar{\sigma}$), von Mises concentration parameter maximum-likelihood estimator ($\bar{k}$) and circular variance (*V*) are those correspondent to the corrected distribution (Table 3.6). Length percentage of the two classes (NFs and WRs) and the number of mapped lines are also shown.

		$\bar{\sigma}$	$\bar{k}$	V	Length %	N
I	NF	128,5	0,6	0,7	51,4	738
	WR	10,7	1,4	0,4	48,6	292
II	NF	126,2	0,5	0,8	60,5	1445
	WR	13,7	2,2	0,3	39,5	1230
III	NF	116,3	0,6	0,7	36,3	2044
	WR	16,7	0,9	0,6	63,7	4476

A higher disparity exists between the circular distribution of dataset III and the manually mapped lineament datasets. From a tectonic perspective, circular modes are directly linked to the stress fields. When the circular distributions are not unimodal (this should be expected in transtensive and transpressive regimes, as well as in areas affected by multiphase deformation with shifting stress fields), the identification of the modal trends is more important than the computation of the mean vector (since a mean azimuth may not be able to correctly identify the σ_1 orientation). The presented crater scarp correction should be regarded as a useful way to test the self-consistence of the automatically extracted lines. Since the circular distributions of I and II agreed well, it is also possible to use those distributions to generate a corrective distribution to be used in future mapping efforts (using the same procedure described for the crater scarp correction case).

All the modes are recognizable in the three datasets, making the semi-automatic procedure also capable of identifying the main stress trends. The ~5-12° angular interval between the mean azimuths of the manual and semi-automatic datasets can be considered a good result. In fact, 10° bins are commonly used to plot directional trends of Mars mapped tectonic features (Wilkins and Schultz, 2003; Bistacchia et al., 2004; Borraccini et al., 2007). The obtained mean azimuth dispersion is comparable with the bin sizes normally used, which is indicative that the semi-automatically derived circular statistics are within the acceptable ranges.

3.5 Conclusion

In terms of accuracy, a fair to moderate agreement is found to exist between the three datasets at the scales of analysis. Agreement rates are slightly lower for the cases where the semi-automatic dataset is evaluated. Despite that, the semi-automatic procedure allowed the identification of a higher number of structures not identified in the other mapping efforts. In areas with a good MOLA coverage, WR mapping is more accurate and complete since both bounding scarps as well as minor scarps are correctly retrieved from the altimetry data.

Line density is perhaps the parameter that presented a higher degree of variation between the datasets. Those variations are related with the spatial resolution of used datasets as well as with, in cases of manual mapped lineaments, the personal style of the interpreters.

Despite the regional and local approaches used to create datasets I and II, the circular statistical analysis shown that the regional approach is also capable of recovering the same overall circular distribution pattern. After directional bias correction, dataset III is also capable of representing the main trends. Directional statistical parameters extracted from the semi-automatic derived dataset are within the acceptable ranges.

This comparative work allowed to identify the main problems associated with the applied semi-automatic procedure. The main problems are related with specific MOLA DTMs limitations. Despite the high accuracy of the laser-derived altimetry, areas with bad data coverage lead to over segmentation of the mapped lines, as well as to the non-recognition of features in the more severe cases. The preferential trend of the MOLA data tracks produce a directional bias, with North-South striking scarps being preferentially underestimated. For regional surveys, that bias can be corrected using the circular distribution obtained for crater scarps. Smaller scale features can be completely overlooked due to the coarse resolution of the MOLA data.

Despite the pointed limitations, our results validate the semi-automatic procedure to map tectonic features at a regional scale using MOLA DTMs. Data fusion of MOLA and photoclinometry derived altimetry (Lin et al., 2010) would certainly improve the mapping results.

The lineament classification stage is the main obstacle to the fully automation of the lineament mapping process. Automatic recognition of the scarps allows to reduce subjectivity, putting the focus on the geological interpretation and not on the mapping itself.

Mapping tectonic features from remote sensing data is more than drawing lines. Discriminating skills are essential to characterize and interpret the mapped features on Mars surface. A fully automated procedure, that would map and classify the lineaments according to their tectonic meaning, would possibly leave behind essential information, such as cross-cutting relations, oblique shear senses or preservation grade of the mapped scarps. The adopted semi-automatic procedure, since it relies in the human classification of the lineaments using imagery, still allows this degree of freedom to the user.

The morphometric measurements associated with the classified scarps are an extension of the classic 2D analysis, constituting a promising tool for the tectonic analysis of topographic datasets. The presented comparison used MOLA data with the best spatial resolution achievable. In the future the same methodologies will be applied to higher quality elevation data from Mars and other planets.

4 New perspectives on the evolution of the East Thaumasia region

The several proposed tectonic models for the evolution of the Thaumasia plateau were previously referred in chapter 2.2. A detailed analysis will be performed for the eastern part of the Thaumasia region (Figure 4.1 and Figure 4.2), a region whose tectonic evolution deserved special attention on previous studies (Schultz and Tanaka, 1994; Dohm and Tanaka, 1999; Anguita *et al.*, 2006; Borraccini *et al.*, 2007; Montgomery *et al.*, 2009). All the mentioned studies always relied on a more or less detailed photogeologic interpretation of the tectonic structures. Dohm and Tanaka (1999) established the general geological evolution of the area and defined a stratigraphic sequence. Those stratigraphic units were later used by Borraccini *et al.* (2007) to analyze their mapped tectonic structures (dataset II used in chapter 3) affecting each stratigraphic unit. A detailed comparative analysis lead Anguita *et al.* (2006) to propose an orogenic belt characterized by thick- and thin-skinned tectonics. A more schematic and interpretative mapping was presented by Montgomery *et al.* (2009), who proposed that the Thaumasia Plateau structure resembles a "mega-slide" along a hypothesized salt related *décollement*. The existence of these large salt deposits is still very speculative, but the proposed model successfully characterizes a large part of the observed tectonic structures and kinematics. Focusing in the study region, the proposed kinematic behavior for the Thaumasia Minor "microplate" was partially confirmed by the strain analysis presented in chapter 2. Despite that fact, the style and timing of this deformation in the analyzed north Thaumasia Planum rift (the rift formed after the formation of the wrinkle ridges and with the inversion of the shear sense) indicates a more complex evolution.

The primary objective is not to support or deny any of the proposed physical models that drive the formation of the tectonic structures. The intention is essentially to characterize, as objectively as possible, the tectonic structures present on the surface. Strains will be estimated for the normal faults using the same methodology employed in section 2. A method for analyzing the compressive strains related with wrinkle ridge formation is presented and applied to the study area.

Tectonic structures will not be analyzed separately, as in the majority of the mentioned studies. The developed mapping procedure also allows a morphometric analysis of other kind of structures which contributed to the formation of the complex topography nowadays observable. The morphometric analysis of drainage paths as well as of other geomorphologic elements is integrated with the analysis of the mapped tectonic features.

A detailed mapping of the tectonic structures and drainage networks located east of Protva Valles, gives a new perspective and time constrain on the complex interplay between tectonic and hydrologic activity in the Thaumasia region.

In the end an evolutionary sketch is proposed which incorporates all the described observations.

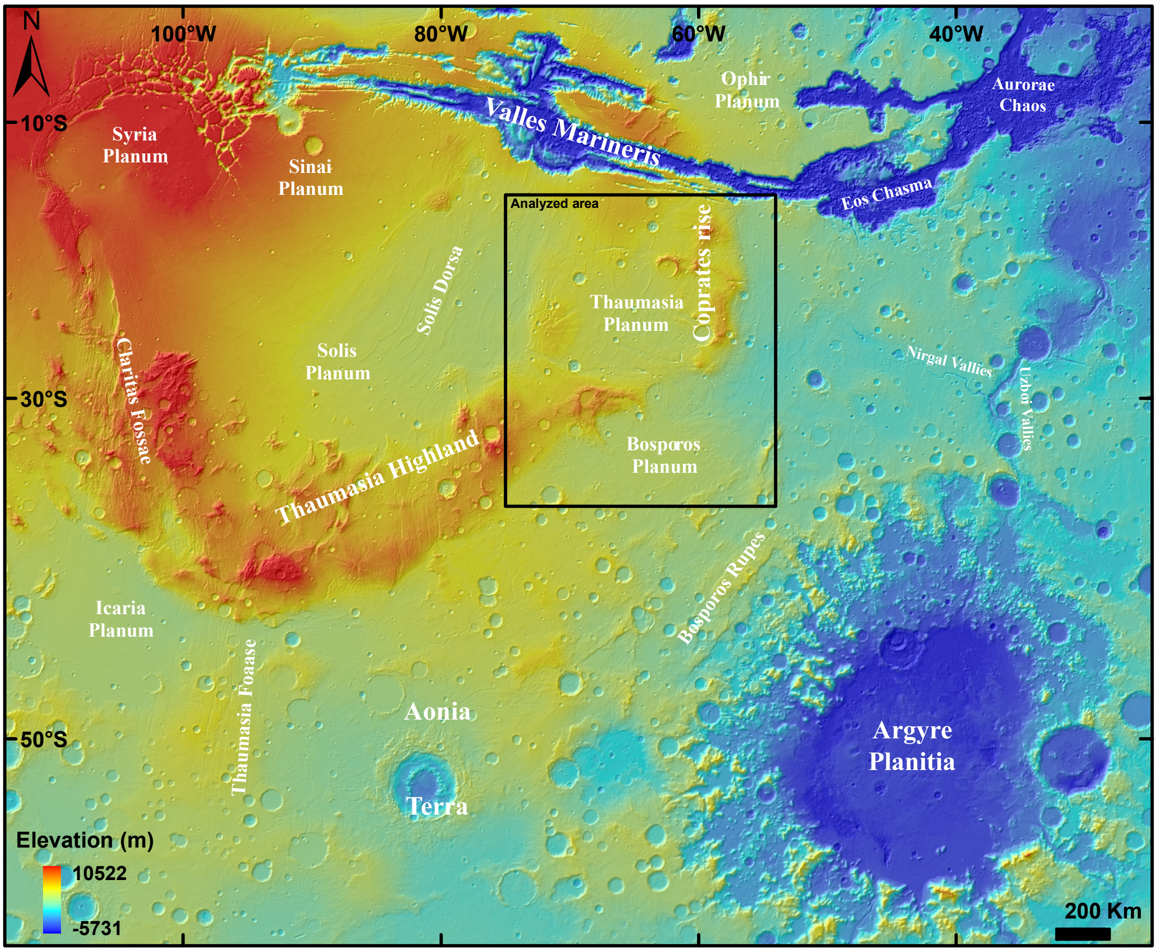

Figure 4.1– Context topographic map. Framed area corresponds to the study area. See Figure 4.2 for a more detailed view of the study area.

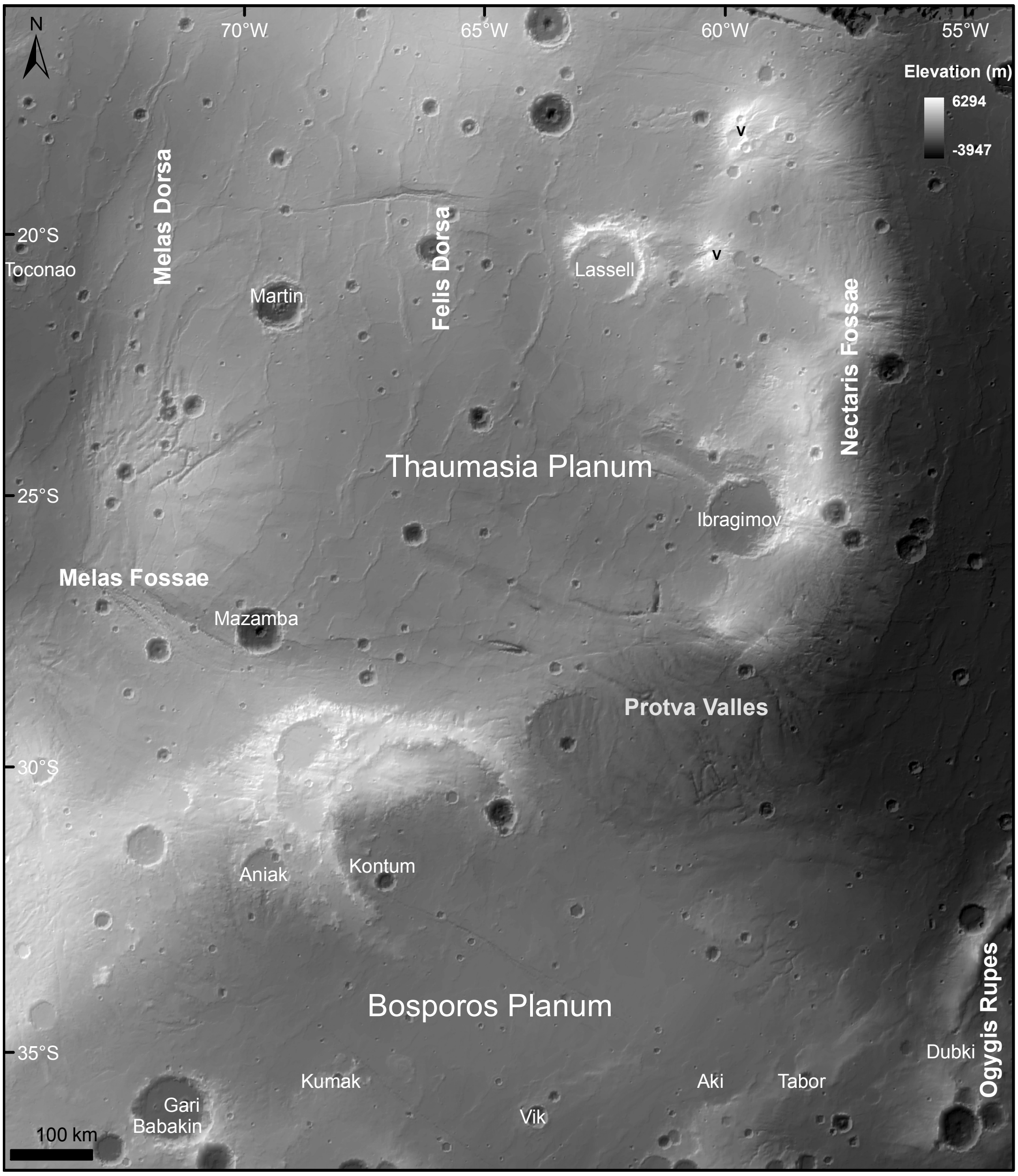

Figure 4.2 - Shaded relief topography of the Thaumasia Planum region. Two degraded volcanoes are marked with V.

4.1 Geology

Several geologic units were defined for the Thaumasia region by Dohm and Tanaka (1999) based on stratigraphic relations and morphologic characteristics, following the stratigraphic scheme of Tanaka (1986). The units were defined by the existing type of morphologies (note the morphological descriptive unit names in the legend of the geologic map in Figure 4.3). This implies that the mapped units could be considered more like morphologic units than pure geologic units, as those mapped on our planet. Geologic units that illustrate Earth geologic maps reflect and integrate essentially two different geologic aspects: lithologies and ages. Despite those differences, it is believed that the mapping methodologies used on Mars allow a first-order approximation to the mapping and characterization of geologic processes (Tanaka *et al.*, 2009).

The defined units were dated by crater counting (for a method review see Hartmann, 2005). High uncertainties may be associated with absolute ages derived from crater densities curves. Secondary craters as well as dependence of scale of analysis may strongly influence the obtained ages (see Carr, 2006, p. 36-42). Even so, it is a widely applied technique, and is the only possible dating method until radiometric ages became available.

The older terrains present in the study area are cratered, etched, dissected and fractured terrains of Noachian age (see map in Figure 4.3). Those units are concentrated along the North-South aligned highlands of Nectaris Fossae (Coprates Rise is also an informal name used for the area) and on the Northeast-Southwest trending highlands, located between Melas Fossae and Bosporos Planum. Two minor patches of Noachian terrains correspond to the fractured terrain of Melas Dorsa and to the subdued and dissected terrains near Ogygis Rupes (refer to Figure 4.2 for location). Unit *Nfu* correspond to two degraded volcanic edifices, of possible Noachian age (Dohm and Tanaka, 1999).

Hesperian age units embay older terrains and are though to be of volcano-sedimentary origin. They form the ridged plains, which in map view constitute the majority of the analyzed area. Three main units of Hesperian age are dominant: an older ridged plain unit that corresponds to the Thaumasia Planum and Felis Dorsa regions (*HNr*), a younger ridged unit (*Hr*) that appears east of Melas Dorsa and west of Nectaris Fossae and the third main unit, named smooth unit (*Hpl3*), is located in Bosporos Planum (Dohm and Tanaka, 1999; Dohm *et al.*, 2001a). Amazonian units are only represented by a small area in the Valles Marineris escarpment.

The general arrangement of the geological units, topography and ages suggest a large anticlinal structure with axis trending N-S along the Coprates rise and passing to a NE-SW trend north of Bosporos Planum. Other high amplitude structures, previously interpreted by Schultz and Tanaka (1994) as lithospheric-scale buckles correspond to the N-S trending highs of Melas Dorsa and Felis Dorsa. The NE-SW lobated scarps located near Ogygis Rupes were also interpreted as large scale thrust faults.

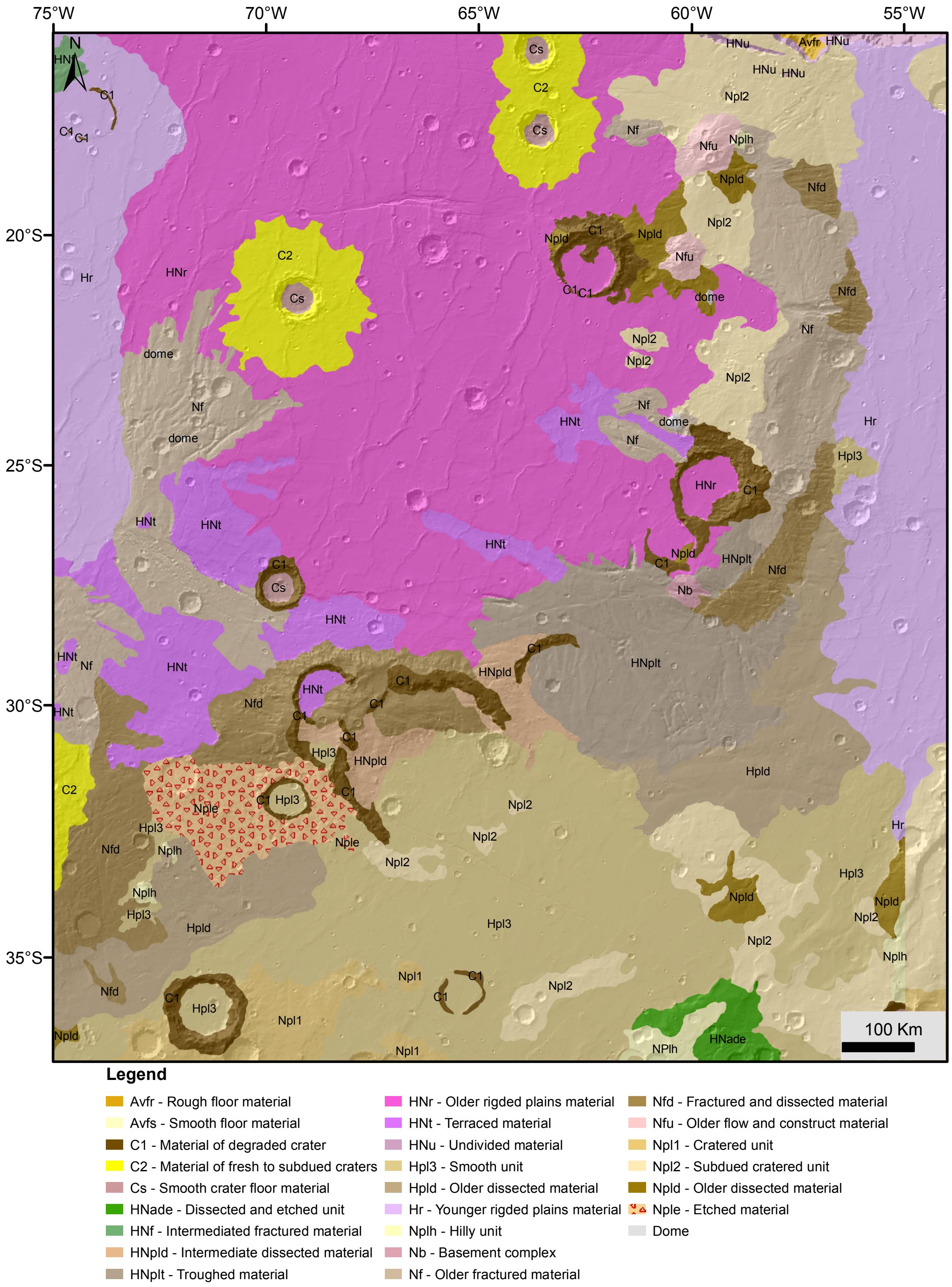

Figure 4.3 –Dohm *et al.* (2001b) geologic map of the Thaumasia region. The shown units for longitudes east of the 55ºW meridian were adapted from the digital version of the Global Geologic Atlas of Mars (Skinner *et al.*, 2006).

4.2 Tectonic characterization

The quantitative and qualitative evaluation of the semi-automatically mapped tectonic lineaments, presented in chapter 3, supports the following analysis and discussion. The advantages given by the integrated morphometric analysis are explored in order to give a new insight on the tectonic evolution of the East Thaumasia region.

The map in Figure 4.4 shows all the mapped tectonic and tectonic related structures. Wrinkle ridges are the more abundant structures followed by several sets of normal faults that can form isolated grabens or even rifts. Other two types of structures associated with tectonic activity were mapped. Smooth wrinkles appear sometimes associated with wrinkle ridges. They lack the characteristic small scale crenulations on top of the ridges, and are interpreted to correspond to secondary higher amplitude folds. Those are not always easily identifiable on imagery due to the high amplitude and inexistence of a clear surface morphology. In association, or aligned with normal faults several linear depressions were identified. Two clusters are visible: one in the fractured terrain, north of Protva Valles, which may be related with hydrothermal activity (Dohm *et al.*, 2001c), and another set located near Coprates Chasma forming typical pit-crater chains morphologies (Wyrick *et al.*, 2010).

Normal faults are commonly found in the Noachian elevated terrains while wrinkle ridges are widespread in the lower flatter plains. Generally, wrinkle ridges do not present clear signs of erosion, while many of the mapped normal faults scarps present signs of erosion and sedimentation on the grabens floors. In the East facing margin of the Coprates Rise, deeply incised graben-like depressions exist. Since they best reflect an erosional past, they were not classified as normal faults. Nevertheless their linear trends, strongly suggests a preferential erosion controlled by fractures.

Besides that first order classification, a second type of characterization was performed during the lineament classification stage. The presence of signs of scarp degradation was registered as well as the inferred horizontal shear sense associated with the mapped tectonic features. For the normal faults case, features were classified as dextral or sinistral according to one main criterion, the arrangement of the faults in *en echelon* arrays. Note that those *en echelon* patterns are easier to recognize when the arrays are relatively small (as those described in chapter 2). As will be shown, there are also cases where fault sets are composed of long linear fault segments, whose *en* *echelon* pattern arises only at larger scales. In these cases it is hard to infer an oblique displacement component associated with the individual normal faults segments.

An oblique compressive regime is much easily recognizable from imagery. As mentioned, small scale crenulations and folds are present in some of the wrinkle ridges. Those structures may be arranged *en echelon* giving the sense of horizontal shear (see the well ilustrated examples in Smart *et al.*, 2006). In other cases curved shaped wrinkle ridges may even displace and deform older structures, and S or Z shaped tear faults may form. A horizontal shear component is not definable in most cases, and those structures are treated as being purely compressive or purely distensive.

The lineament maps in Figure 4.5 show the inferred shear sense for compressive and distensive tectonic structures. The statistics of the circular distributions of Figure 4.5 are presented in Table 4.1. The number of mapped scarps that represent wrinkle ridges is the double of the number of normal faults scarps. Approximately 90% of the total length of mapped lineaments corresponds to pure compressive or pure distensive tectonic structures. This indicates that oblique structures are rare or, alternatively, that they were underestimated.

A conservative approach was followed during the classification stage, so that a horizontal shear sense was only assigned when indicative morphologies were observable from high resolution imagery. Erosive processes may have also played an important role in masking the small scale morphologies indicative of the presence of an oblique strain component. Other important aspect is the scale and partition of the deformation. Oblique strains may be partitioned not homogeneously. In some places strains may be concentrated in a small area, producing morphologies large enough to be recognizable from orbital imagery. In other places strains may be widespread over larger areas, producing a different set of morphologies, where the strains are spread along smaller scale structures, not easily recognizable in the images. A fact is that oblique structures were probably underestimated, but is not expected that they represent the majority of the mapped structures.

The characterization of the sense of horizontal shear associated with possible oblique tectonic structures has never been performed systematically on Mars. The implications and the way to deal with this new degree of complexity will be discussed further along.

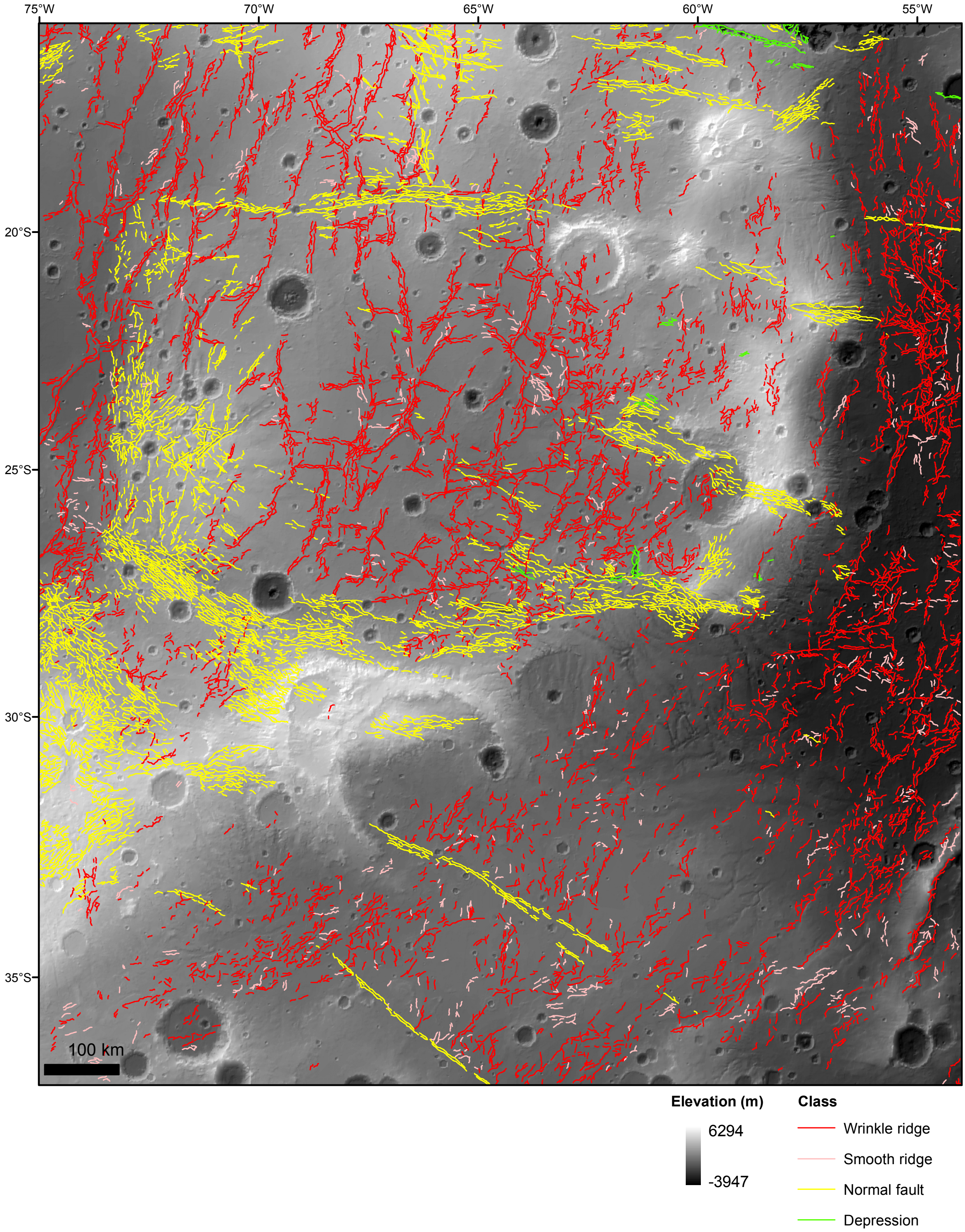

Figure 4.4 - Mapped tectonic features. Wrinkle ridges and normal fault scarps are the more abundant features. Linear depressions were also identified and are usually associated with extensional faulting. Smooth ridges correspond to compressive structures similar to wrinkle ridges but lacking the characteristic rugged ridge of wrinkle ridges. They appear usually in association with wrinkle ridges. See Annex 1 to get a better view of all the mapped features. Annex 2 shows an oblique perspective of the same area.

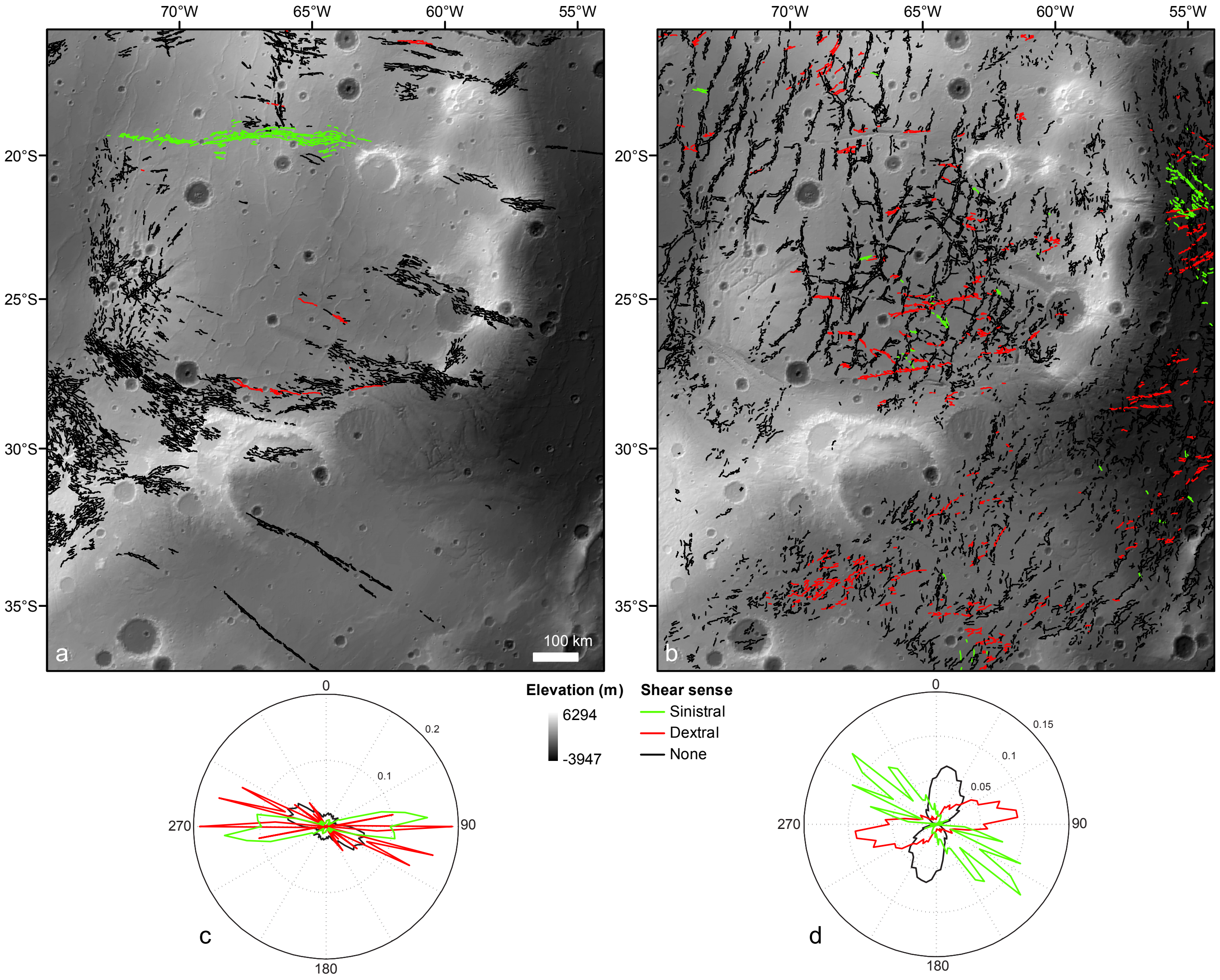

Figure 4.5 - Spatial distribution of the mapped structures according to the inferred shear sense; a) normal faults; b) wrinkle ridges; c) and d) are the correspondent corrected length weighted circular distributions.

Table 4.1 - Length weighted circular statistics for the normal faults and wrinkle ridges in Figure 4.5 according to the inferred horizontal shear sense.

	Normal Faults					Winkle Ridges				
	$\overline{\sigma}$	$\overline{k}$	V	Length %	N	$\overline{\sigma}$	$\overline{k}$	V	Length %	N
Sinistral	86.8±1.2	1.91	0.32	6.4	203	130.6±1.4	1.67	0.36	1.9	173
Dextral	104.8±2.1	1.75	0.35	1.5	46	74.4±0.8	1.31	0.45	10.3	865
Pure	117.2±0.6	0.67	0.68	92	3776	16±0.3	1.23	0.48	87.8	8282

Global directional statistics are shown in Table 4.1 for each type of tectonic structure and class of horizontal shear associated. The presented parameters were computed after the correction of the length-weighted circular distribution. The applied correction was the same introduced in section 3.4.4 and aims to correct the directional bias produced by the preferential orientation of the MOLA tracks.

4.2.1 Distensive structures

Bimodality characterizes the circular distribution of the pure normal faults. A principal mode trending ~N120ºE and a secondary mode comprised between N0-30ºE are the key features. Note that those modes correspond to perpendicular sets of normal faults and will be analyzed separately in the following sections.

Left-lateral normal faults are well represented and correspond to the structures that form the East-West rift previously analyzed in chapter 2. A mean trend of ~87º was computed for this set of features while a ~105º mean trend was obtained for the normal faults that present evidences of possible right-lateral displacement. This last set is less represented, but seems to be concentrated in the rift located between Melas Fossae and Protva Valles, in the Coprates Rise South termination. This right-lateral strike-slip component has previously been recognized by Borraccini *et al.* (2007) who interpret this rift as a transfer fault system related with the differential movement of the Thaumasia Plateau block. Only a small number of oblique structures in this area have been recognized. This attests the difficulty in finding clear indicators of horizontal shear for each normal fault, this possible oblique component being much easier to infer from the arrangement of large scale structures, in the case of the entire rift system.

4.2.1.1 Lineament topographic height index - *THI*

Traditional 2D lineament analysis employs length weighted circular plots and statistics to characterize the trends of a lineament population. The spatial distribution of the length of the lineaments is commonly not a motive of interest, perhaps because the length of each individual segment depends on the interpreter, as seen in the comparison of the two human produced lineaments datasets (see lineament length density plots in section 3.4.3). In the case of the automatically mapped lineaments, MOLA gaps break the continuity of the mapped structures, which may also influence the spatial distribution of the length of the mapped line segments.

A new index based in scarps morphometric attributes is introduced: it allows a weighing of the mapped lineaments that produces similar results to the traditional length weighing, allowing at the same time to evaluate the spatial location of the more relevant structures. The proposed index is named topographic height index (*THI*) since it combines the mean height of the scarps h (computed as described in chapter 2) with the mean pseudo-frequency f, obtained from the wavelet edge analysis (see section 2.4.1.2). The index is computed for each scarp according to:

$$THI = \log\left(\frac{f}{h}\right). \qquad \text{(Eq. 4.1)}$$

The logarithm is used to compress the range of obtained values. From a signal processing perspective, the computed parameter corresponds to the approximate ratio between the frequency and the amplitude of the signal in the vicinities of the scarps.

Note that h varies much more from scarp to scarp than f. This makes that the major part of the *THI* variance observable in Figure 4.6b comes from the height of the scarps. In other words the *THI* variations better represent the height variations of the scarps.

Scaling functions between the length and throw of normal faults have been studied (Schultz *et al.*, 2004; Xu *et al.*, 2006) revealing that maximum normal fault throw generally increase with fault length. This imply that length and *THI* should be inversely proportional, which suggests that the circular distributions may differ depending on the parameter used to weight the strike vectors. Despite this, computed length and *THI* weighted circular distributions present similar characteristics (compare the rose diagrams in Figure 4.7a and Figure 4.7b). It is not clear why this happens, and further quantitative testing, using perhaps synthesized fault scarps should be performed in the future.

The lineament length spatial distribution is somewhat fuzzy (Figure 4.6a). Even so, clusters of longer lineaments are visible, but those clusters are always disturbed by the presence of smaller lineaments. The *THI* spatial distribution (Figure 4.6b) displays a more comprehensive arrangement of the normal faults because the *THI* values allow the ranking of the scarps by reflecting their different heights.

Several clusters presenting lower *THI* values are visible (lower *THI* values correspond to lower frequencies and/or higher scarp heights). Zone I, highlighted in Figure 4.6b, shows an area of lineaments with low *THI* values. Those normal faults present a lateral variation from NW to SE, where the faults cross the dissected rim of a Noachian crater. The zone where the *THI* values decrease corresponds to this rim, which indicates that the faults scarps where dissected, nowadays presenting anomalously high apparent vertical offsets due to erosive processes.

Zone II shows a different case. A set of grabens crosses the Coprates rise, fracturing a dissected crater whose floor has been filled with Hesperian rigged plains materials. The faults continue eastward until they disappear bellow the rigged plains. The faults located inside the crater present higher *THI* values. This suggests two separated phases of tectonic activity. During the first phase, the development of the main faults, which are nowadays best represented in higher terrains outside the crater, took place. Those fault scarps were probably subjected to erosion, which justifies their lower *THI* values. After the emplacement of the plain materials inside the crater, a less intense tectonic phase reactivated the previously formed normal faults, creating smaller faults on the Hesperian crater floor covering unit. As will be seen, this dual tectonic regime will be recognized in other scenarios and regions.

Zone III correspond to the central part of the rift analyzed in chapter 2. As reported before, the central part of the rift has the higher extension rates, which correspond to the area with lower *THI* values located in this zone. No signs of scarps erosion were found in high resolution imagery.

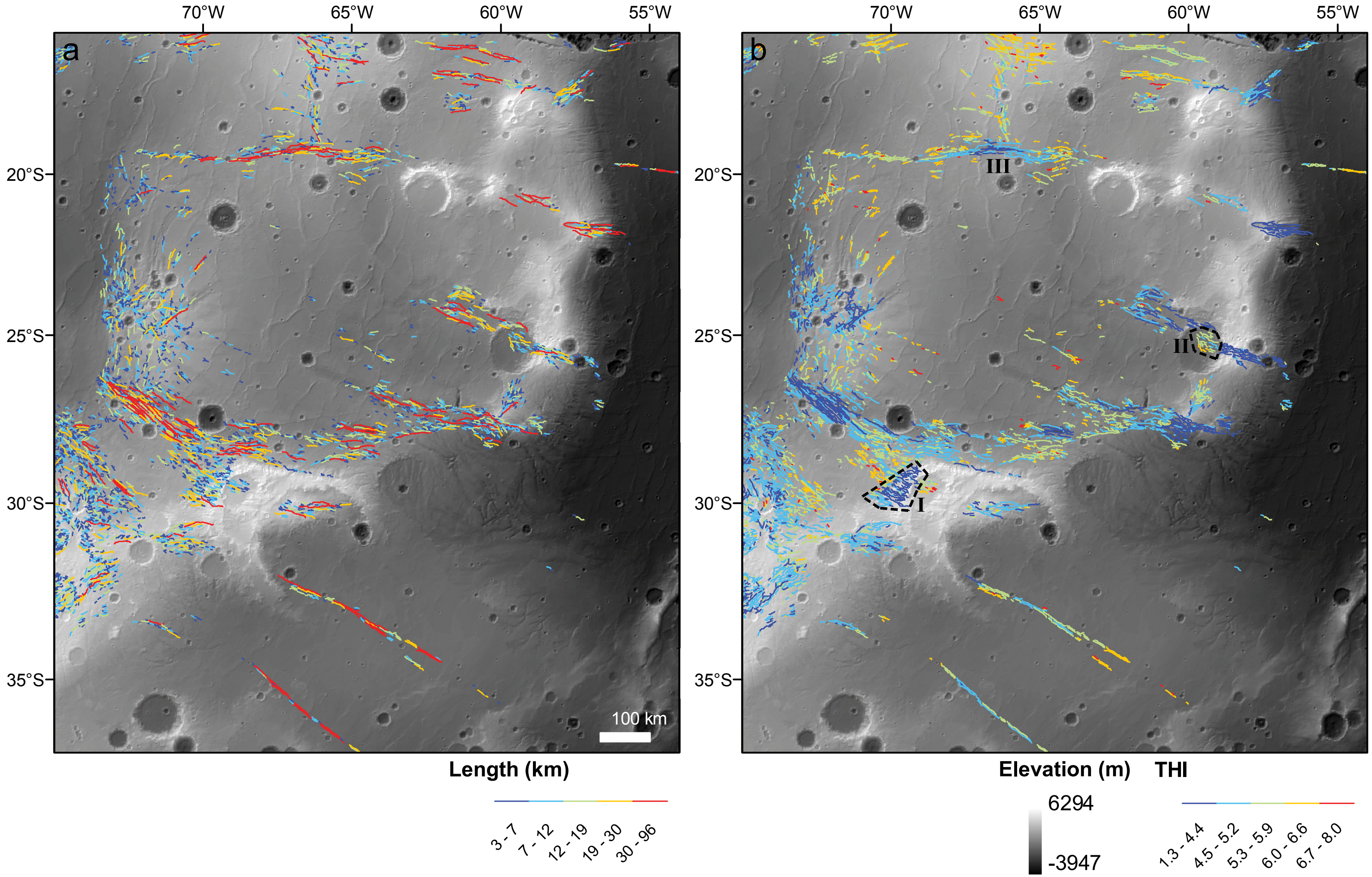

Figure 4.6 - See next page for full legend.

Figure 4.6 –Map a) and b) present the normal fault length and *THI* spatial distributions. Note the general agreement between the circular distributions and the spatial distributions (an inverse relation in this case) of the length and *THI* weighted features. Map (b) present a more consistent spatial segmentation of the mapped normal faults, with a better spatial clustering of the normal faults scarps. See text for discussion and Figure 4.7 for related circular distributions.

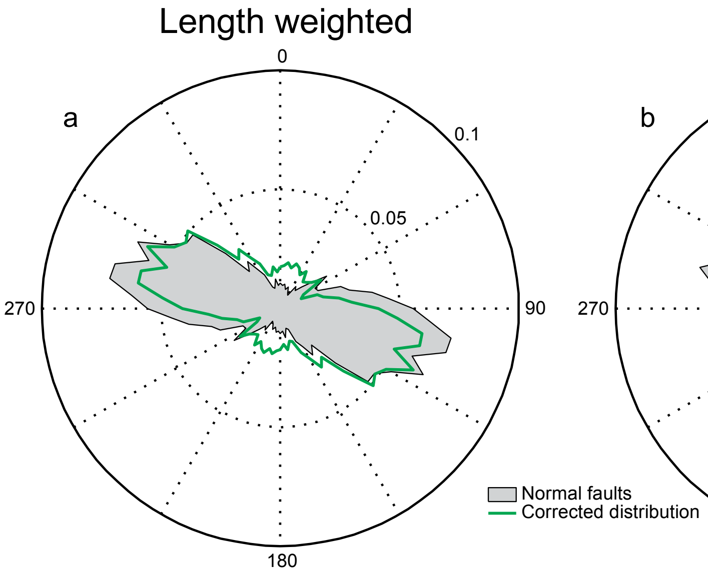

Figure 4.7 - Normal faults circular distributions. Rose diagram a) present the length weighted circular distribution and b) presents the *THI* weighted circular distribution. Green line distributions correspond to the directional bias corrected distributions (see section 3.4.4).

4.2.1.2 The N0-30ºE normal faults

The bimodality of the lineament population, with two orthogonal sets of normal faults has been earlier linked with two distinct deformation episodes. Since the N0-30ºE normal faults are mainly located in the Noachian unit *Nf* that form the ~N-S axis of the Melas Dorsa those tectonic structures were interpreted as Noachian in age (Borraccini *et al.*, 2007). Cross-cutting relationships also support that those structures are older than the N120ºE striking set of faults, namely those that form Melas Fossae.

Borraccini *et al.* (2007) invoke an early tectonic episode (Middle Noachian) linked with an E-W regional extensional stress field that formed the older ~N-S normal faults. A secondary cluster of faults with the same trends exists located again on top of a more elevated region, north of Felis Dorsa. In this case Hesperian age plains materials (unit *HNr*) are deformed.

Several long wavelength buckles were mapped by Schultz and Tanaka (1994) in the Thaumasia area. In the study area, besides the Coprates rise, two other N-S trending structures were identified: Melas Dorsa and Felis Dorsa. Those structures were interpreted as lithospheric-scale bends spaced hundreds of kilometers apart. The same interpretation was made by Borraccini *et al.* (2007), dating the formation of this large buckles as Early Hesperian.

The close spatial relation between these sets of normal faults and the axis of the large scale buckles (Melas and Felis Dorsae), is not ignored in this work, and a different genetic mechanism that relates those different structures is proposed.

The referred spatial association of the sets of normal faults with the axis of the large scale bends may reflect a genetic relation between these different structures. There is an apparent incongruence between the stress field needed to justify the formation of the normal faults and of the large scale buckles. The first ones imply a vertical σ_1, and a σ_2 striking ~N-S while the large scale compressive structures reflect an ~E-W horizontal σ_1. This last σ_1 is compatible with the same principal stress responsible for the formation of the wrinkle ridges during the Hesperian, and can be related with the same physical mechanism: the possible gravity-driven slide of the Thaumasia block. This has been earlier recognized by Schultz and Tanaka (1994). In their model, the compressive structures developed at two scales (wrinkle ridges spaced by tens of kilometers and large buckles spaced hundreds of kilometers), and were basically formed due to a same stress field acting in a two-layered decoupled lithosphere.

Is it really necessary to invoke an early phase of ~EW extension, or can the referred normal faults development be correlated with the same stress field responsible for the formation of the long wavelength buckles and wrinkle ridges?

A tectonic inversion would be reasonably expected if the formed faults were later affected by a regional compressive stress, the same responsible for the formation of the Dorsae. Signs of this inversion were never reported. Furthermore, the spatial association of the N0-30ºE normal faults with the large scale lithospheric buckles suggests that they may have formed coevally.

Syn-kinematic normal faults may form parallel and along the axis of anticlines (Strayer *et al.*, 2004; Morley, 2009). Perhaps the most spectacular case of anticline crestal extensional faulting is the one described by Morley (2009). In the referred work, crestal normal faults appear associated with deepwater folds, formed with syn-kinematic sedimentation. The development of longitudinal extensive structures parallel to fold axis requires a rotation of the σ_1, so that it passes from a horizontal to a vertical position near the fold axis. The most probable mechanisms involved in this process are: bending stresses that produce extension in the outer arc of the buckle and/or gravity induced stresses related with the vertical growing of the buckle.

The majority of the examples described by Morley (2009) point to gravity as the primary driving mechanism. High saturated and poorly consolidated sediments make the developing folds, in the mentioned case, highly sensitive to mass wasting processes. As will be seen in section 4.3.2, the Melas Dorsa flanks also display evidences of water-induced mass wasting processes, in the form of sapping valleys.

Map view patterns of the normal faults in Melas and Felis Dorsae also present similarities with some of the structures mapped by Morley (2009). But first, the large wavelength folds geometry of the Dorsae must be better described:

- Melas Dorsa is not a symmetric buldge; it presents a steeper East flank while the West flank dips gentler, which means that the axial plane of the anticline verges eastward;
- in the south the entire structure is cut by Melas Fossae faults, while in the north the height of the bulge decreases and it disappears below the ridged plains materials. This suggests a North plunging anticline;
- the North Melas Dorsa and the South Felis Dorsa zones seem to curve in opposite senses, forming *en echelon* folds terminations; in chapter 2 an E-W right-lateral transfer zone has been identified due to wrinkle ridge offset (see Figure 2.9). As discussed in that section, this rigth-lateral kinematics is probably inherited, which proves an early interaction between the two mega fold structures;
- Felis Dorsa is more symmetric, faulting is less intense and the axial surface apparently plunges Southward;
- normal faults in the Dorsae tend to form simple grabens.

Among the several fault patterns described by Morley (2009) one is particularly interesting: the one that illustrates a normal faults pattern developed on the hinge of two *en echelon* folds terminations. As the two folds propagate laterally, the *en echelon* plunging terminations of the folds start to form. During this stage a second set of normal faults may form oblique to the two folds and to the normal faults first developed. This same pattern is well visible in the eastern flank of Melas Dorsa, with a set of curved faults trending ~N30ºE, in the direction of the termination of the Felis Dorsa buckle. A third set of faults may develop in the plunging terminations of the folds. Those faults are orthogonal to the anticline (striking E-W) and are less represented in the same area of Melas Dorsa. Note that those faults are in the alignment of the North Thaumasia Planum rift, and must have been reactivated by the later sinistral shear event.

It is now possible to better interpret the normal faults directional secondary mode (located in the interval N0-30ºE). Approximately North trending fractures formed in the crests of two large scale Dorsae. In the curved interacting termination zones of the two folds, a second set of faults developed trending ~N30ºE. The trend interval corresponds to the sum of these two sets. A less represented set of faults formed in the terminal North edge of the Melas Dorsa strikes ~E-W.

The analogies between the observed patterns of deformation in this portion of the Thaumasia plateau, and some of the ocean floor compressive structures described by Morley (2009) are strong arguments that support the proposed interpretation. However, the physical mechanism responsible for the crestal distension may be different. Gravity-driven faulting as been favored for explaining the majority of the normal faults analyzed by Morley (2009). Those faults tend to form arrays that dip with the same direction of the dip of the fold flanks, forming stair-steps arrays of faults. In Thaumasia simple grabens predominate. This implies an extension mechanism not fully gravity-related, but primarily related with the fold outer arc extension associated with tangential longitudinal strains (Bobillo-Ares *et al.*, 2000). This is a well known process that creates extension in the outer arc of folds (in the case, in the top of the antiforms) and compression in the inner arc due to a horizontal shortening of the layered sequences. In this scenario, faults should not present preferential dip directions (depending on the fold flank where they are located), forming instead conjugated normal faults grabens (Strayer *et al.*, 2004).

The Dorsae were treated until know as simple buckle structures. However, the flank asymmetry that characterizes Melas Dorsa strongly suggests a fault-fold structure, with a blind thrust dipping eastward. This does not change the interpretation of the N0-30ºE normal faults as fold hinge extensional structures. The same kind of structures are expected to form during the emplacement of fold-thrust belts in association with a thrust ramp (Lemiszki *et al.*, 1994; Strayer *et al.*, 2004).

The different morphology of the Dorsae suggests a differential compressive behavior. The different ages of the terrains that form the bends axis (Noachian in Melas Dorsa and Late Noachian to Early Hesperian in Felis Dorsa) may also suggest a different formation age. Melas Dorsa seems to accommodate higher strains, while Felis Dorsa morphology suggests lower compressive strains. These observations support an eastward migration of the deformation, with the development of Melas Dorsa being followed by the emplacement of the older ridged plains materials and later formation of Felis Dorsa. All these evolutive steps were always driven by the same stress field. This situation also implies that, at least partially, the emplacement of the older ridged plain terrains (*HNr* unit) may be syn-kinematic with the formation of Melas Dorsa.

If the proposed interpretation is correct, this is one more case of the recognition of one pattern of tectonic structures at a wide range of scales. As an example, consider the recognition of shear zones at several magnitudes, from microscopic to regional scales (Tchalenko, 1970). In the presented case, similar patterns were recognized in outcrop folds (Lemiszki *et al.*, 1994; Bobillo-Ares *et al.*, 2000), in kilometric structures (Smart *et al.*, 2006 described an example of outer arc extension in a Solis Planum wrinkle ridge), in folds spaced tens of kilometers (Morley, 2009) and now in very large Martian lithospheric bends spaced almost 300 km.

The proposed model integrates the complex array of normal faults in this area, relating it with the formation of the Dorsae. It successfully combines a variety of tectonic structures under a unique, and possibly long lasting, regional stress field.

4.2.1.3 The ~N120ºE normal faults

The best represented family of distensive structures in the study area trends approximately N120ºE. To be more precise, fractures are comprised in the interval N105-135ºE. A dextral component of shear has been identified in some of those structures (see Figure 4.5), especially in the Melas Fossae region where they form *en echelon* arrays.

In the Coprates Rise they form several rift systems that traverse the entire structure. As pointed before, in this area those sets of fractures present degraded scarps, and they show signs of at least two phases of activity (recall the Figure 4.6b area II analysis above). The same general conclusion can be drawn for the rift system that starts in Melas Fossae and ends east of Protva Valles.

In the highlands between Melas Fossae and Bosporos Planum (in the Southeast corner of the study area), a complex interplay exists between the N120ºE faults coming from the Melas Fossae region, and other sets of normal faults trending NE-SW to E-W, again, parallel to the crest of a large scale antiform (this one making part of the Thaumasia Highlands ridge, see Figure 4.1). Many faults in this zone present signs of heavy erosion. The majority of the distensive activity in this region occurred before the emplacement of the unit *Hpl3* in the Bosporos Planum region, since only two sets of smaller long grabens occur on it.

It is clear that those structures segment and have conditioned the development of the Coprates Rise in the East and of the Thaumasia Highlands Southwest. They acted as transfer faults in a transtensional regime, being responsible for the longitudinal segmentation of the Thaumasia Highlands/Coprates Rise arch. This kinematic interpretation was correctly defined by Borraccini *et al.* (2007), but again, they favored a two phase model. According to that model, a Middle to Late Noachian regional extensional stress field, was responsible for the development of the N120ºE rifts as pure extensional structures. This phase was followed by an Early Hesperian compression with the principal compressive axis trending ~N120ºE. During this phase the allegedly earlier formed rifts where reactivated as transfer fractures during the folding and possible thrusting associated with the formation of the Coprates Rise and Thaumasia Highland buckles.

Note that a unique regional σ_1 striking ~N120ºE is enough to justify the formation of the two sets of structures, the distensive/transtensive rifts as well as the large scale buckles. This fact enables two possible models for the formation of the rifts: pure extension followed by transtension as argued by Borraccini *et al.* (2007), or only transtension, with perhaps non-uniform strain partition.

Discerning between the two presented possibilities is not an easy task. The described stratigraphic relationships suggest that more than one tectonic phase is responsible for the formation of the rifts: one intense phase before the emplacement of the *HNr* unit, and a less intense phase after the emplacement. Besides the clear intensity differences between those phases, a distinct pattern of faults do not seem to have formed. The second phase seems to be limited to the reactivation of the earlier features since a different faulting style is not evident. A unique long lasting transtensional episode is perhaps a simpler explanation.

4.2.1.4 Regional extensive strain analysis

The local strain analysis performed in section 2.5.2 showed to be an interesting methodology to evaluate the distribution of the strains along rift systems. The same methodology is used here to generate strain vectorial fields that enable a more regional assessment of the extensive strains affecting the eastern border of the Thaumasia Plateau.

As pointed, the simple adopted fault model assumes pure orthogonal extensional, constant dip angle of 60º; erosive or depositional processes are completely overlooked, which can strongly influence the obtained strain values.

The computed extension vectors for each scarp pixel were sampled using a 4 km/pixel grid. This results in an axial vectorial field which avoids the display of a large number of extension vectors.

Figure 4.8a shows the obtained axial extensional vectorial field for the entire set of mapped normal faults, using a pure orthogonal extensional model for all the faults. As discussed, there are evidences that at least some of the faults may also accommodate some oblique component of strain. A coarse way to approximate this scenario is to rotate the computed extension vectors in order to account for an oblique strain component. It is highly unlikely that a same obliquity angle would fit the real strain vectors of a complex case as the one being analyzed. Even so, Figure 4.8b displays the axial vectors computed according to the inferred shear sense associated with each normal fault (see Figure 4.5a). In this case, extension was only computed for fault scarps not presenting clear signs of erosion/deposition. Faults without a defined shear sense were treated as orthogonal.

Extension of sinistral and dextral normal faults was modeled by local rotation of the vectors anticlockwise or clockwise respectively. According with Taylor *et al.* (1994) oblique rifting in our planet tends to develop with obliquities in the range 15-45º. This is the reason why a constant rotation of 30º was used. A compelling example of a rift with

30º regional obliquity may be encountered in the Reykjanes Peninsula, Iceland (Taylor *et al.*, 1994; Clifton and Schlische, 2003; Fournier and Petit, 2007).

The model in Figure 4.8a presents higher strains in the Coprates rise region. As was mentioned earlier, the faults in that area are not pristine structures since they present signs of erosion. Those higher strains are for this reason overestimated. A mean extension trend of N13ºE was found for this model.

Compare the trends of the extensions on the North Thaumasia rift, interpreted before as a left-lateral transfer structure between two blocks. The second model better reflects this oblique extensive behavior. This is also discernible in the rose diagram of Figure 4.8b, with a secondary trend of extension striking N30ºW.

A minor extension trending E-W is also observable, and corresponds to the faults associated with the Dorsae. But perhaps the main difference between the two modelled strain fields is the higher relevance of the extension trending ~N30ºE, that together with the N-S vectors constitute the two main extensional trends. Those trends suggest conjugated extensional faulting. In this case, the mean extension vector trends N19ºE (Table 4.2).

In absolute terms, and excluding extension vectors in eroded areas, the two areas that were subjected to higher extension were the North Thaumasia Planum rift (in its central region, as shown before) and Melas Fossae, especially in the region situated East of the Mazamba crater. The analysis of the strains associated with this second area will be addressed in more detail in the following section.

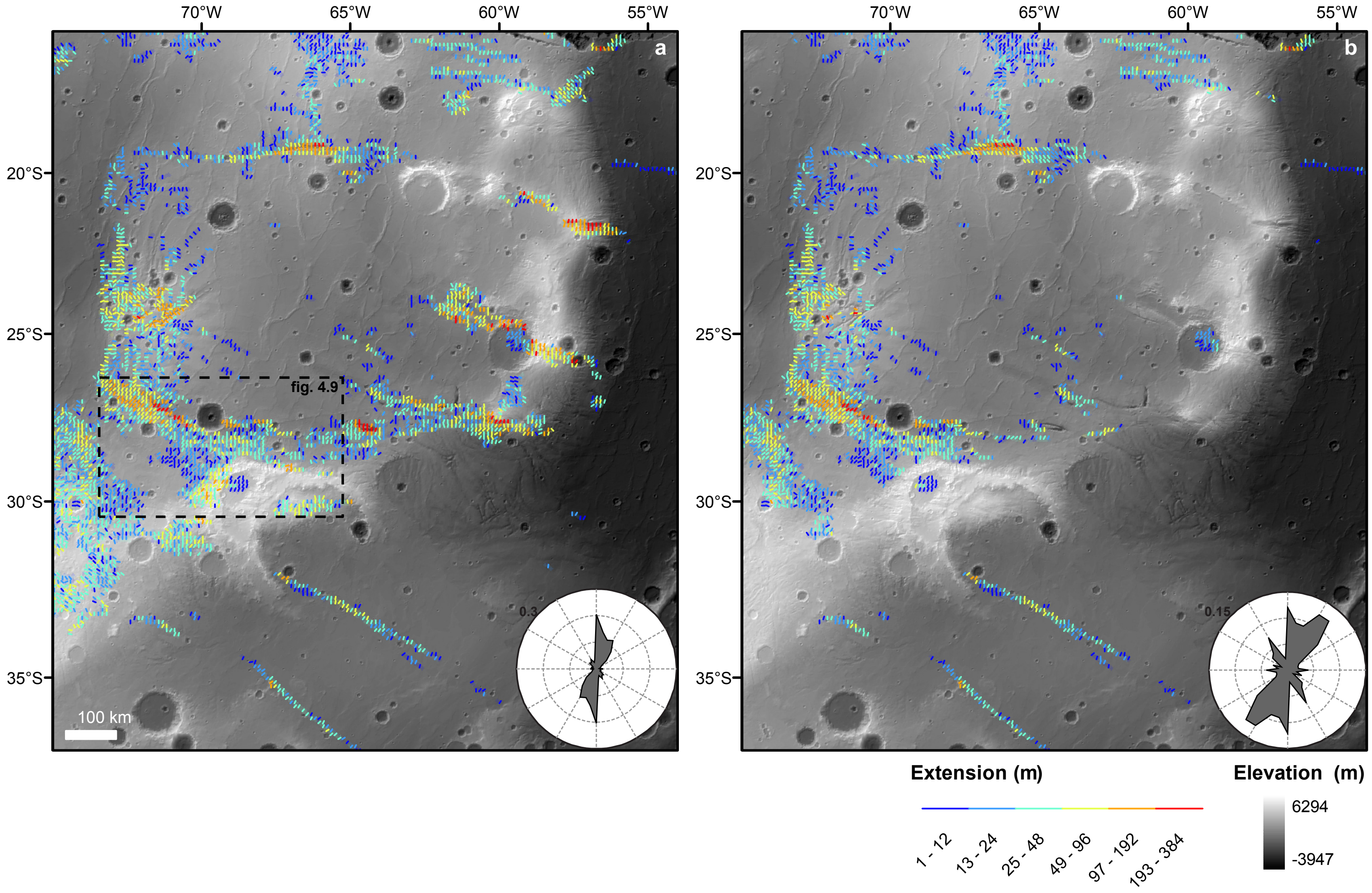

Figure 4.8- See next page for full legend.

Figure 4.8 - Extension vectors; (a) vectors computed for all the normal faults assuming pure dip slip movement; (b) Vectors computed only for scarps not presenting clear signs of erosion\deposition and considering the inferred shear sense. The rose diagrams show the extension weighted circular distributions. Axial vectors were sampled at a 4 km/pixel grid.

Table 4.2 – Circular statistics for the extension vectors of Figure 4.8.

	$\bar{\sigma}$	$\bar{k}$	V	Total extension (km)
Degraded/pure dip slip faults	13±0.2°	1.25	0.47	143.8
Non degraded/oblique slip faults	18.9±0.4°	0.8	0.63	72.2

4.2.1.5 Melas Fossae strain analysis

The set of faults that arise at Melas Fossae can be followed for more than 500 km, until the rift system reaches the Protva Valles region. In this section, only the Eastern part of this rift system will be analyzed.

This area displays a complex evolution, characteristic of a multiphase rift development. Faults cross at least four different stratigraphic units: *Nf*, *Nfd*, *HNt* and *HNr* (see geologic map in Figure 4.3). The high standing cratered and dissected terrains in the Southeast corner of the region depicted in Figure 4.8, show that the deformation was active since the Noachian. Observe how the channel networks that dissect the highlands are aligned with the fractures, and how faults themselves were eroded and concealed by the channels. This shows that some of the fractures were already formed when the channels were carved. All the mentioned structures are older than the plains materials that embay the Highlands (notice that the drainage network is confined to the highland units). To the East, the rift is completely overlaid by the younger ridged plains material (unit *Hr*).

After the first tectonic pulse (now best represented in the Highlands), plains materials were emplaced. Units *HNt* and *HNr* formed in low standing regions burying the previously formed fractures. Those plains were subject to compressive strains and wrinkle ridges formed. The Mazamba crater (see Figure 4.8 for location) formed after the plains emplacement and before wrinkle ridge formation since its crater blanket deposits are deformed by at least one major NE-SW trending wrinkle ridge.

A last distensive episode formed the bulk of the normal faults, which cut the plains materials as well as its wrinkle ridges. Returning to the highlands, note a well preserved set of faults located inside a flat crater floor. Those are interpreted as reactivated faults. In fact, all the second stage normal faults are product of the reactivation of previously formed faults. A Noachian faulted basement should for this reason be present, underlying the younger rift faulted units.

The Mazamba crater seems to have contributed to the rift segmentation. East of Mazamba the rift strikes N60ºW, south of Mazamba a bend exists, and it passes to a more ~E-W trend. Also the arrangement of the faults differs. West of Mazamba the rift is characterized by long linear fault scarps, which form a large scale 200 km sigmoid. East of Mazamba, faults form *en echelon* arrays, and the faults have tens of kilometers. In this part of the rift, it is obvious the generalized left-stepping geometry associated with a dextral shear component.

The Mazamba crater also seems to influence the strain partition along the rift (maps in Figure 4.9b and c show the extension vectors of the fault scarps that dip to the SW and NE quadrants respectively). The western segment of the rift concentrates the faults with higher extension rates. The strain partition in this segment of the rift is not symmetric. The NE dipping faults accommodate the larger extensions. This asymmetry is well perceptible nearby the west rim of Mazamba crater, where a major NE dipping fault holds much more extensive strain than the SW dipping structures in the area.

A SW dipping fault achieves to disrupt the East rim of the crater, but its floor is not faulted. Instead, a rift bend formed outside the crater. This deflection of the fractures, around the crater suggests that the crater acted as a more resistant body, which concentrated the strains South of Mazamba and influenced the style of deformation in the regions located east and west of the crater. Mazamba is not a unique case; note the two smaller craters, with unfaulted inner floors more to the East. Lateral rheological variations, as the ones expected to form due to impact cratering, are usually not taken into account for the tectono-structural interpretation of fracturation patterns on Mars. The given examples shows that maybe those ideas are wrong, and the assumption of fractures developing in laterally homogenous rheological units may be insufficient to explain the variety of tectonic settings that Mars displays on its surface.

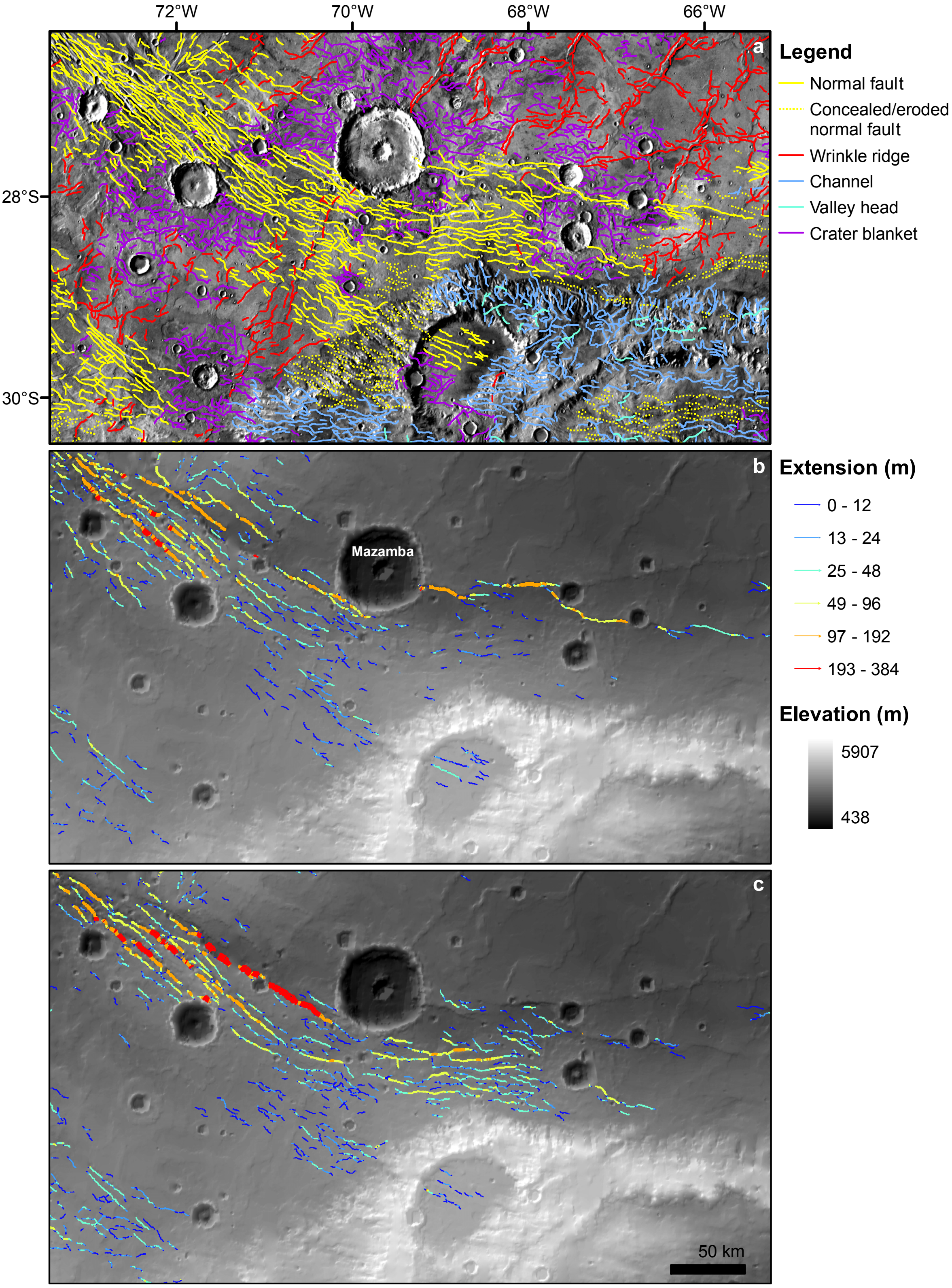

Figure 4.9 - Detailed strain analysis; (a) classified lineament map of the Melas Fossae region; (b) extension vectors for the fault scarps that dip to the SW quadrant; (c) extension vectors associated with NE dipping faults. Only non-degraded scarps were analyzed despite many channels in the degraded craters are aligned with the main NW-SE to E-W trends. Since only vectors located closer than 2 km to a MOLA shot were computed, the vector gaps in (b) and (c) correspond to the larger gaps located between MOLA tracks.

For the section of the rift located east of Mazamba, a strong strain asymmetry is also recognizable. There is a much higher number of NE dipping faults, and they hold the majority of the strain in this region. The SW dipping faults in this area accommodate much less extension, but an array of *en echelon* border faults, which correspond to the North border of the rift structure, present higher extension values.

A transtensive regime is more evident in the eastern portion of the analyzed rift. This observation linked with the higher extensions measured on the western section suggests that the western part may present a more orthogonal extension style. This scenario, with orthogonal extension in the West, soft-linked with a more transtensive regime in the East is kinematically possible. In the future, a strain balance for the entire rift structure would help to clarify this point. Dating the impact crater of Mazamba, through crater counting, would help to establish a lower temporal bound for part of the tectonic activity in the region.

4.2.2 Compressive structures

Wrinkle ridges are the more abundant tectonic structures in the mapped region and they are predominantly located within plain units. Besides those structures, other contractional tectonic features are present in the study area: simple ridges appear usually associated with wrinkle ridges (in the lineament map of Figure 4.4 they were classified as smooth wrinkles); in the SE corner of the mapped area a large lobate scarp corresponding to the Ogygis Rupes is also present. Lobate scarps on Mars tend to occur in highland materials and are interpreted as thrust faults (Watters, 1993).

Wrinkle ridges are considered tectonically formed features originated by far-field compressive stress fields (Watters, 1993; Mueller and Golombek, 2004). This is perhaps the unique consensual view about those tectonic structures. The tectonic processes behind the formation, as well as the subsurface geometry of those features are still debated. They are considered fault-related folds, probably linked with blind thrusts (Schultz, 2000; Montési and Zuber, 2003), but the role of a thick- or thin-skinned tectonic regime is still controversial. Golombek *et al.* (2001) argued in favor of thick-skinned origin, while elastic deformation modeling points to a blind listric thrust fault originating at a shallow *décollement* <5 km deep (Watters, 2004).

4.2.2.1 Wrinkle ridges: trends and general morphology

Wrinkle ridges present three different unimodal circular distributions (see Figure 4.5d). Wrinkle ridges with a left-lateral shear component present a circular distribution with a mean vector trending N131ºE, while the mean vector of the rigth-lateral set strike N74ºE. Pure compressive wrinkle ridges constitute almost 90% of the total of length and trend N16ºE (refer to Table 4.1 for details).

Those trends and kinematics, suggest a conjugated behavior between the dextral and sinistral sets of oblique structures. An angle of 57º exists between those two sets of wrinkle ridges with a bisector plane trending ~N103ºE. This bisector trend is perpendicular to the pure compressive wrinkle ridges, which reinforce the idea that the rigth- and left-lateral oblique wrinkle ridges were formed due to conjugate wrench faulting (Anderson, 1951; Chen *et al.*, 2010). This subject will be discussed in more detail in section 4.2.2.4.

The analysis of the *THI* spatial distribution (Figure 4.10b) reveals that an important morphological difference exists between the wrinkles ridges located in Bosporos Planum and elsewhere in the analyzed region (dashed area I in Figure 4.10b). This spatial segmentation is not visible in the lineament length spatial distribution (Figure 4.10a).

The higher *THI* values for the Bosporos Planum wrinkle ridges indicate that in this area the wrinkle ridges scarps have lower amplitudes. Those *THI* values may also reflect a smaller spacing between the wrinkle ridges (higher spatial frequencies).

The defined area I in Figure 4.10b corresponds to the same area covered by the *Hpl3* unit, named "smooth unit" (Dohm *et al.*, 2001a). It is interesting to point that the *THI* spatial distribution quantitatively supports the qualitative differentiation of that geologic unit. The "smoothness" degree of this unit can be positively correlated with the measured *THI* parameter, which shows for the same area lower amplitude scarps. This correspondence can be used in the future to help to establish morphological units automatically, based on that textural information.

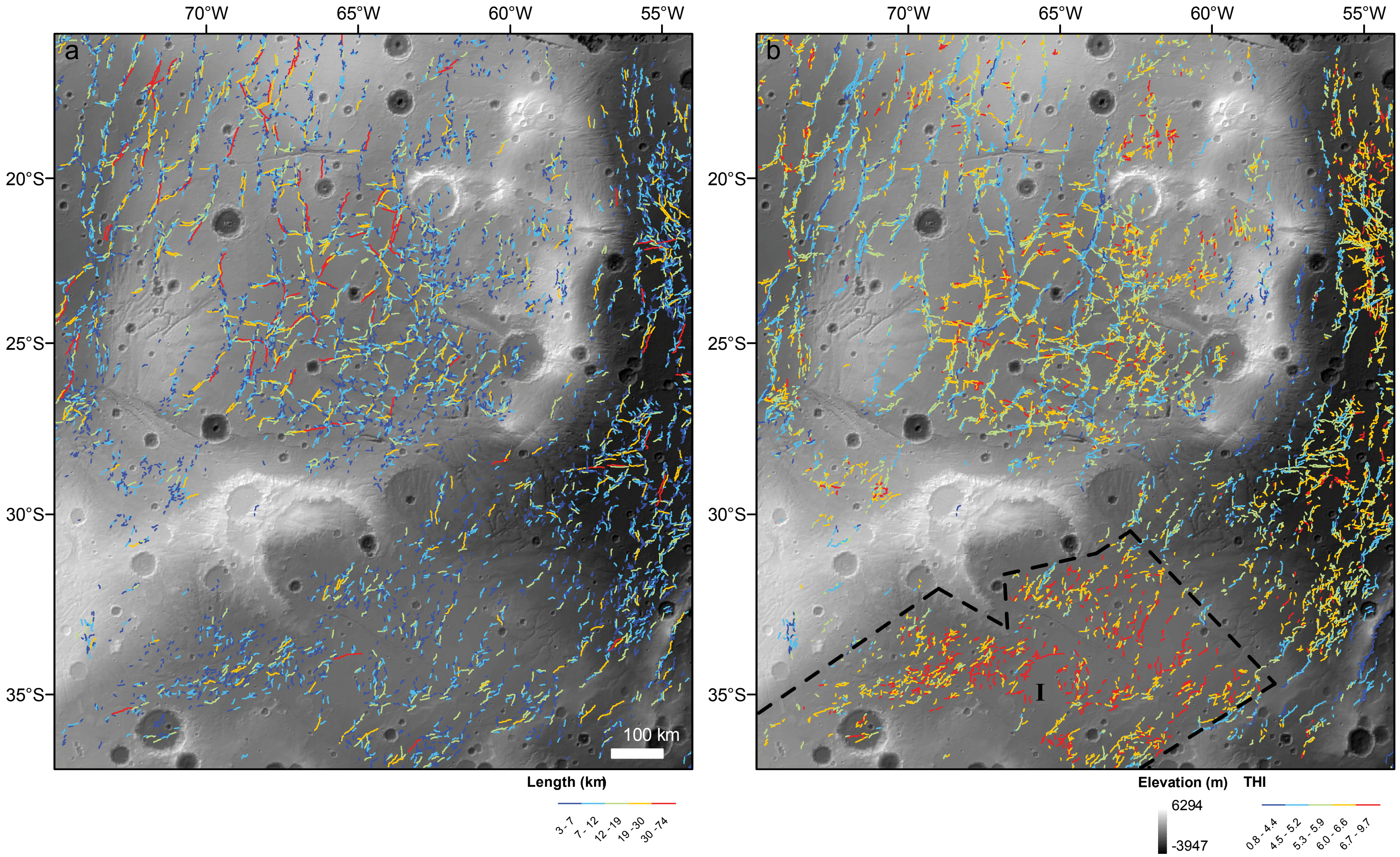

Figure 4.10 - See next page for full legend.

Figure 4.10 – Spatial distribution of the length (a) and *THI* (b) of wrinkle ridges. In this case, despite the good agreement between the differently weighted circular distributions (see rose diagrams in next figure), spatial distributions of the two weighting parameters are not the same. The most striking difference is the area that corresponds to the Bosporos Planum province (area I delimited by dashed lines) characterized by higher values of *THI*.

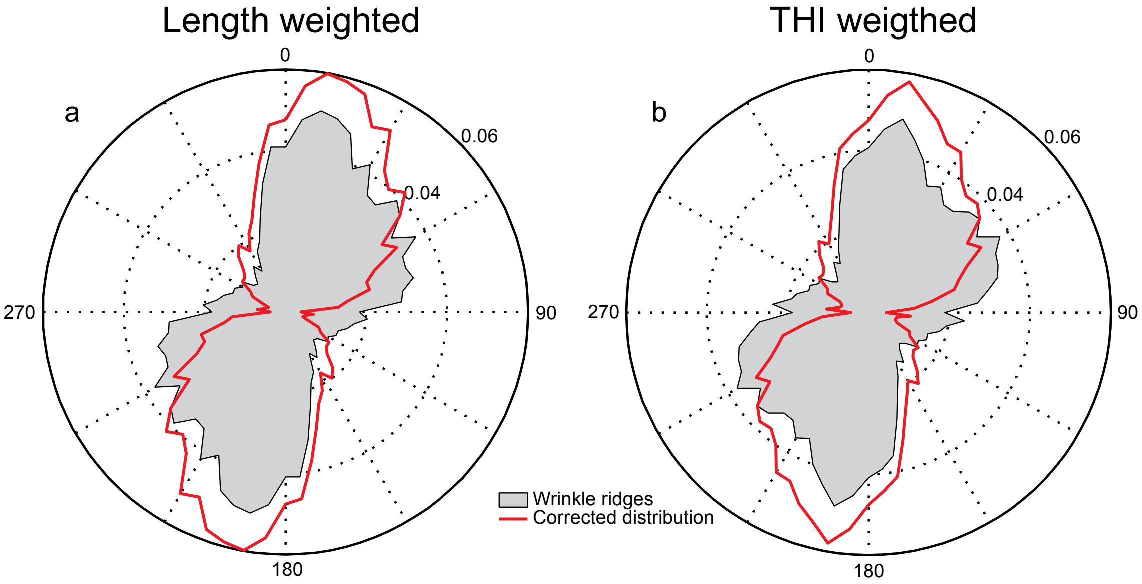

Figure 4.11 - Rose diagram a) present the length weighted circular distribution and b) presents the *THI* weighted circular distribution. Red line distributions correspond to the directional bias corrected distributions (see section 3.4.4).

The presented results show that the wrinkle ridges in Bosporos Planum, present a different morphology. Their scarps are smaller which may be a result of different processes: mantling of the wrinkle ridges by younger eolian, fluvial or vulcanic processes (as proposed by Dohm *et al.*, 2001a); a different style of deformation (induced perhaps by a different mechanical stratigraphy); or smaller strains. The smaller strain hypothesis is also compatible with the resurfacing episode, as long as that episode occurred during the wrinkle ridge formation. This would make that part of the strains would be "lost", and only the post-depositional strains would be measurable.

Length and *THI* weighted circular distributions show the same general features. A same principal mode trending ~N15ºE and signs of a secondary mode at ~N45ºE is visible. This second mode is best seen in the uncorrected rose diagrams (gray patches) since the correction of the MOLA anisotropy reduces the relative weight of those trends.

4.2.2.2 Wrinkle ridges asymmetries

The asymmetry of the wrinkle ridges flanks has previously been interpreted as indicative of the underlying thrust faults dip direction (Schultz, 2000; Mueller and Golombek, 2004). The blind thrusts should dip in the same direction of the backlimb of the folds, this flank being characterized by lower slopes.

The recognition and characterization of those asymmetries has only been made locally (eg. Vidal *et al.*, 2003), and a regional evaluation was never performed. Those issues can be easily addressed using the proposed mapping and morphometric characterization framework.

One way to investigate and visualize possible asymmetries is to create a rose diagram of the aspect angles (the azimuths of the scarps normal vectors) weighted by the height of each scarp. The slope angle can also be used to weight the aspect angles producing identical results.

Since the bounding scarps of the wrinkle ridges were systematically mapped, the proposed diagram shows the relation between the heights and the direction of dip of the scarp flanks. This reasoning can also be conjugated with a spatial segmentation of the analyzed features, which enables to answer questions such as: does an asymmetry exist? Is it more intense in a certain region?

An example is shown in Figure 4.12. Figure 4.12a shows the wrinkle ridges mean elevation histogram. A limit was chosen (dashed line) to segment the wrinkle ridges according to their mean elevation. This segmentation allows to analyze separately the wrinkle ridges located east of Coprates Rise and those located in Thaumasia Planum/Bosporos Planum. Figure 4.12b show the two segmented sub-populations. The rose diagram in Figure 4.12c shows that a flank height asymmetry exists (the gray diagram correspond to entire population). It shows that wrinkle ridges SE dipping scarps have higher heights than NW dipping ones. This asymmetry is stronger for the wrinkle ridges located in the lower terrains east of Coprates rise.

The employed methodology and reasoning proves that the flank asymmetries are a widespread regional characteristic of the ridges. This implies that at a regional scale, the blind thrusts that are probably associated with the formation of the ridges preferentially dip to the NW quadrant.

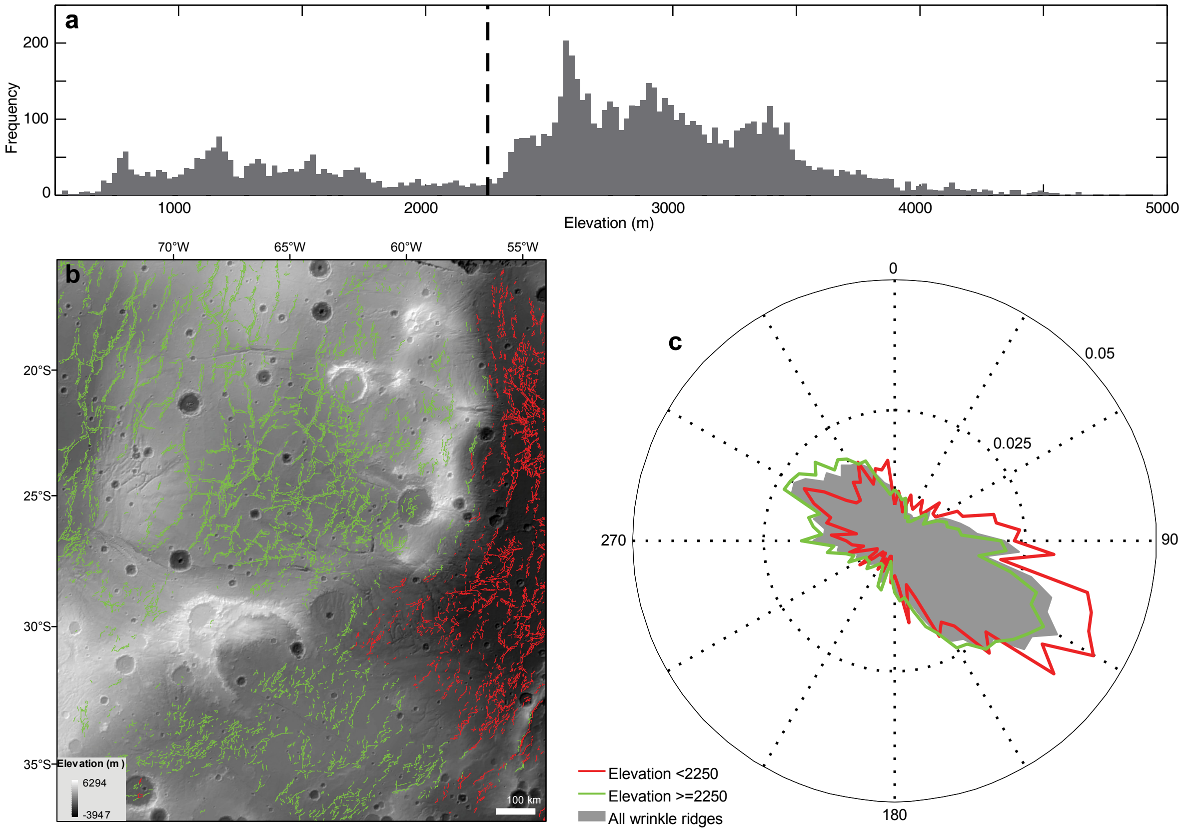

Figure 4.12 – Wrinkle ridge asymmetry; (a) wrinkle ridge mean elevation histogram (dashed limit corresponds to the elevation threshold used to segment the wrinkle ridges in two sub-populations); (b) elevation segmented wrinkle ridges (see (a)); (c) directional histograms of the mean aspect angles weighted by the height of the wrinkle ridge scarps. A strong asymmetry is present between the NW and the SE facing scarps of the wrinkle ridges. The elevation segmentation indicates that this asymmetry is stronger in the eastern lowlands of the analyzed region.

This regional dip direction of the thrusts, inferred from the folds asymmetry, is consistent with a Tharsis centered stress field, especially if a thin-skinned tectonic regime is assumed to be responsible for the formation of the wrinkle ridges.

The characteristic spacing between the ridges is also an important parameter that could be used to model the depth of the fractured brittle layer (Montési and Zuber, 2001; Montési and Zuber, 2003; Anguita *et al.*, 2006). The eastward decrease of the spacing is evident in Thaumasia Planum, which indicates that the depth to a possible *décollement* also decreases eastward. In future works, the automatic measurement of the wrinkle ridge local spacing will be used to estimate the local depth of the brittle layer deformed by the wrinkle ridges.

4.2.2.3 Automatic compressive strain estimation

The uncertainties about the subsurface geometry of the wrinkle ridges difficult the establishment of a concise model which would better constrain the strains and stresses responsible for the formation of those compressive structures.

In this section a simple geometric model will be used to study the strain distribution associated with the wrinkle ridges. This method relies on the measurement of the excess area produced during the folding/faulting that lead to the formation of the wrinkle ridges.

This excess area parameter is already a good indicator of the amount of strain, but if some assumptions are made (especially in the style of deformation), other parameters such as the amount of shortening or the depth to a *décollement* surface can also be estimated. Of course that in this case a thin-skinned regime must be assumed, which as discussed, may be a plausible mechanism for the formation of the ridges.

The generic geometric model used by Colton *et al.* (2006) was extended so that it can be applied automatically at 2D, nevertheless the same model assumptions and limitations are still present.

The geometric model relates the shortening, excess area and depth to a *décollement* in a thin-skinned regime. Colton *et al.* (2006) used that model to estimate the depth of *décollement* by measuring manually in topography profiles two parameters: the excess area (A) and the shortening (ΔL). The excess area was obtained by defining a base level while the shortening was estimated by the difference between the curvilinear surface length (L_i) and the horizontal distance across the wrinkle ridge (L_f).

Several image analysis techniques were used to estimate the same parameters, so that the model could be run automatically and without the limitation of a 1D analysis. In fact, there are a lot of conceptual similarities between the adopted methodology for estimating the compressive strains and the methodology introduced in chapter 2 for the strain analysis of the normal faults. Both were 1D methods that were adapted and automated to allow a fast 2D analysis.

As in chapter 2, several morphological operators were used; the formal definition in mathematical terms of commonly used operator is not presented here. Readers should refer to Soille (2002) for a detailed description of each operator.

A directional iteration is used to analyze different sets of uniformly trending ridges separately. A directional query is performed on the lineament database and a marker matrix m_{α} is created for each iteration (in all the given examples an angular interval of 10º was used). On each iteration, the ridges that strike perpendicularly to an angle α are selected.

Besides the marker image, a maximum admissible width for the ridges must be defined (L_{max}). The defined value must surpass the maximum width of wrinkle ridges under analysis (in all the presented cases a L_{max} of 20 km was used). An elevation matrix f as well as its spatial resolution f_{res} are the others inputs.

The initial marker matrix is subjected to a sequence of morphological operators that allow passing from the one pixel lineaments that mark the ridge scarps to larger objects that mark not only the scarps but also the space between the scarps, in other words, the total extent of the ridges. A closing operation using a disk structuring element (SE) D with radius $L_{max}/4$ is followed by a dilatation using a line structuring element with the same trend as α with a length of $L_{max}/2$:

$$m_{\alpha} = \delta_{\frac{1}{2}L_{\max}\alpha} \phi_{D_{\frac{1}{4}L_{\max}}} \left(m_{\alpha}\right) \qquad \text{(Eq. 4.2)}$$

The initial curvilinear length is computed according to:

$$L_i^{\alpha} = m_{\alpha} \cap \delta_{L_{\max}\alpha} \int^{L_{\max}\alpha} \left[m_{\alpha} \cap \sqrt{\rho_{P_{\alpha}}\left(f\right)^2 + f_{res}{}^2} \right] \qquad \text{(Eq. 4.3)}$$

A morphological gradient computed using a pair of points as SE is used to estimate the vertical component of the distance vectors between each point on the surface. The trend of the pair of points is aligned with α. The horizontal component corresponds to the pixel spatial resolution that gives the distance between neighbor pixels. Since a square grid is used this distance is not constant and depends on α.

The vectorial sum of those two components gives the true distance between the points on the surface. This distance is then intersected with the marker matrix in order to limit the following spatial integration to the areas occupied by the ridges. Note that the integration is performed using a linear SE with size L_{max} and trend α. Finally, a dilatation followed by a new intersection with the marker image ensures that only the local maximum values of the integration are retained.

The final length is computed according to:

$L_f^\alpha = m_\alpha \cap \delta_{L_{\max}\alpha} D(m_\alpha)$ (Eq. 4.4)

The Euclidian distance operator is applied on the marker image, and the same sequence of dilatation and intersection is used to keep only the maximum length along the ridges.

The shortening for a given α is computed by:

$\Delta L^\alpha = L_i^\alpha - L_f^\alpha$ (Eq. 4.5)

Finally, a point-wise maximum operator is used to combine the shortening values obtained for the several α:

$\Delta L = \underset{\alpha}{\vee} \Delta L^\alpha$. (Eq. 4.6)

The same concept used to compute L_i^α is employed to compute the section excess area:

$A^\alpha = m_\alpha \cap \delta_{L_{\max}\alpha} \int^{L_{\max}\alpha} \left[m_\alpha \cap \left(f_{res} \times WTH_{L_{\max}\alpha}(f) \right) \right]$. (Eq. 4.7)

In this case the white top-hat operator is used to compute the height of the ridges above a base level. Those heights multiplied by the pixel resolution give the section area for each pixel. Those areas are then intersected with m_α and spatially integrated as for the L_i^α case. The same sequence of dilatation and intersection with m_α is also applied.

A point-wise maximum is also used in order to combine the excess areas obtained for each α:

$A = \underset{\alpha}{\vee} A^\alpha$. (Eq. 4.8)

The azimuth of shortening α_s is obtained by registering for each pixel the α correspondent to the maximum A^α:

$\alpha_s = \{ \alpha \mid A = A^\alpha \}$. (Eq. 4.9)

The simpler assumption is that the compressive stresses were perpendicular to the ridges. A pure shear regime is for this reason the standard mode the algorithm uses. It will be shown in the next subsection that a rotation of the stresses is perhaps needed to justify some of the more complex arrays of wrinkle ridges.

Following the same thin-skinned geometric model earlier discussed (Colton *et al.*, 2006), the depth to *décollement* (*Z*) can be estimated according to:

$$Z = \frac{A}{\Delta L} \,. \qquad \text{(Eq. 4.10)}$$

The obtained matrices are used to derive a strain axial vectorial field. Since it is not practical to visualize a shortening vector for each pixel, a downsampling is performed for two grid sizes of 2 and 4 km/pixel.

Figure 4.13c shows the computed shortening vector for an area with two sets of intersecting wrinkle ridges. An older set of NW-SE striking wrinkle ridges is intersected by a NNE-SSW more recent set. Note the higher relief associated with the younger set of ridges, which denotes that this set accommodates higher deformations (Figure 4.13a and b).

The small scale corrugations visible in the high resolution imagery (Figure 4.13a) are not present at the MOLA spatial resolution. Nevertheless, the general arrangement of the shortening vectors as well as the relative magnitudes of the shortenings agree well with the visual perception given by the analysis of the DTM (Figure 4.13b).

The MOLA track coverage will also have an impact in the results of this methodology. The local smoothing of the DTM caused by the gaps of MOLA data produces a decrease in the measured strains. See for example the zone pointed with a white arrow in Figure 4.13b. A larger track gap exists in this area, which translates in an area with lower shortenings (see the same area in Figure 4.13c). Small craters superimposed on the ridges may have an opposite impact, making the shortening values increase locally.

A clear interference pattern is visible in Figure 4.13c. This fold interference is reflected in the location of the zones with higher shortenings in the same areas where the ridges intersect. Besides the magnitude of the shortening, the axial vectors azimuths in those areas are disturbed due to the overlay of the two compressive episodes.

The shortening values are far more interesting from a tectonic perspective, but Figure 4.14 suggests that the measured values were underestimated. Compare the distribution of the shortening and excess area values in Figure 4.14a and b. Observe how the along-ridge variation of the excess area is much more gradual than the variation of the shortening values. For this parameter, narrow bands of high and low shortenings are present. This is not expectable or observable in the ridges morphologies.

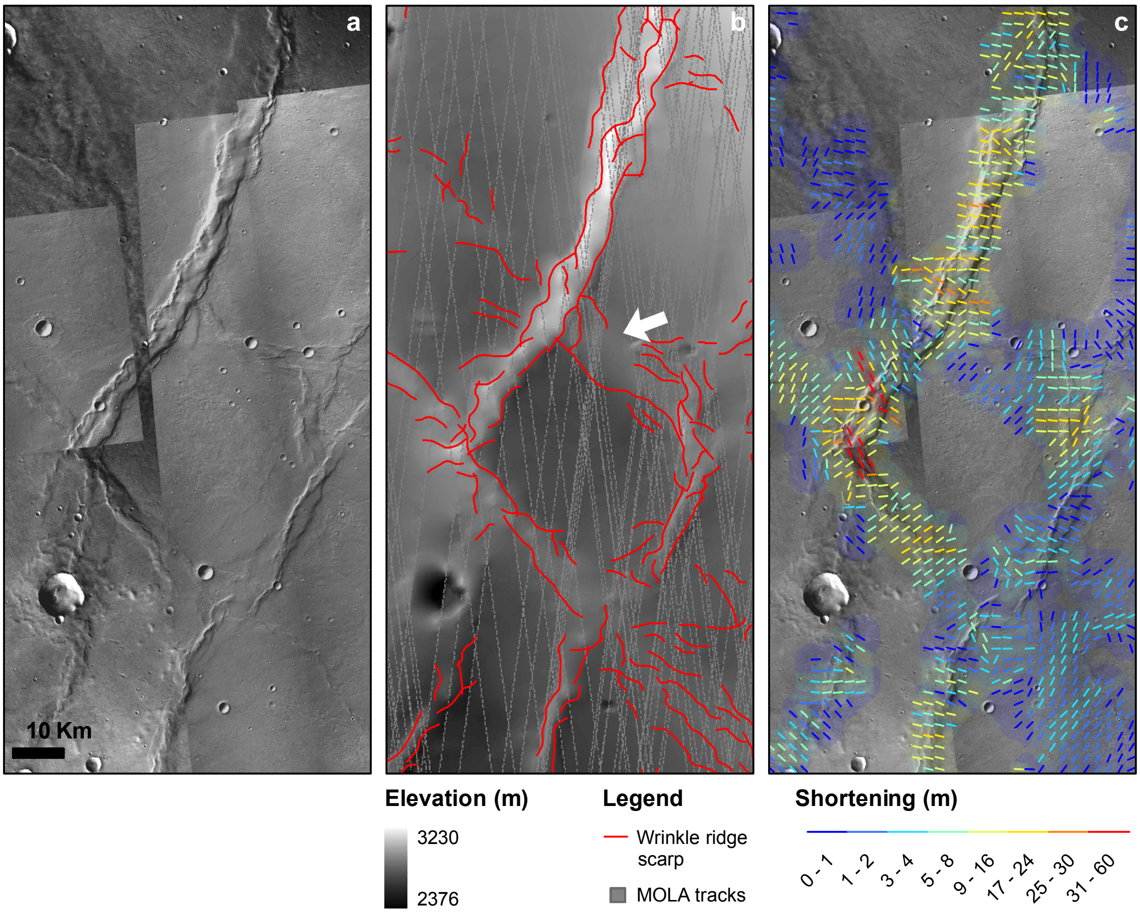

Figure 4.13 – Wrinkle ridges strain analysis of an area were two distinct phases of deformation are present (see Figure 4.18 for location); (a) CTX and HRSC images; (b) mapped wrinkle ridges scarps and MOLA tracks used to derive the DTM. The arrow points to one of the largest data gaps in the area; (c) shortening axial vectors sampled at a 2 km/pixel grid. MOLA coarse resolution and data gaps do not allow the representation of the small scale corrugations well visible in (a) images. Two sets of wrinkle ridges intersect in this area. A NW-SE set is affected by a more intense and recent deformation episode that produced the NNE-SSW wrinkle ridges. A clear pattern of fold interference is recognizable in the location of the maximum strains (in the intersection zones) and in the disturbance of vectors azimuths.

Recall that the shortening is basically the difference between the initial length (the surface final length, or if preferred, the curvilinear length of the curve that links the two extremities of the ridges) and the final length (the actual horizontal extent or width of the ridges). As referred, MOLA data resolution and characteristics do not allow the recognition of the smaller crenulations that are usually found on top of the ridges. This scale cutoff makes that the measured shortening values are certainly underestimated since the measured curvilinear length is always smaller than the reality (Colton *et al.*, 2006).

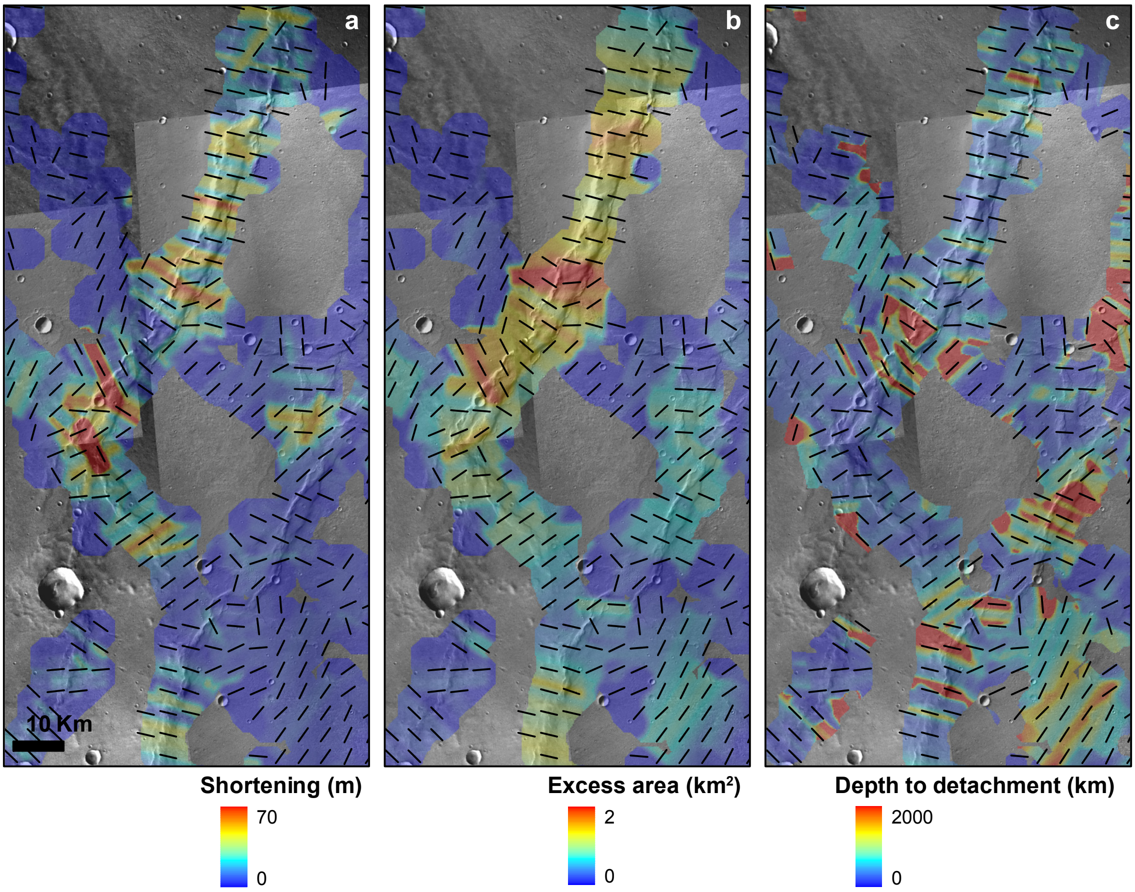

Figure 4.14 – Comparison of the three parameters obtained from the excess area strain quantification technique (see Figure 4.18 for location); (a) shortening; (b) excess area; (c) depth to detachment. The represented vectors correspond to the axial vectors sampled at a 4 km/pixel grid. Note the high lateral variability of the computed shortening values when compared with the excess area values. Since finer details are completely overlooked due to MOLA data characteristics, shortening values should be highly underestimated which produces unrealistic estimations of the depth of *décollement* parameter. The excess area seems to be the more stable and reliable proxy for a future regional strain assessment.

The pointed issues make the shortening values highly sensitive to the spatial resolution and quality of the altimetric data. This explains why the narrow bands with higher shortenings, correspond to the areas where MOLA tracks are present (compare Figure 4.13a and Figure 4.14b, and note that the spacing existent between the bands correspond to the local distance between the MOLA tracks).

The excess area values are distributed regularly. A smoother along-strike variation agrees with the observable morphologies in the DTM and imagery. It is evident that this parameter is less sensitive to MOLA data quality. This is perhaps linked with the fact that the coarse spatial resolution of MOLA data eliminates the smaller crenulations while preserving the main large scale ridge that constitutes the majority of the excess area.

It is for those reasons that the excess area measurement can be considered a better proxy for the amount of strain associated with the wrinkle ridges formation. This parameter can even be used independently of the model assumed for the wrinkle ridges. Even if a thick-skinned model is preferred, the excess area measurement can still give a correct indication of the strain distribution.

Considering the thin-skinned geometric model, the depth of the hypothesized *décollement* was estimated (Figure 4.14c). Even if the conceptual model would fit the real subsurface geometry of the wrinkle ridges, the pointed data and methodological limitations will always difficult the obtention of good estimates. Since shortening values are expected to be underestimated, an overestimation of the *décollement* depth is inevitable.

This is in fact what numeric results reveal. For the region shown in Figure 4.14, computed *décollement* depths reach the unrealistic depths of 2000 km. The same problems were reported for the manual measurements performed by Colton *et al.* (2006). They also interpret the unrealistic *décollement* depths obtained (in their case reaching the 700 km) as resulting from shortening underestimation. Simulating a reasonable constant depth of 50 km they found that measured shortening values only represent 8-24% of the real shortenings, which means that the majority of the deformation is accommodated by small scale structures, which are not discernible at MOLA resolution.

The absolute measured shortenings are for those reasons highly underestimated, which implies that it is not possible to produce meaningful estimatives for the *décollement* depths. Those problems should be addressed in the future. First, better altimetric data such as CTX DTMs (<20 m/pixel) should be preferred to do this kind of analysis. This would overcome some of the MOLA data limitations such as data gaps. The underestimation of the shortenings cannot be overcome only by improving data quality. There will always be present a percentage of strain at finer scales not measurable at a given DTM resolution. Fractal geometry seems the obvious solution for this problem, since it allows handling scale dependant processes.

Because of the pointed limitations, the proposed methodology is mainly considered and used as a first order approximation to the regional compressive strains.

If the absolute magnitude of the obtained shortening vectors is highly underestimated, it is still possible to appreciate its relative spatial variation at a regional scale.

4.2.2.4 Oblique compressive shear

In this section the importance of oblique shear associated with the wrinkle ridges is assessed. The measured length percentage of wrinkle ridges that present signs of oblique slip is 12.2%. As was previously stated, this is a conservative estimative.

In Figure 4.15a a complex array of compressive and oblique compressive structures is displayed (refer to Figure 4.18 for location). A principal set of wrinkle ridges trending N-S is present, forming wide wrinkle ridges in same places presenting *en echelon* arrangements. Those structures are cut and displaced by two other conjugated sets of oblique slip ridges: a left-lateral set striking N128.3ºE and a rigth-lateral one trending N69ºE (this last set presents a higher dispersion of the trends, becoming more E-W aligned in the central part of the analyzed region). It is evident that those conjugated fractures controlled the formation of the N-S structures, acting as transfer faults (see lineament map in Figure 4.15b). But since they also present a ridge-like morphology (with a positive relief) they are considered as possessing a component of compressive strain (even if this component can be minoritary). Transpressive wrench faulting has been previously pointed to exist in the analyzed area by Anguita *et al.*(2006). In the referred work, some of the oblique compressive structures were interpreted as push-up structures associated with basement strike-slip shear zones.

As shown in Table 4.1, an acute angle of 56.2º exists between the dextral and sinistral wrinkle ridges for the entire area. This gives an angle θ of 28.1º between the fractures and the maximum compressive stress (σ_1). For the possible conjugated fractures shown in Figure 4.16 a slightly higher θ of 29.65º was measured.

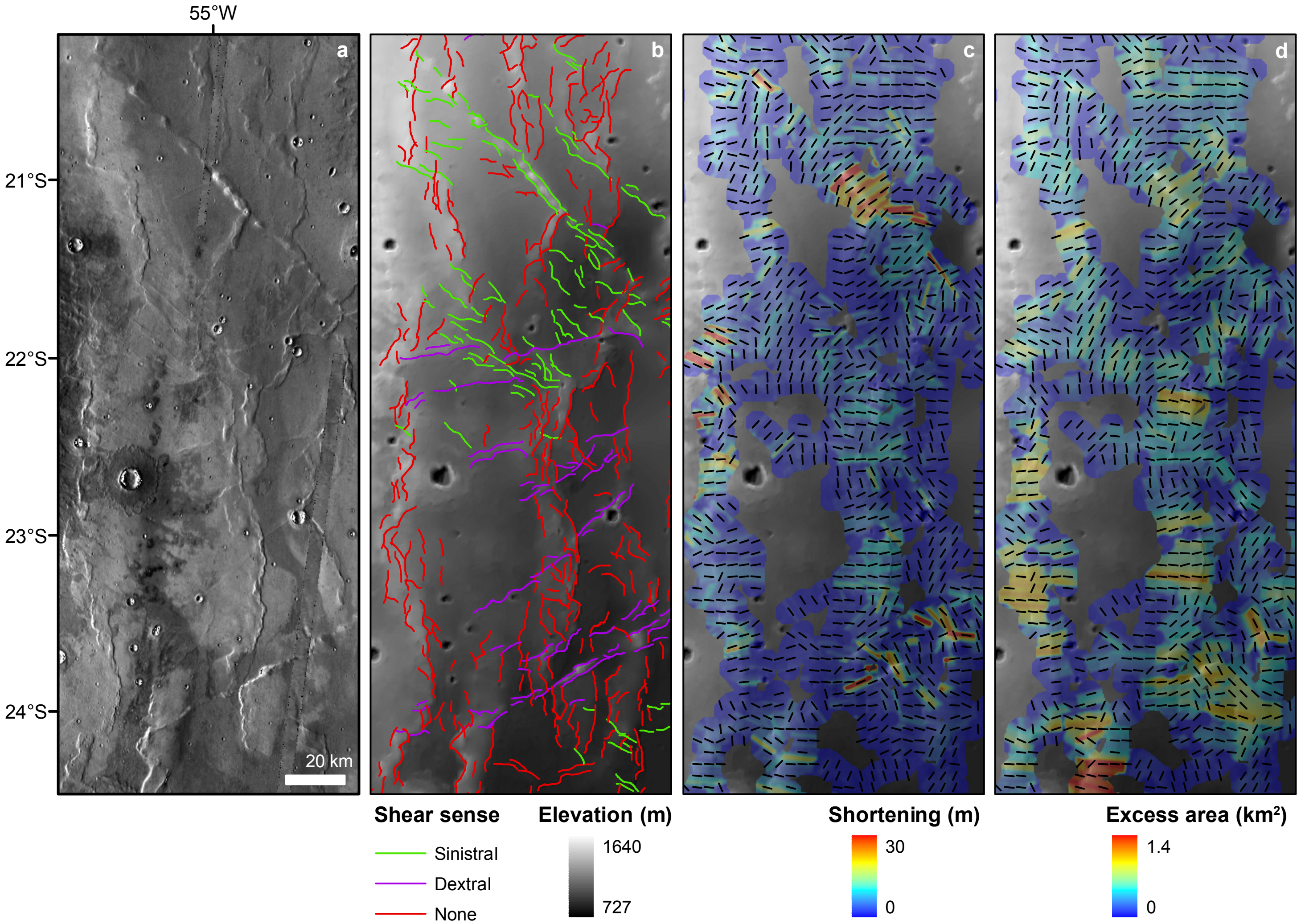

Figure 4.15 - See next page for full legend.

Figure 4.15 – Strain analysis of an area where a complex array of wrinkle ridges is present (see Figure 4.18 for location); (a) THEMIS infrared mosaic; (b) DTM and mapped wrinkle ridges, classified according to the inferred shear sense; (c) shortening; (d) excess area. The shown vectorial field in (c) and (d) corresponds to a 4 km/pixel sampling of the shortening vectorial field computed assuming a pure shear scenario (see next figure for a different approach). In the represented area N-S wrinkle ridges are cut and controlled by two conjugated shear zones, a NE-SW rigth-lateral shear zone located in the South and a NW-SE left-lateral one in the North of the shown area. Horizontal offset of the N-S wrinkle ridges is visible associated with oblique compressive structures. The strains are variable along the structures and they appear to be segmented by the oblique compressive structures.

Recurring to Coulomb's Law of failure, the angle of internal friction (ϕ) can be computed using the relation:

$$\phi = 90 - 2\theta \qquad \text{(Eq. 4.11)}$$

(Davis and Reynolds, 1996), which gives a ϕ of 33.8º for the entire population of possible conjugated fractures in the East Thaumasia region. An internal friction angle of 30.7º was obtained for the possible conjugated fractures shown in Figure 4.16. Those values are within the range of internal friction angles for most rocks, 25º-35º (Davis and Reynolds, 1996).

Other possible conjugated sets of strike-slip faults on Mars were identified by Okubo and Schultz (2006) West of Olympus Mons. In that case, a lower ϕ angle of 20º was computed. As noted by the Authors, this angle is compatible with the 14-25º friction angles estimated for Mars jointed layered basaltic rock-masses located in the Valles Marineris walls (Schultz, 2002). This suggests that the higher friction angles obtained in the presented case are more representative of fractures developing in unfractured rocks, in an Andersonian strike-slip scenario (Anderson, 1951).

The horizontal offset of the N-S structures along the transpressive conjugated structures is puzzling. For a same oblique structure, the apparent offset for successive N-S wrinkle ridges seems to change. One justification would be that the transpressive structures formed at the same time of the main compressive structures. But the only scenario that can be surely excluded is the one where the transpressive structures would form after the formation of the N-S wrinkle ridges. In this case, and assuming that the wrinkle ridges would not be reactivated, the horizontal offsets would be constant.

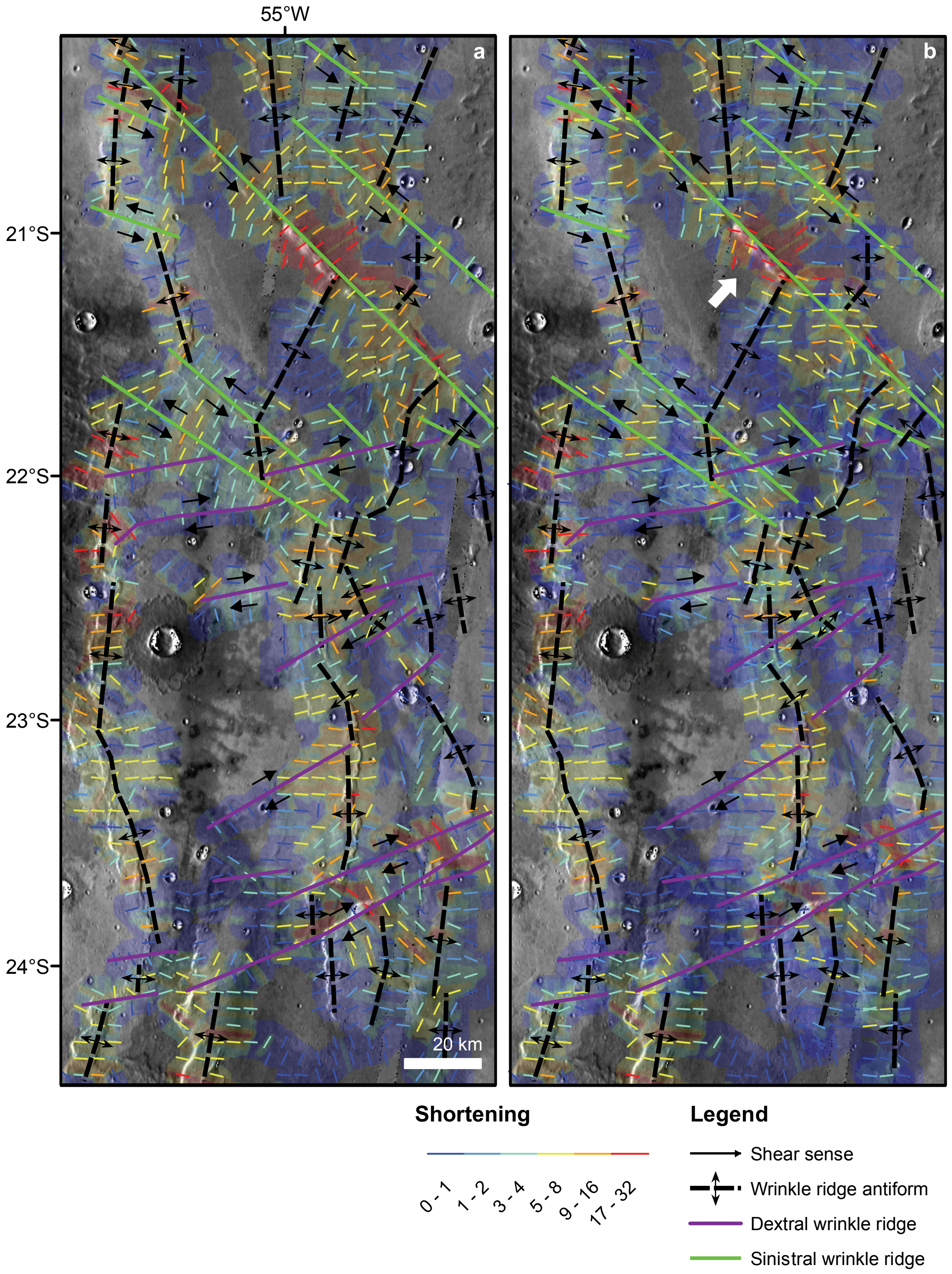

Figure 4.16 – Tectonic interpretation and model comparison between a pure shear scenario and a simple shear approximation; (a) shortening vectors computed for a pure shear scenario where compression is always orthogonal to the tectonic structures; (b) a simple shear approximation where shortening magnitude is computed as in the pure shear case, but where for structures presenting signs of transpression the strain vectors suffer a rotation of 60º, clockwise or anticlockwise depending if the shear sense is sinistral or dextral. Compare the different vector directions in the vicinities of the oblique wrinkle ridges. See text for discussion.

In maps c and d of Figure 4.16 the computed shortenings and excess areas are displayed. It is hard to interpret the strain distribution in this area, but a high along strike segmentation of the strains is patent. A pure shear setting, with the strain vectors trending orthogonally to the ridges was used to compute the shown compressive strains. A more comprehensive strain analysis can only be made if the transpressive nature of the oblique ridges is incorporated in the model.

As in the case of the analysis of the transtensive strains, the simpler solution is the rotation of the strain vectors associated with the structures that present oblique slip, emulating in this way a simple shear regime. A choice for a unique angle of rotation was made iteratively in areas where the pure compressive and transpressive structures interact. The objective was to make that in these areas the azimuths of the transpressive vectors approximate those computed for the compressive structures. The best fit was obtained using a 60º rotation, clockwise for the sinistral and anticlockwise for the dextral structures. The rotation does not change the magnitude of the shortenings, since those are still computed according with the described methodology.

This straightforward scheme used to approximate the strain trajectories associated with the transpressive structures can still be improved if instead of a fixed rotation, as the one used, the quantity of horizontal slip along the structures is incorporated into the model. This may be only practicable in areas where other structures were displaced by the strike-slip movement, allowing the local measurement of the strike-slip component associated with the transpressive structures.

The comparison of the two discussed approaches is shown in Figure 4.16. An interpretative sketch was added to help the comparison of the models. Compare with special attention the azimuth changes of the strain vectors in the vicinities of the transpressive structures. The modeled strain trajectories in Figure 4.16b better represent the transpressive nature of those structures. The shortening vectors are no longer orthogonal to the structures (see Figure 4.16a), which would prevent the development of a strike-slip strain component. Instead, a 30º angle exists between the transpressive structures and the strain trajectories, which agrees with a transpressive regime.

The tectonic sketch overlaid on the strain vector also gives a new insight on the strain segmentation. A main N-S segmentation is present, and it can be linked with the action of the transpressive strain transfer systems, that transect the main compressive N-S trending structures.

The deformation along the NW-SE trending structures is also segmented. The white arrow in Figure 4.16b points to a region that accommodates higher strains. This region is comprised between two displaced wrinkle ridges and the horizontal offset is approximately 20 km. This is another observation that supports a contemporary formation for the two sets of features. Not only the N-S set development was conditioned by the strain transfer along the conjugated transpressive structures, but also the evolution of that transpressive regime was conditioned by the presence and formation of the ridges.

The comparison of the circular distribution of the shortening vectors for the two models reveals that the simple shear approximation gives a different circular distribution (Figure 4.17). Perhaps the best prove that the proposed methodology gives more precise indications of the trends of regional compressive strains, is the fact that the circular distribution computed for the Figure 4.16b case presents a lower circular dispersion. The computed circular variance for the simple shear approximation case is 0.36, while a variance of 0.72 was found for the pure shear case (see Table 4.3). The concentration parameter $\bar{k}$ differences are even greater (recall that $\bar{k} = 0$ correspond to a uniform circular distribution).

This shows that the second approach is a better method to estimate the trend of a regional σ_1. Besides differences in the variance, the two methods produce different mean trends. A significant difference of 16.5º between the two computed mean trends exists. This is particularly important because it shows the impact of the choice of a given shear model to derive a regional compressive direction.

Pure shear regimes were preferentially used to evaluate and analyze the tectonic patterns at a global scale (Anderson *et al.*, 2001; Anderson *et al.*, 2008). The simpler assumptions of stresses aligned with normal faults, and orthogonal to all the mapped compressive structures lead to the definition of several (perhaps too many) tectonic centers. Thirteen of those centers were identified in the Tharsis region (Anderson *et al.*, 2001), while four more centers were statistically defined for the eastern hemisphere of Mars (Anderson *et al.*, 2008).

The detailed tectonic analysis of the given examples, the strain models, and the numeric comparison of the pure and simple shear models strongly suggest a simple shear framework. Those arguments points to the need to review the mentioned tectonic centers to better understand the processes responsible for the stresses. Such a review will certainly decrease the number of probable stress sources, since a simple shear regime implies that under a same stress field a higher variety of tectonic structures may form with different trends and kinematics.

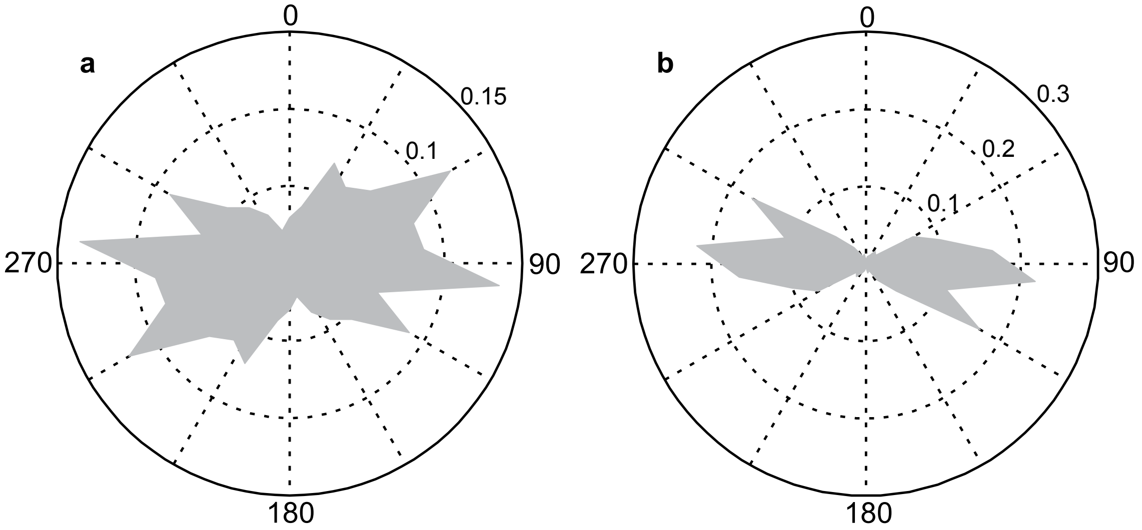

Figure 4.17 – Rose diagrams of the shortening vectors shown in Figure 4.16; (a) diagram for the pure shear case (Figure 4.16a); (b) diagram for the simple shear approximation case (Figure 4.16b). A mean vector trending 80±2° and 96±0.8° was computed for (a) and (b) respectively. The case (b) distribution has a lower circular variance of 0.36 versus 0.72 of the pure shear case (a circular variance of 1 correspond to a uniform distribution), this strongly suggests that the proposed model is a better solution when the objective is to identify the direction of a regional σ_1. The difference between the obtained mean vector azimuths show the importance of a correct kinematic interpretation of the mapped structures in order to better constrain the stress fields.

Table 4.3 – Circular statistics for the shortening vectors of the two models shown in Figure 4.16. See Figure 4.17 for the rose diagrams.

	$\overline{\sigma}$	$\bar{k}$	V
Pure shear	80±2.1	0.59	0.72
Simple shear	96.5±0.8	1.67	0.36

4.2.2.5 East Thaumasia compressive strains

The developed methodologies for wrinkle ridge strain estimation were applied to the entire East Thaumasia region (Figure 4.18). The introduced approximation to a transpressive model was used.

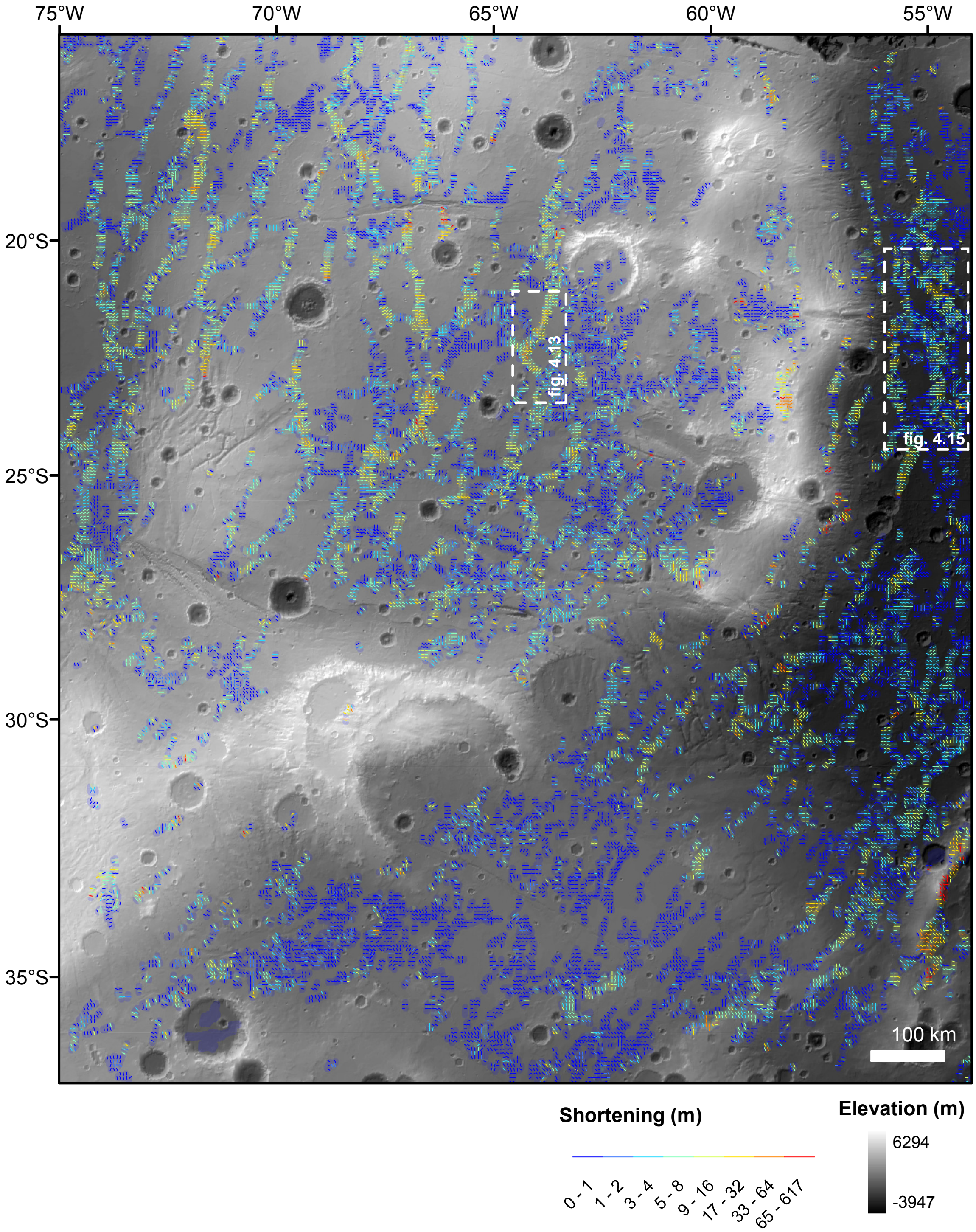

Figure 4.18 – Wrinkle ridge shortening vectors computed using the excess area technique. Note the low shortening values for the Bosporos Planum region. The axial vectors were sampled at a 4 km/pixel grid.

The previous morphometric analysis reveals that the wrinkle ridges located in Bosporos Planum are smaller. This is obviously also reflected in the measured strains: note the lower shortening values obtained for that region.

In the Melas Dorsa and Thaumasia Planum regions, the majority of the shortening is related with the ~N-S striking wrinkle ridges. In Thaumasia Planum, shortenings decrease eastward, particularly eastward of Lassel crater (see Figure 4.2 for location). In fact, Lassel crater may be locally responsible for the concentration of the strains more to the West. Notice how the larger strains are concentrated nearby the western rim of this dissected crater. North and South of the rim the deformation was less intense. As for Mazamba crater, this supports the view that craters can act as rigid bodies, influencing the stress trajectories and strain localization during regional deformation.

High strains were obtained for the lowlands located east of the Coprates Rise. In this area not only magnitudes are high, but also the deformed area is large. Compare the size of undeformed areas in Melas Dorsa with the almost inexistent undeformed patches in the East Coprates Rise trough.

The highest absolute strains are concentrated in the Ogygis Rupes area (in the SE corner of the study area). As was mentioned earlier, lobate scarps are present in this area. Those structures are more likely associated with a thick-skinned tectonic regime and they form broader relief morphologies. Since the maximum considered width for the modeled ridges was of 20 km, the computed strain values are underestimated because lobate scarps are much wider. Despite this, the obtained shortenings for the area are still among the highest measured values.

In order to compare the trends and magnitudes of the strains, four zones were defined (Figure 4.19a). The main limit between the zones follows the Coprates/Thaumasia Highlands arch, while secondary boundaries were defined by following the Melas Fossae/Protva Valles and North Thaumasia Planum rift/Lassel crater alignments.

Shortening vectors in each zone were analyzed separately. Since a lower circular variance was computed for circular statistics in zone I, the shortening in this area is more concentrated around a mean vector trending N99ºE (Table 4.4). Shortening mean trends of N107ºE and N108ºE were computed for zones II and IV respectively. The circular distribution of the strains in zone III is bimodal with two modes striking N110-120ºE and ~N160ºE. This bimodality agrees with the bend of the large scale Coprates/Thaumasia Highlands arch. The circular diagram for the entire region (Figure 4.19b) also shows this same bimodality. The Melas Fossae/Protva Valles right-lateral shear zone marks the limit between two major tectonic provinces. One in the South, best represented at Bosporos Planum and with a main compression trending ~N160ºE. And the other province located north of the shear zone characterized by a set of tectonic structures more compatible with a N107-108ºE regional σ_1. Finally, a third province can be also recognized as corresponding to the zone I (with a σ_1 trending N99ºE).

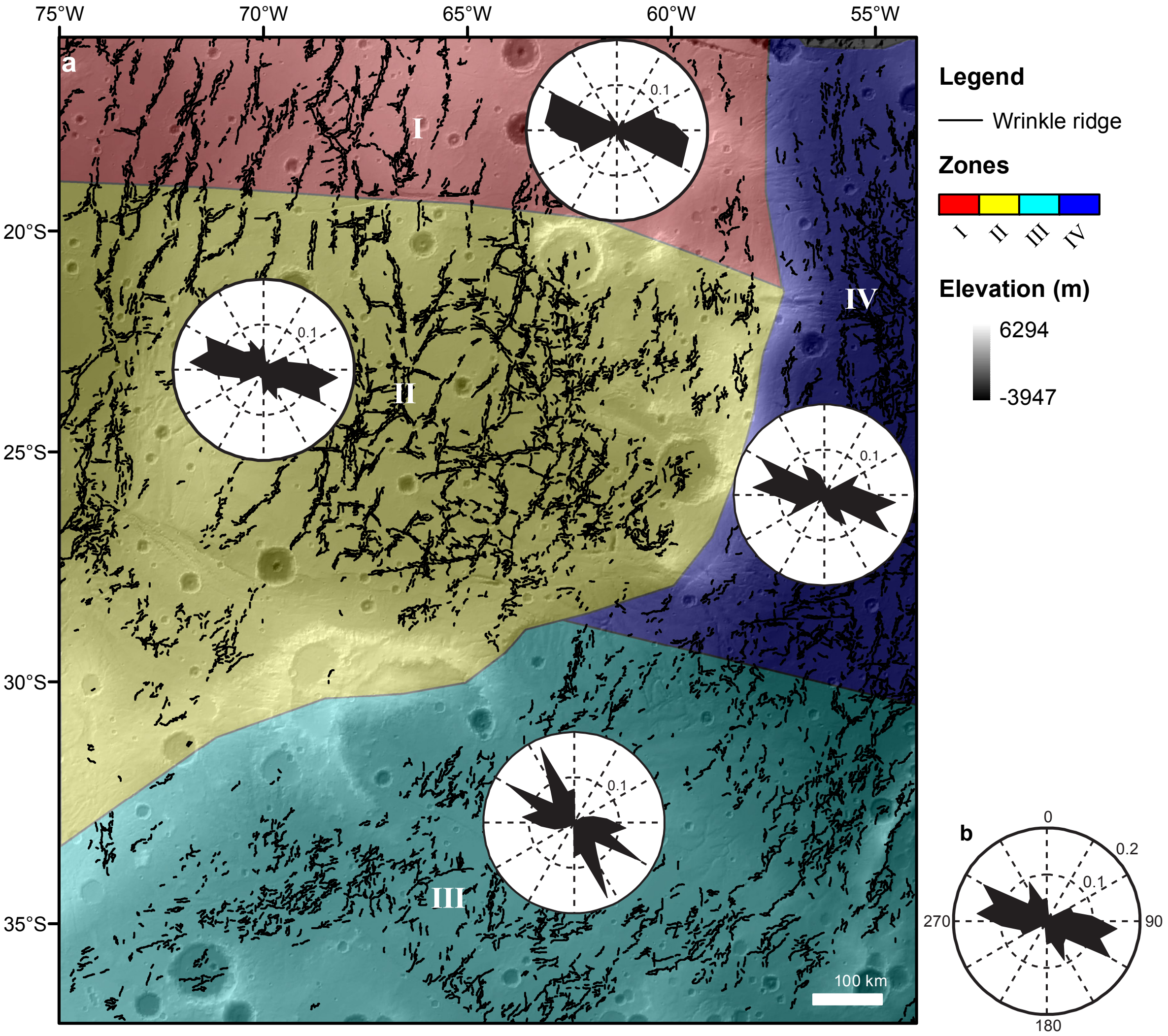

Figure 4.19 – Shortening vectors rose diagrams per zone; (a) shortening rose diagrams computed for each defined area; (b) rose diagram for the total area. See Table 4.4 for circular statistics associated with each diagram. A good agreement exists between zones I, II and IV. A clockwise rotation is perceptible from North to South. The circular distributions in zone III is bimodal and is constituted by a mixture of two main components, ~N120ºE and ~N160ºE. The overall distribution is also bimodal, with a main mode at ~N105ºW and a minor one at ~N160ºW.

Table 4.4 – Shorthening vectors circular statistics per defined region. See Figure 4.19 for the boundaries of the defined zonation and for the rose diagrams.

Zone	$\overline{\sigma}$	$\overline{k}$	V	Shortening (km)	Zone area (km^2)	Shortening/area (km/km^2)
I	98.5±0.2	1.29	0.46	37.4	357351	1.0E-04
II	108.4±0.1	0.91	0.59	145.4	693273	2.1E-04
III	129.2±0.2	1.03	0.54	72.0	592871	1.2E-04
IV	107.2±0.2	0.95	0.57	55.0	241942	2.3E-04
Total area	111.5±0.1	0.91	0.59	309.8	1885437	1.6E-04

The proposed provinces denote a northward anticlockwise rotation of the principal stress axis during wrinkle ridge formation. The proposed provinces are segmented by two main ~E-W transfer structures: one more evident, the Melas Fossae/Protva Valles and the other less obvious corresponding to the North Thaumasia rift/Lassel crater alignment.

The agreement between the wrinkle ridge stress field trajectories and the larger scale buckling/thrusting structures is remarkable. This is another good indication that the two types of structures, even if representing two very different scales and styles of deformation (probably thin-skinned for the wrinkle ridges and thick-skinned for the buckles, Anguita *et al.*, 2001; Anguita *et al.*, 2006), are compatible with a unique stress field.

The shortening per area ratio allows to compare the amount of shortening affecting each zone. The higher ratio belongs to zone IV while ratios in zones I and III are almost half (Table 4.4). Those values show that the central and eastern regions of the analyzed area are much more deformed. Those variations of strain can be explained by the action of the two mentioned ~E-W transfer structures that form bands with different ratios of strain. Those bands are easily recognizable on the highlands Noachian terrains, while in the Noachian-Hesperian plain units they are not so obvious. What the presented wrinkle ridge strain analysis reveals is that despite those structures having been concealed by the deposition of the plain units, the control of the wrinkle ridge formation is in great part made by the dextral ~E-W shear bands.

In summary, everything points to a basement controlled thin-skinned tectonic regime forming a rich array of compressive and transpressive structures that at surface form the characteristic morphologies of the wrinkle ridges. Those relatively small scale structures are the product of a unique stress field. This later stress field has the same principal compressive trend responsible for the development of the larger scale buckles that form the Coprates/Thaumasia Highlands arch.

4.2.3 Other structural indicators

Other types of mapped scarps are not directly linked with tectonic activity, but reflect the local structure of the geologic units (Figure 4.20). The characterization of those scarps is made essentially using high resolution imagery. The identified scarps are in some cases not easily recognizable in all the imagery datasets (see the example in Figure 4.21b). The general procedure for the identification and characterization of those structures generally implies a sequence of actions:

1. an automatically mapped lineament is not recognizable in coarse resolution imagery (usually THEMIS infrared imagery with 100 m/pixel);
2. confirm if MOLA track coverage in the scarp region is good;
3. if the MOLA coverage is good (meaning that the scarp is really there) higher resolution datasets (HRSC, and CTX images) are used to try to identify and characterize the scarps.

The most abundant features are scarps that present layering. Those scarps have generally low heights (a mean height of 25±34 m was measured) and an apparent fine horizontal layering is predominant. They are widespread across all geologic units. Plain units seem to present some areas where those structures appear more clustered. Note the mapped high concentrations in the Thaumasia Planum region (mainly west of Coprates Rise) or in the Bosporos Planum/Protva Valles regions.

Mesas were also identified, and the mesa scarps can also present horizontal layering. Those structures are rarer and they appear again associated with the Bosporos Planum/Protva Valles regions and with the West flank of the Coprates Rise

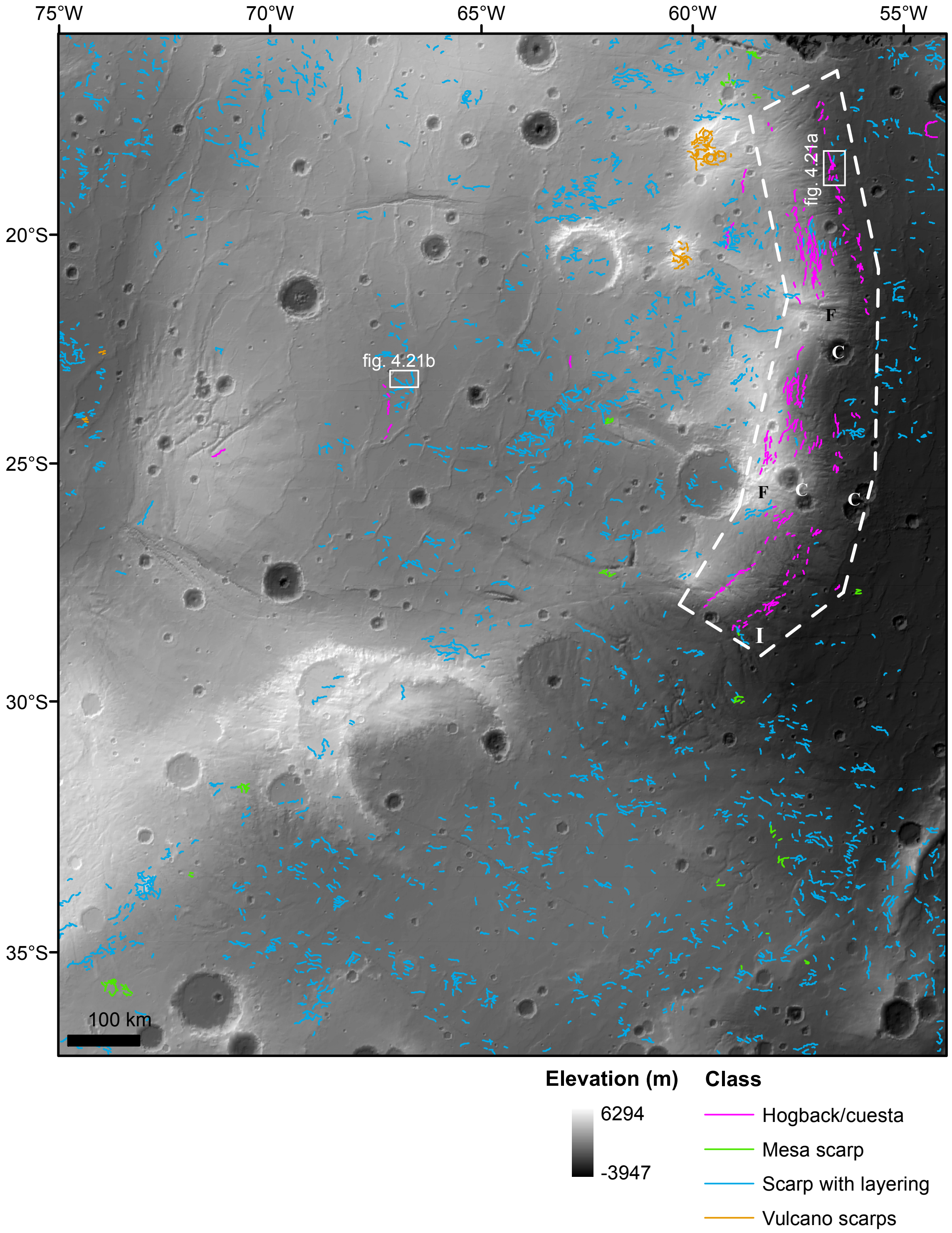

Figure 4.20 – Spatial distribution of scarps that present a structural significance. Two volcanoes presenting highly dissected flanks are the main volcanic features in the area. Scarps where horizontal bedding is visible in imagery are widespread over the entire area, forming in same places mesas. The height of those scarps is in general low (a mean height of 25±34 m was measured). Scarps with tilted layers were recognized under the form of cuestas/hogbacks (the real dip was not compute so the two possibilities are considered). These structures occur mainly along the Coprates rise (dashed area I) with a constant East dipping direction. These structural continuity is locally disturbed by cratering (C), faulting (F) and drainage networks.

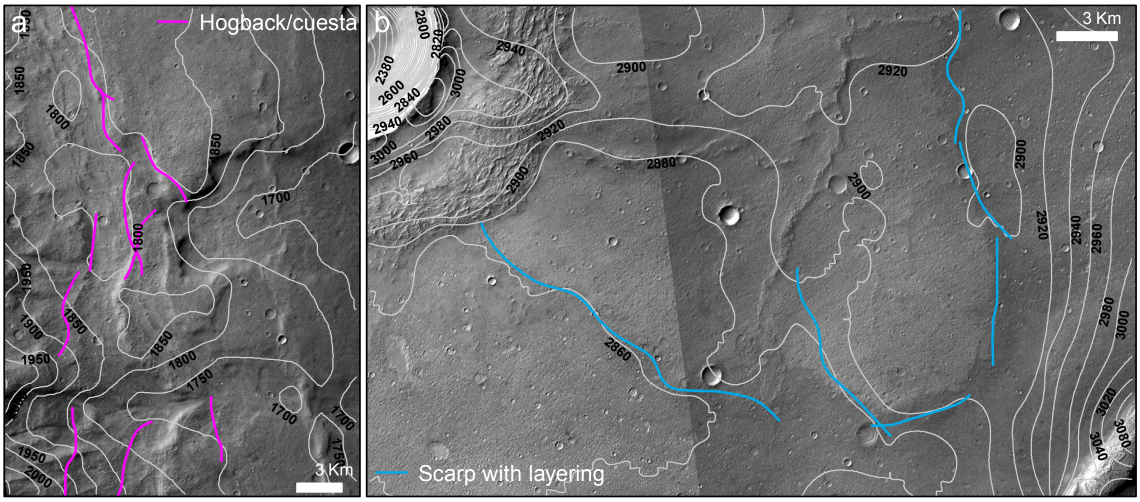

Figure 4.21 – Detail of some of the mapped bedding structural scarps overlying CTX images (see Figure 4.20 for location); (a) East dipping beds forming a hogback/cuesta structure. Note that the alternating sequence of layers is cut by channels that flowed to the East; (b) set of scarps associated with horizontal or smoothly dipping layers. These gentle scarps are only noticeable in the images due to a difference in albedo. In this case since there are no shadows it would be very difficult to characterize the overall structure if only the CTX images were used.

These two classes of scarps imply the following sequence of events: deposition of layered sequences of materials (possibly of volcano-sedimentary origin) followed by erosion that reveals the internal layering of the sequences. In some cases a tectonic control could have contributed to the subsequent erosion. Note how in the Thaumasia Planum the scarps with layering are located between the wrinkle ridges. The compressive strains responsible for the ridge formation may also affect the sediments located between the ridges. In those cases a slight tilt of the layer can help to form the layered scarps.

The main processes responsible for scarp erosion and retreat are probably eolian and fluvial. The fluvial processes are especially evident for the Bosporos Planum/Protva Valles regions.

Highly dissected volcano scarps are associated with the two volcanoes located east of Lassel crater. Those Noachian-Early Hesperian volcanic edifices are probably constituted by an alternation of lava flows and pyroclastic deposits characteristic of explosive activity (Dohm and Tanaka, 1999). The highly dissected flanks support this possibility.

Scarps presenting tilted strata were also identified in the study area. Since the dipping angle was not computed, all the scarps were merged in a single class named hogback/cuesta. Qualitatively, gentle dipping angles are associated with some of the layers visible in scarps located in the vicinities of wrinkle ridges in the Thaumasia Planum region. This association suggests that the morphologies correspond to cuestas formed during wrinkle ridge development.

The most important sets of tilted strata occur in the East flank of the Coprates Rise (see Figure 4.20 region I). In this area a set of East dipping layers can be laterally followed for more than 800 km, along the entire Coprates Rise bulge.

Differential erosion of the tilted beds along the Rise produced triangular faceted hogbacks (see Figure 4.21a), as noted by Schultz and Tanaka (1994). The presented mapping gives more emphasis to the regularity and lateral continuity of the layering. But the most intriguing is the recognition of two different layer sets. Figure 4.22 shows the standard deviation elevation interval for each hogback scarp in region I. From South to North the scarps tend to form two main sets with tilted layers, one at 1500-2000 m and the other at 3000-3500 m. In the central region, cratering and faulting are responsible for the disruption of the layers (see C and F labels in Figure 4.20 and the gray areas in Figure 4.22).

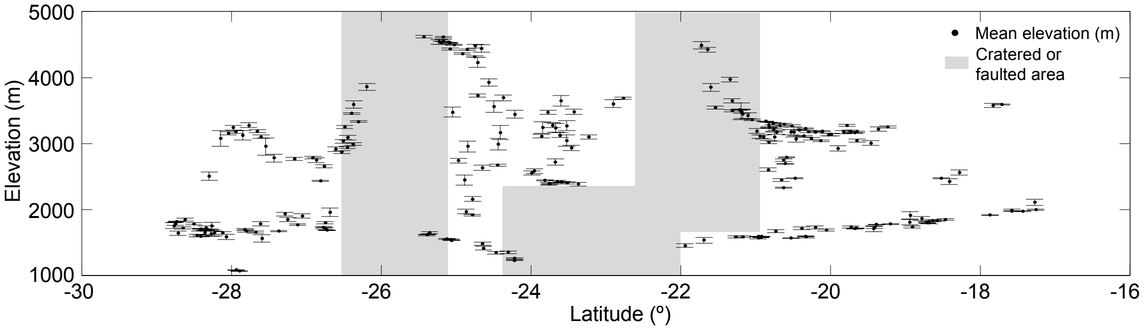

Figure 4.22 – Plot showing the South to North vertical distribution of the hogbacks/cuestas scarps present in Figure 4.20 region I. The mean elevation as well as the standard deviation interval associated with each measurement is shown. Gray patches correspond to areas where faulting and cratering have disrupted the lateral continuity of the structures (refer to C and F label in Figure 4.20). Nevertheless two main sets of layers emerge approximately at 1800 and 3200 m and present an apparent large lateral continuity spanning more than 800 km.

Those apparently continuous layers constitute excellent tectonic markers to investigate the deformation along the Coprates Rise front. It is also one of the best outcrops of highland layered materials on Mars, whose stratigraphy is of major interest. One interesting possibility is, for instance, the characterization of a possible angular unconformity between the two units. This would imply that the youngest one (the one standing at lower elevations) may have formed syn-kinematically with the formation of the buldge. A lower apparent dip as already been assigned to those layers by Anguita *et al.* (2006) who related those apparent dip differences with a basement-cover unconformity.

A future detailed study of those layered deposits will need a better geometric characterization of the attitude of the layering, especially of the measurement of the layering dip angle along the Rise. The methodology used by Fueten *et al.* (2005) for measuring the attitude of the layered deposits in Valles Marineris is a good starting point.

In terms of layered sequences, a clear contrast exists between the Coprates Rise and the Thaumasia Highlands more to the Southwest. Those tilted layered sequences are completely absent in the mapped segment of the Highlands. Again, the Melas Fossae/Protva Valles dextral transfer structure separates two different structural provinces marked by a large dissected and tilted crater located in the South.

It is perhaps time to raise a new issue: are the morphologic and structural differences found between these two sectors a consequence of a different architecture of the frontal buckles/thrusting that constitute the Coprates/Thaumasia Higlands arch?

From the presented analysis, three main arguments can be invoked to support this possibility:

- the compressive strains measured for the wrinkle ridges in the Bosporos Planum are approximately half of the deformation measured for the Coprates Rise frontal lowlands (this is only true if wrinkle ridges in Bosporos Planum were not covered by later sedimentary deposition);
- the mentioned tilted strata are only present in the Coprates Rise East flank;
- the Melas Fossae/Protva Valles dextral transfer structure is a major structure, active during Noachian to Early Hesperian age, whose kinematics can justify a differential behavior of the frontal bulges.

The Thaumasia Highands and the Coprates Rise bulges were always considered a more or less continuous structure formed by lithospheric buckling and perhaps thrust structures (Schultz and Tanaka, 1994; Dohm and Tanaka, 1999; Webb and Head, 2002; Borraccini *et al.*, 2007; Montgomery *et al.*, 2009). Contrary to those views, the presented data and interpretations support a stronger differential evolution of the two provinces that are separated by the Melas Fossae/Protva Valles transfer structure.

Thrusting along the bulge was always considered a possibility, since direct evidences were not found. What the analysis of the study area reveals is that, even if only one possibility, this lithospheric thrusting is perhaps restricted to the Coprates Rise front, while the examined Thaumasia Highland small segment is more akin to only buckling. Nahm and Schultz (2010) having modeled and tested the possibility of orogenic thrusting in the Southern Thaumasia Highlands, concluded that the bulge topography is not consistent with an orogenic thrusting wedge. The presented analysis did only cover a small portion of the Southern Highlands, nevertheless the proposed scenario agrees with their conclusions. A complete mapping of the remaining portion of the Southern Thaumasia Highlands can help to clarify this point. However, that new mapping effort will probably not change the introduced hypothesis for the study area, which restricts/favors the possibility of thrusting only to the Coprates Rise bulge.

4.3 Hydrologic characterization

In this section, the hydrology of the study area will be succinctly analyzed. The relation between tectonic processes and the hydrologic circulation will be particularly emphasized.

The main period for valley network formation in the high cratered terrains is thought to have ended at the Noachian/Hesperian boundary (Fassett and Head III, 2008). This limit is also consistent with the decline in the erosion of the cratered highlands. During Noachian times, fluvial activity was widespread and wet and warmer conditions allowed the formation of phyllosilicates (Bibring *et al.*, 2006; Mustard *et al.*, 2008).

A slightly different interpretation suggests lower dissection rates during the Noachian, followed by a main fluvial activity during a later intense valley formation stage (Late Noachian-Middle Hesperian) (Howard *et al.*, 2005; Irwin *et al.*, 2005). During this stage alluvial fans and deltas formed in association with the developed drainage networks.

Closer to the study area, other works show evidences for precipitation and fluvial runoff later in Martian history. Late Hesperian dendritic channels were identified in the Vallis Marineris area (Mangold *et al.*, 2004). In the Southwest Thaumasia region, stratigraphic relations suggest a Hesperian age for a complete assemblage of valleys, paleolakes and deltas (Mangold and Ansan, 2006). The same authors analyzed the valley networks in Warrego Valles (southern Thaumasia Highlands) and concluded that hydrological activity in the region span the Noachian-Late Hesperian interval (Ansan and Mangold, 2006).

The global or local origins for those periods of later wet conditions are still motive of debate, since hydrothermal activity or cratering can locally create transient surface runoff conditions, even if at a global scale a colder and dryer climate existed (Fassett and Head III, 2008).

Sapping valleys are a different type of valleys, and they are usually related with groundwater seepage and mass wasting processes (Howard, 1988; Lamb *et al.*, 2006). The U-shaped cross section and characteristic amphitheatre valley heads are some of the key features that allow the recognition of those features.

4.3.1 Surface runoff and sapping

During the lineament classification process a large number of valley scarps were recognized (Figure 4.23). Valley networks were mainly mapped along the Coprates and Thaumasia bulges while valley head scarps appear mainly associated with some of the valleys mapped in the dissected rims of a large tilted crater located North of Bosporos Planun.

As previously mentioned, other types of scarps present signs of erosion. The normal faults that cross the Coprates/Thaumasia arch constitute the best examples of those types of scarps. It could be argued that in those cases, surface water runoff may not be the best mechanism to explain those morphologies, but water driven erosion may still be implied in the erosion and dissection of those tectonic features. For this reason those eroded structures are included in the following analysis. Another indicator of the close relation between the tectonic structures and the drainage networks are the fault aligned, rectilinear channels that characterize much of the Protva Valles and Coprates Rise drainage patterns.

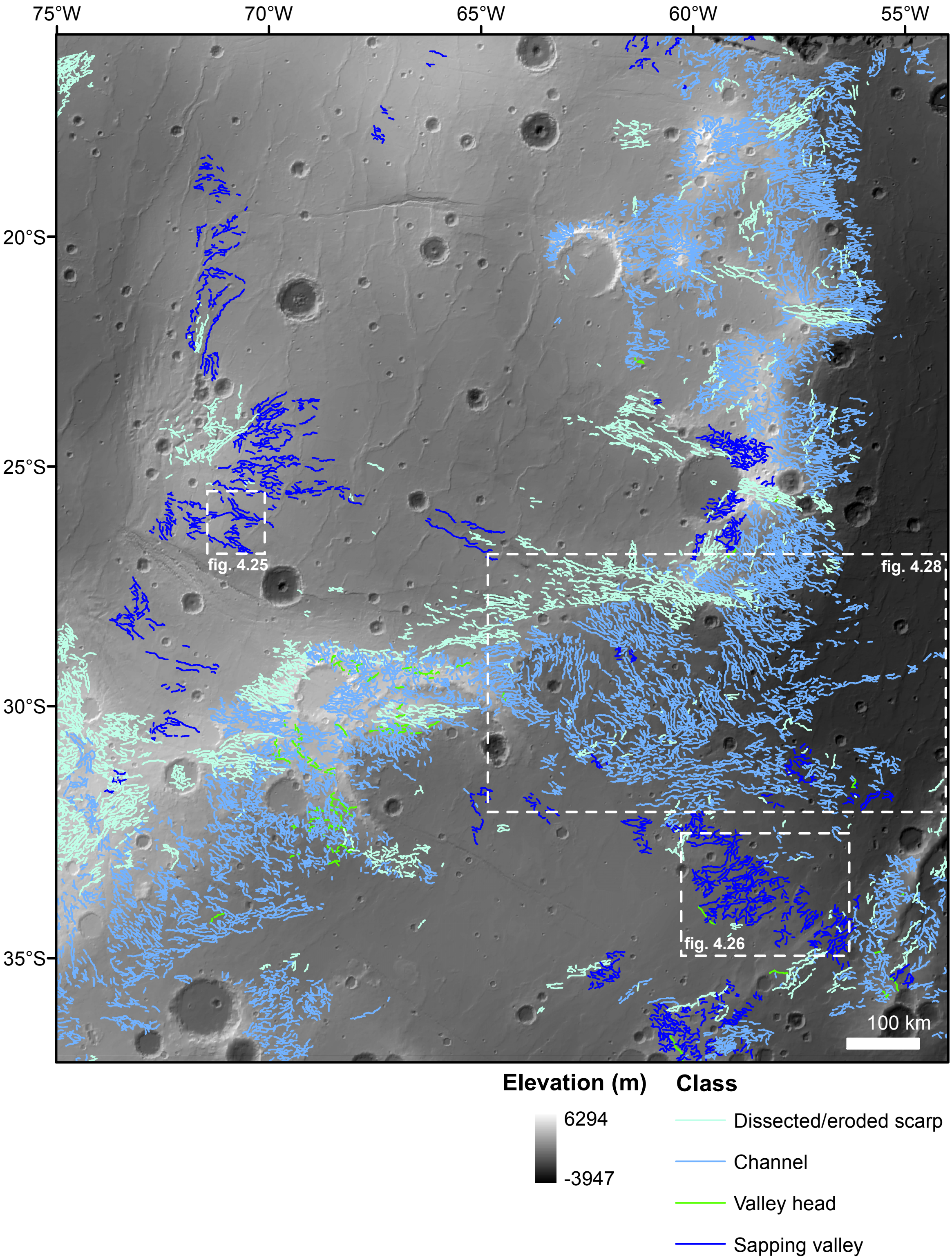

Figure 4.23 – Mapped scarps where water flow, sapping or high degree of erosion is evident.

The paleoerosional map of the Thaumasia region (Dohm *et al.*, 2001c) presents a much lower number of channels than the Figure 4.23 map. In previous works three stages of valley incision were distinguished in the study area (Dohm and Tanaka, 1999;

Dohm *et al.*, 2001c). A Noachian stage (stage 1) corresponds to the valleys that dissect the highlands craters rims, the volcanic edifices and the higher sections of the East flank of the Coprates Rise. The channels located in the Ogygis Rupes area were also considered as stage 1 features. Resurfacing has probably affected those channels, since they generally form discontinuous patches (Dohm and Tanaka, 1999). What the present mapping reveals is that a higher continuity exists, since channels and signs of erosion were found to be continuous along the full extent of the Coprates/Thaumasia arch.

The second stage channels (Noachian-Hesperian) constitute the majority of the channels in the Protva Valles region and in the highlands that encircle Bosporos Planum (dissecting the *HNpld* and *HNplt* units, see Figure 4.3). The erosive structures in the *HNplt* unit (that dissect the Protva Valles main escarpment) present a different morphology and they locally form irregular depressions. Those different morphologies have been linked with possible fracture-induced hydrologic circulation and hydrothermal activity (Dohm and Tanaka, 1999). Note that those erosive structures were formed in a unit that covers the East ending of the already mentioned Melas Fosse/Protva Valles dextral transtensive rift system. This makes likely credible that the valleys in the Protva Valles region formed in association with a high secondary permeability associated with the fractures identified more to the west.

A third set of Hesperian valleys (stage 3) were identified in the Southeast edge of the Coprates Rise and dissect the *Hpld* unit. Some of these channels cut wrinkle ridges (Dohm *et al.*, 2001c).

The automatic mapping and careful lineament classification using high resolution imagery allowed the identification of numerous valleys more akin with sapping valley morphologies. Wider valleys, generally ending at an amphitheater shaped valley head were mapped in the large Northeast facing escarpment located between Protva Valles and Ogygis Rupes. A previously uncharted group of sapping valleys was identified west of Martin crater. This set is the continuation of the sapping valleys located more to South (constituting the *HNt* terraced material unit). Those two groups formed in the Eastern flank of Melas Dorsa.

4.3.2 Longitudinal vectors - flow paths

The analysis of the longitudinal valley profiles is a commonly used technique to segment river systems, essentially by delimiting sections of the channels where slope breaks occur and studying the shape of the profiles (Knighton, 1998; Rădoane *et al.*, 2003).

Starting from the lineament database, a longitudinal slope vector for each scarp was computed. To make the technique more reliable, the vectors were not computed between the edges of the scarps. Instead, the scarp lineaments were divided in two equal segments, and a 3D centroid was computed for each segment. The slope and dip direction of the longitudinal vector is computed from those points, which makes the resulting vectors less sensitive to MOLA data gaps. It should be noted the need to use geodetic measurements of azimuths and distances during the computation of the vectors, which makes the methodology independent of the type of map projection of the original data.

If sedimentation, cratering or tectonic activity did not change the longitudinal profile of the valleys, the computed vectors are excellent ways for evaluating the directions of paleoflow, since the vectors dip direction should approximate the direction of water surface runoff. A local inversion of those "paleoflow" vectors azimuths should be regarded as indicative of a later perturbation of the drainage networks by tectonics or other processes.

This methodology was also applied to all the mapped scarps that present signs of water related activity, such as degraded scarps and sapping valleys (to all the scarps drawn in Figure 4.23). Since water surface runoff is not probably responsible for the formation of those structures, the longitudinal vectors still give indication of the regional longitudinal slope, which is especially relevant in the case of the sapping valleys.

Figure 4.24 shows the longitudinal slopes for the mapped scarps. The higher slopes (>1.5º) correlate well with the stage 1 valley networks mapped by Dohm *et al.* (2001c). Those areas correspond to the rims of the dissected craters, to the dissected volcanic edifices, to the Coprates Rise East flank and to the Ogygis Rupes lobate scarps. Those results show that the stratigraphic and more qualitative hierarchization of the drainage networks proposed by Dohm *et al.* (2001c) reflect indeed a morphologic measurable parameter. This may in the future contribute to an automatic recognition and segmentation of this specific kind of stage 1 valleys in broader areas.

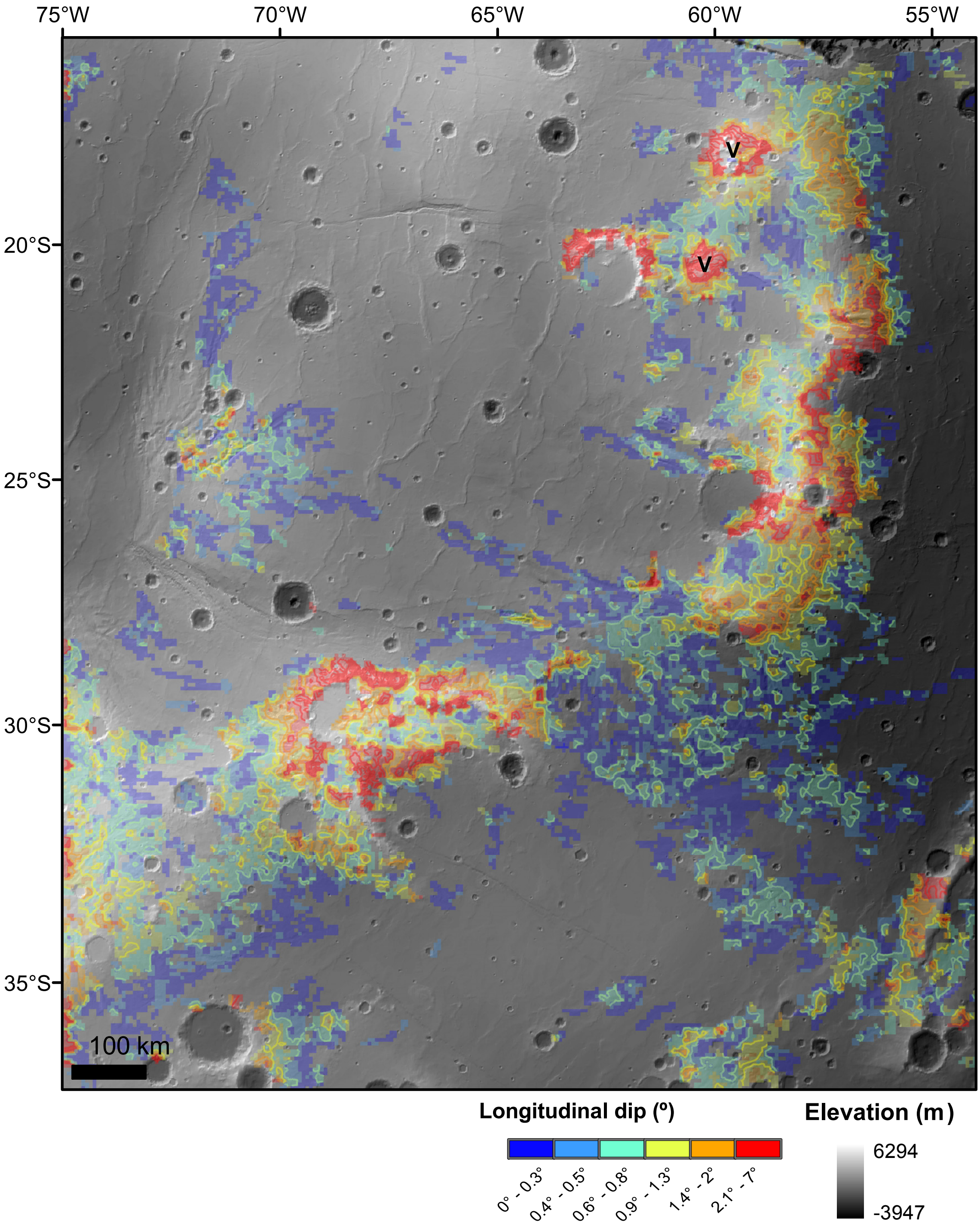

Figure 4.24 – Longitudinal slope angles measured for the scarps shown in Figure 4.23. Higher dips are associated with: crater rims located on the Noachian cratered highlands, with the two volcanoes (V) that present dissected flanks and with the tectonic features in Ogygis Rupes (SE corner of analyzed area). Those are basically the same locations of the stage 1 valleys mapped by Dohm *et al.* (2001c).

In map view, stage 2 and 3 valleys, as well as the sapping valleys, present lower slopes (<1.5º). It is obvious that the slopes tend to decrease with elevation.

Two examples that illustrate well the potentialities of the proposed method are shown in Figure 4.25 and Figure 4.26. In both cases, sapping valleys were analyzed. In the first map the impact of tectonic activity is shown. The formation of a wrinkle ridge induced a decrease in the longitudinal slope of the sapping valley nearby that tectonic structure. Some of the vectors even show the inversion of the longitudinal dipping direction (see the vectors pointed by the black arrow in Figure 4.25b).

Figure 4.26 illustrates a different setting. In that region tectonic activity may have caused a lateral variation of the slope values. Observe that the slopes are higher in the Southeast corner of the area, and decrease toward the Northwest border of the analyzed region. The flow trajectories seem to have suffered a rearrangement nearby the two NE-SW trending wrinkle ridges. This suggests that the formation of the sapping valleys in this area may have occurred at the same time of the wrinkle ridges development. This makes plausible that the tectonic activity in the region may have facilitated the aquifer disruption and the formation of the sapping valleys.

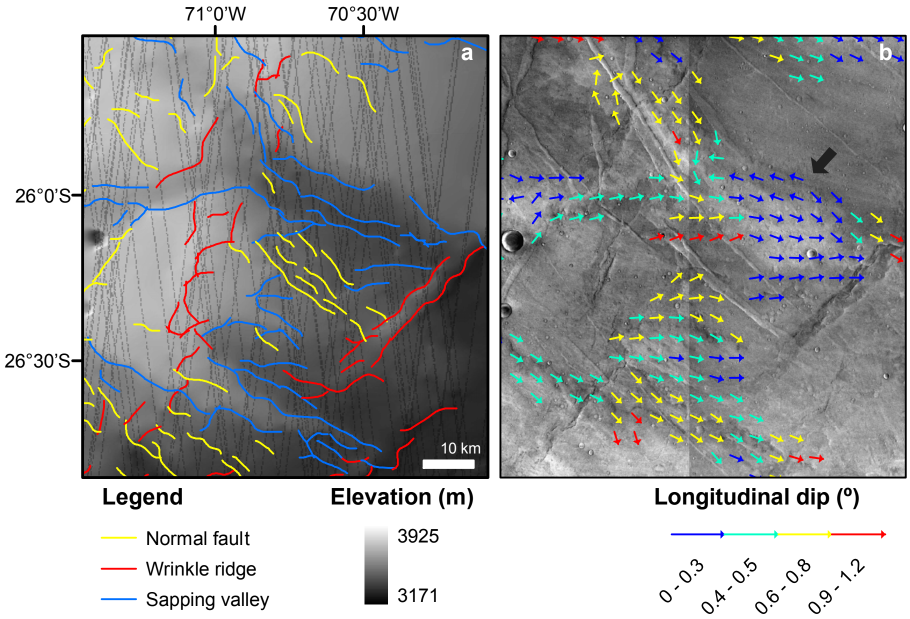

Figure 4.25 – Sapping valleys near Melas Fossae (see Figure 4.23 for location). (a) Mapped scarps overlaid on MOLA (MOLA tracks are also shown); (b) HRSC images. At least two incision levels are visible. Wrinkle ridge postdate the wide sapping structures and normal faults cut the wrinkle ridges; (b) valley scarp longitudinal vectors, note the lower slopes and contrasting dip direction near the black arrow, a clear indicator of the effect of deformation in the sapping valleys network.

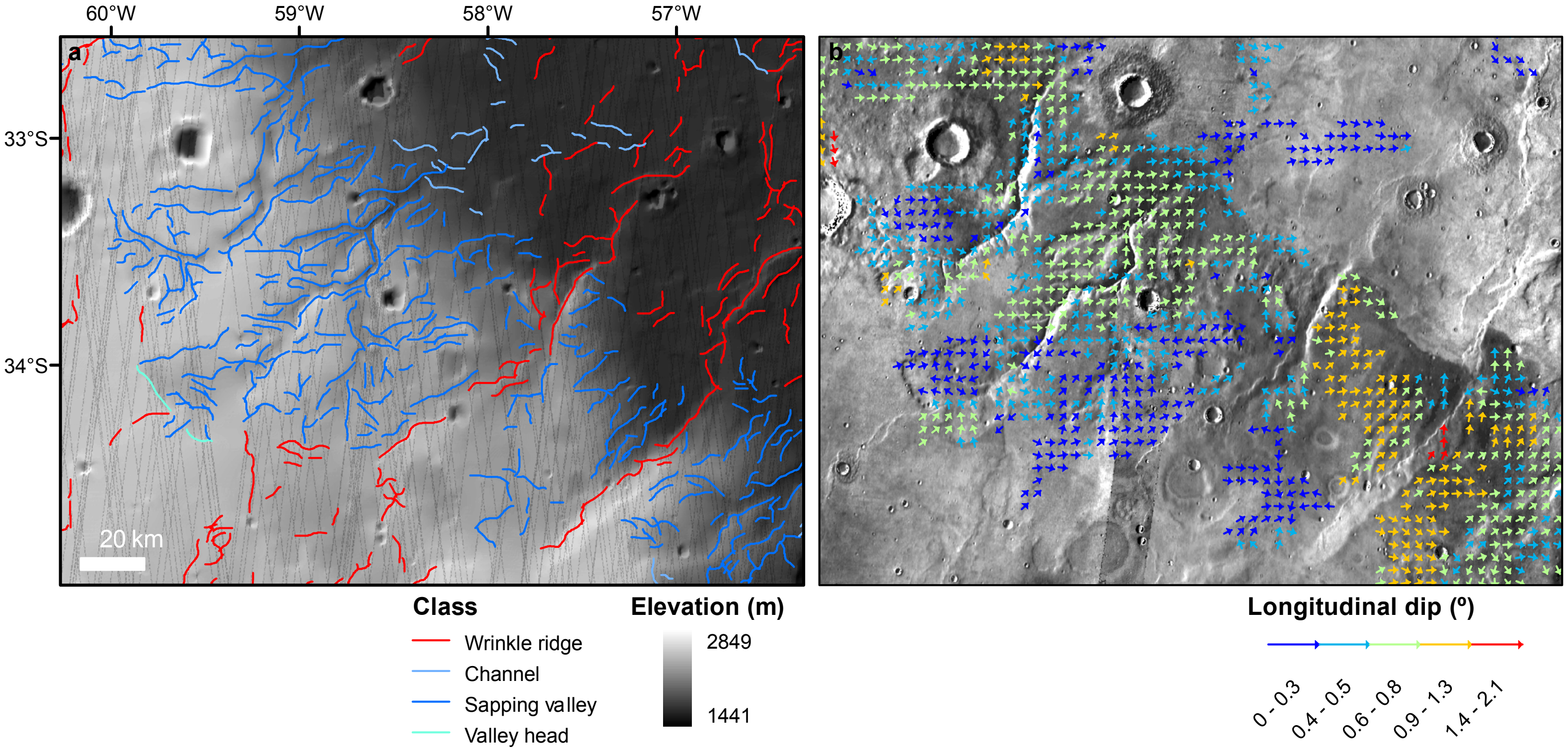

Figure 4.26 – Example of the application of the introduced morphometric methodology to the East Bosphoros Planum sapping channels (refer to Figure 4.23 for location). (a) Mapped sapping valleys overlaid on MOLA altimetry; note the amphitheatre shaped valley heads in some of the upper section of the valleys. Wrinkle ridges seem to control some of the channel in the SE corner of the displayed region. (b) Channel longitudinal dip vectors sampled at a 4 km grid. The impact of the two main compressive structures located in the SE portion of the area is evident in this case: higher longitudinal slopes as well as a rearrangement of the vectors dip direction more to the East indicate that in this area tectonic activity may be connected with the sapping process. In the central and NW zones sapping seems to postdate some of the wrinkle ridges.

Contrary to the other channels, whose longitudinal dip angles decrease with a decrease in elevation, the slopes of the depicted sapping valleys seem to increase as moving down on the regional escarpment. When the sapping valleys reach the lowland plains, slopes abruptly decrease.

This means that a morphometric difference was found between the normal valley networks and the sapping valleys. River channels on our planet also normally present an upward concave longitudinal profile (exponential, logarithmic and power functions are normally used to model channel longitudinal profiles, Knighton, 1998). The sapping valleys slopes, which correspond to an upward convex longitudinal profile, could reflect the different processes that formed those morphologic features (sapping and mass wasting processes instead of water surface runoff).

Is that pattern recognizable in other sapping valleys on Mars, or is it just a local characteristic? Have the local geology and stratigraphic setting influenced the described morphologies? These are some of the questions that remain to be answered. This different longitudinal slope signature, if confirmed in other areas, would be considered as diagnostic of sapping processes.

4.3.2.1 Regional drainage paths

The introduced methodology and the type of map view analysis it enables were already briefly explored in the previous section. To get a larger scale perspective of the surface drainage patterns a vectorial analysis technique widely used in structural and tectonic studies is used.

The longitudinal vectors were computed independently for each scarp class shown in Figure 4.23. Next, the slope and dip direction of the vectors were projected in equal area stereographic plots, and density contours were generated. Since the measured slope values are low, slope values were truncated at 2º and stretched to fit the range 0-90º. This means that in the obtained stereographic plot, a 90º dip correspond to a 2º slope value of the longitudinal valley profile (see the graphical scale in Figure 4.27a).

The already mentioned bimodality of slopes associated with channel networks is perfectly visible in the Figure 4.27a plot. Two modes are visible for dipping angles of 0.3º and 1.9º. This last mode is most likely underestimated since angles larger than 2º were truncated. This diagram confirms the interpretation made previously, of the existence of a higher dipping channel set (stage 1 channels) and of a lower dipping subpopulation (stages 2 and 3). The flow azimuths are mainly centered in the N60-140ºE interval, but a weaker reverse sense flow direction is also visible (N240-310ºE). Those channel longitudinal profile vectors could be easily correlated with the formation of the ~N-S to ~NE-SW large bulges that form the Coprates Rise and Thaumasia Highlands. The preserved channel networks are, in this case, clearly controlled by large scale topography.

Figure 4.27b stereographic diagram shows that sapping valleys only present low sloped longitudinal profiles (all the modes present a 0.3° dip angle). Higher vector dispersion exists for those features, and main directional modes trend N80ºE and N110ºE. Those modes make part of a main interval comprised between N45ºE and N135ºE. An opposite sense of longitudinal dip is in this case stronger, and a N280ºE trend is more evident. The analysis of the sapping valleys in Melas Dorsa (Figure 4.25) revealed that tectonic processes may locally invert the sense of longitudinal dip. This means, that at least partially, the third mode can be attributed to this fact.

The eroded scarps present a major vector trend in the interval N270-300ºE and dipping 0.3° (Figure 4.27c). The East dipping longitudinal vectors are more dispersed and the dip angles present a higher variation. Nevertheless, they seem to be comprised in the N45-120ºE interval. This type of scarps also presents a subpopulation with higher dip angles. It is more difficult to interpret those results, but they agree with the preferential location of those eroded scarps in the West-Northwest dipping flank of the Coprates Rise/Thaumasia Highlands arch (Figure 4.23).

The projection of the totality of the water carved/eroded structures gives a much more regular view of the overall regional "paleoflow" pattern (Figure 4.27d). The dip angle bimodality is still present for the East quadrant dipping vectors (N45-135ºE). A secondary mode with lower slopes is present with approximately the opposite dipping sense (N250-315ºE).

The asymmetry between the number of East and West dipping vectors is much stronger in the case of the channels longitudinal vectors. Since the channels are the only mapped structures that directly require precipitation, and assuming that at a regional scale a geologic or tectonic influence can be neglected, this asymmetry can be considered as indicative of paleoclimatic asymmetries possibly caused by the large topographic bulges.

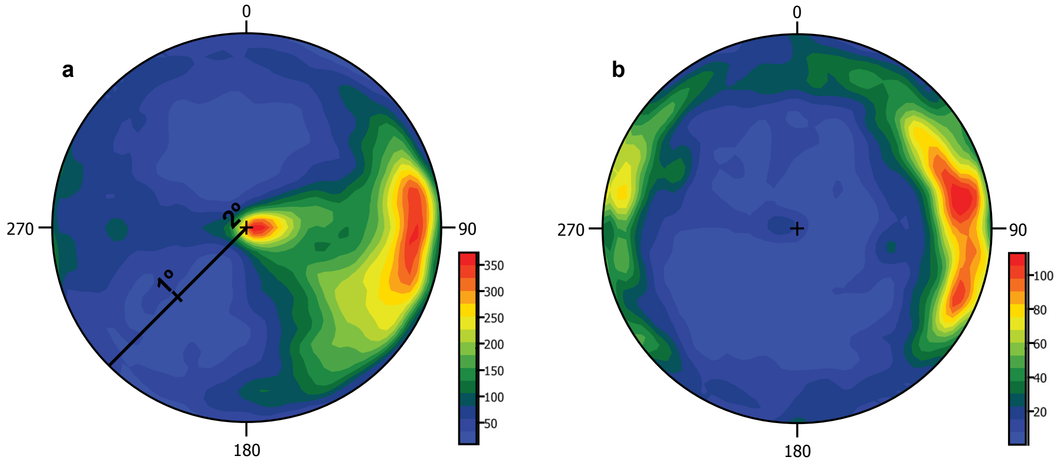

Channels **Sapping valleys**

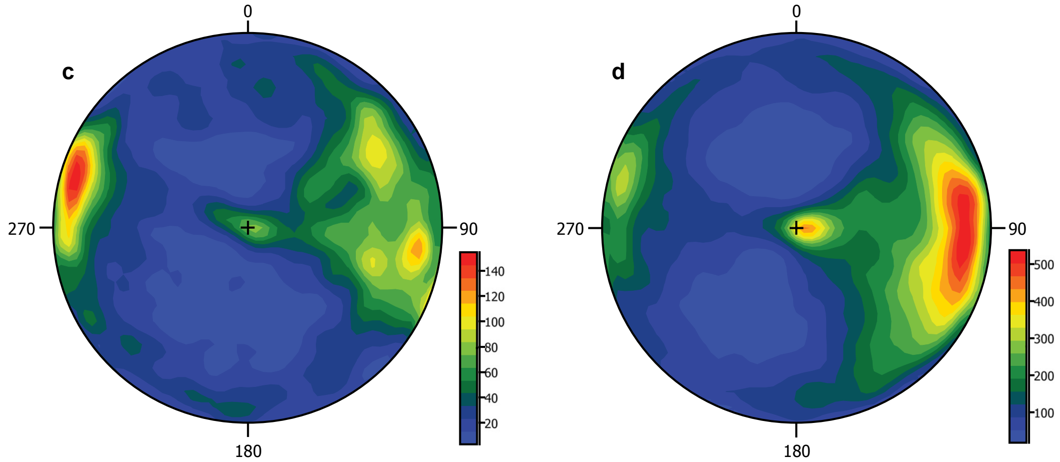

Eroded scarps **All scarps**

Figure 4.27 – Equal area (Wulff net) lower hemisphere stereographic projection of the longitudinal dip vectors that dip less than 2º. Due to the low measured dips, values were truncated and stretched to fit the range 0-90º (see the graphic scale in (a)). Vectors were plotted for each class in Figure 4.23 (a) stereographic projection of the channel longitudinal vectors; (b) stereographic projection of the sapping valleys longitudinal vectors; (c) stereographic projection of the eroded/dissected scarps vectors; (d) stereographic projection of the totality of the vectors in (a-c). Two main trends are evident, one set striking 240º-310º and the other 60º-140º. Dips are concentrated around two values: 0.3º and 1.9º (since values were truncated to <= 2º this higher dip mode may be superior, dips >2º are generally associated with scarp rims, see map in Figure 4.24). Sapping valleys are always low dipping while the other two classes of features have the two sets of dips well represented. Channels mainly dip to the East quadrant while eroded/dissected scarps present a higher concentration of vectors that dip to the West quadrant.

4.3.3 Provda Valles drainage system

After the presented regional analysis, it was decided to analyze in more detail the Protva Valles region, a region that offers the possibility to study Hesperian hydrological activity. Besides the already described analysis, made using the scarps extracted from the MOLA data, it was necessary to go further, and use CTX imagery. For this purpose a CTX mosaic with a spatial resolution of 6 m/pixel was created to analyze a more restricted area. A classic fotoinpretation was then performed.

The main objective was to better constrain the cross-cutting relationships between the tectonic structures and the channel systems. Due to the MOLA coarse resolution those relations are not resolvable. This is particularly well evidenced in the lineament map of Figure 4.28a. Channels and wrinkle ridges coexist in the same units, but the spatial resolution is not enough to discriminate the cross-cutting relations. Yet, the computed longitudinal dip vectors for the channels scarps are still very useful (Figure 4.28b).

Note an increase in the dip angles after the channels cross the NW-SE hogback structures (zone I), a clear sign of structural control during the carving of those channels. Locally, the vectors seem to converge to the area marked as zone II, which may be indicative of the existence of a body of standing water in the past.

Another good example of channel tectonic longitudinal dip inversion is observable in the area pointed with a black arrow (Figure 4.28b). Observe how the vectors suffer an inversion in the zones located between the wrinkle ridges. This is already indicative that in that region wrinkle ridge formation postdate the channel formation. This area belongs to the Early Hesperian younger ridged plains unit (*Hr*) (Dohm *et al.*, 2001a), which gives a lower bound for this channel formation stage.

The analysis of the CTX image mosaic reveal a much more complicated set of structures, and cross-cutting relationships point to a more complex joint evolution of the wrinkle ridges and channels. The area analyzed in more detail (Figure 4.29) corresponds to a transition zone between the *Hr* unit and the *Hpld* unit (also of Early Hesperian age).

A new class of channels only observable at finer scales was recognized. They are interpreted as inverted channels that form small ridges. This morphology tends to appear in lower elevations, while small channels still presenting a negative topography were preserved in higher terrains (compare the spatial distribution of S1 channel/lineations with the S1 inverted channels in Figure 4.29a). This implies an important regional resurfacing episode after the Noachian.

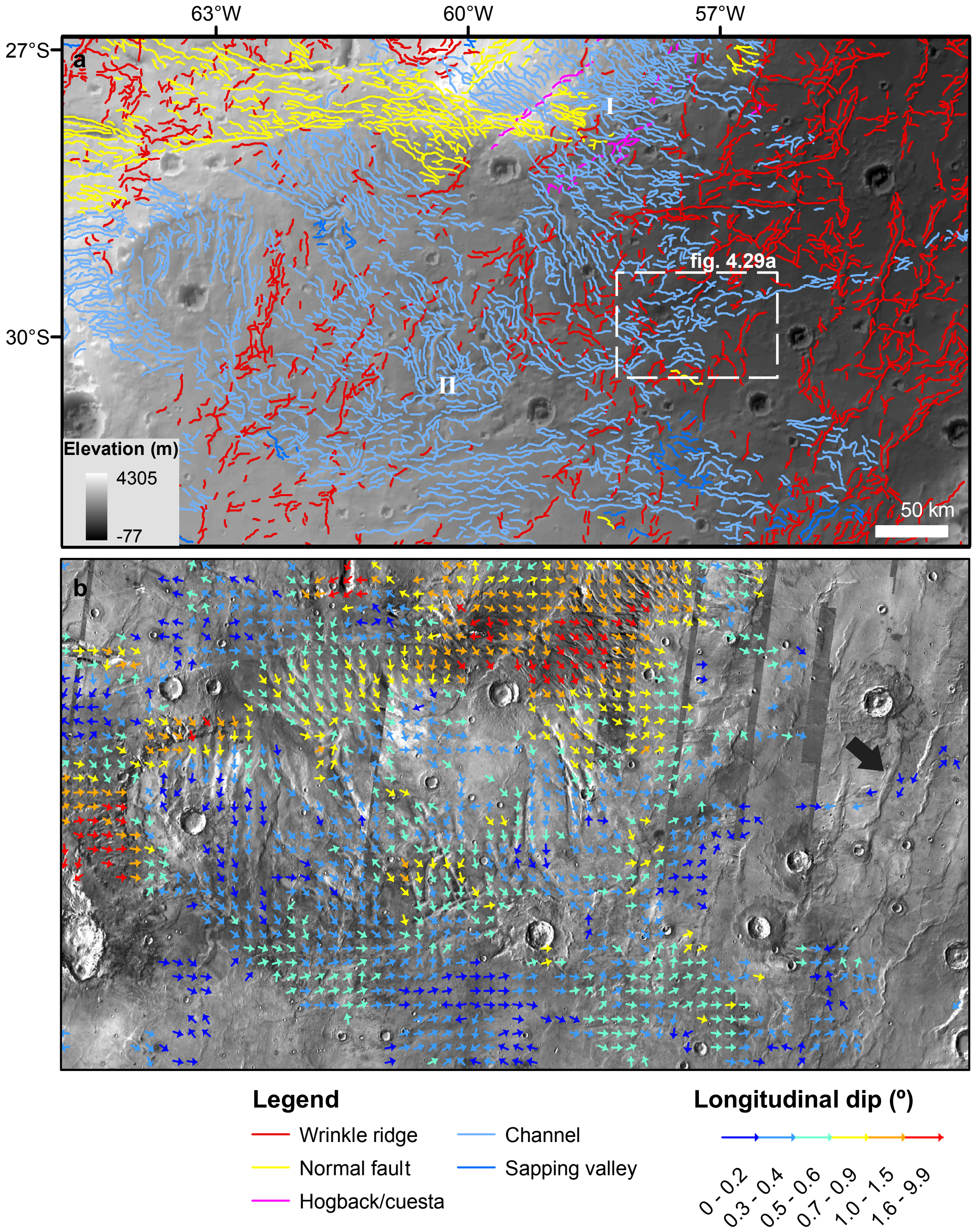

Figure 4.28 – Protva Valles mapped structures. (a) mapped scarps; (b) channel longitudinal dip vectors sampled at a 4 km grid; regional flow direction toward SE dominates the NW part of the shown area, passing to a more E-W trend reaching the ridged lowlands. Dip angles are higher in the Coprates Rise. Note the inversion of the apparent flow direction (black arrow) associated with wrinkle ridge formation in the ridged lowlands. See text for discussion.

In map view, the referred channels are discontinuous and usually present a low sinuosity. Their narrow width and low sinuosity suggest a low energetic environment.

The cross-cutting relations for the S1 structures are clear: they are cut by all the younger channels as well as by all the wrinkle ridges (see how the inverted channels appear superimposed on the wrinkle ridges in Figure 4.29d). Examples of inverted channels were already identified on Mars (Marzo *et al.*, 2009). In the present case they are interpreted as belonging to an ancient setting of surface runoff, named S1 phase. Those channels do not always follow the actual topographic gradient, see for example the S1 channels in the smooth North-dipping surface labeled as zone I (Figure 4.29a). Despite the North-dipping regional slope, the channels present an East-West trend, parallel to the present day elevation contour lines.

A second phase of aqueous surface runoff (S2) is characterized by larger and more sinuous channels. In the central part of the analyzed region, the main wide channel shows a braided morphology (Figure 4.29c) where channel bars are still perceptible.

The development of braided river systems is thought to be dependent on several conditions: abundant sediment supply that will be mobilized as bed load, erodible banks, discharge variability and steep valley slopes (Knighton, 1998). Those conditions are usually meet in proglacial areas and in the transition of mountainous to plains regions.

An obvious parallelism between those general conditions and the regional setting of the analyzed region can be established (see the regional setting of the analyzed region in Figure 4.28). Channels with higher profile slope descend and dissect the Protva Valles and Coprates Rise highland regions. The resurfacing event that produced the inversion of the S1 channels confirms that erodible banks are also a likely condition in the region.

When the channels reach the lowlands their profile slope decreases, which matches the observation of braided stream systems in that transition area.

Braided morphologies do not indubitably indicate a long and persistent water runoff phase. Braided channel morphologies are also characteristic of desert wadi channels, which do not have a continuous surface water runoff, but are usually formed due to desert flash floods events (Glennie, 1970).

Those ephemeral discharge channels are sometimes associated with alluvial fans and perennial lakes (Gaber *et al.*, 2009). In the analyzed region four small fan-like structures were mapped in the termination of some of the braided S2 channels. The position of those fans coincides with the location of two large quasi-circular depressions, probable subdued craters. Those depressions are interpreted as possible paleolakes. The putative paleoshores of the lakes were defined by the local recognition of escarpments and erosive surfaces from imagery. As can be seen, the mapped paleoshores do not perfectly correspond to an equipotential topographic surface. This is more evident in the case of the larger mapped lake. For this lake, three fans are located between the 950 m and 1000 m elevation contour lines. This is perhaps the best indication that the mapped erosional shorelines were overestimated. Alternatively, the fans can mark a lower water level in the lake.

The existence of a fourth alluvial fan located between the two lakes (Figure 4.29c) implies the overflow and connection of the two lakes.

Both lake depressions are located between wrinkle ridges, which suggests that the tectonic activity controlled the location of those paleolakes. The fact that the paleoshores follow and, in some cases, dissect the wrinkle ridges (Figure 4.29c), proves that the lake emplacement was made after or during wrinkle ridge formation. This is consistent with the S2 channels, which also cut the majority of the wrinkle ridges (Figure 4.29d). Note however, that some of the wrinkle ridges are not cut by all the S2 channels. Observe the NE-SW trending wrinkle ridge in Figure 4.29b, see how in some cases it cuts the S2 channels while in others it is cut by them (the smaller channel in northern part of the image). This observation, and the referred longitudinal channel dip inversion measured in the westward continuation of this channel system indicate that tectonic activity persisted locally, during and after the S2 channel formation.

In summary, the detailed mapping allowed the identification of two distinct phases of water runoff. The first phase is older than the wrinkle ridge formation (older than Early Hesperian). It is tempting to correlate those channels with the high-sloped Noachian drainage networks of the highlands. In this scenario the S1 channels would correspond to the floodplain counterparts of those highlands channels. The second phase is characterized by the formation of alluvial fans, two lakes and braided channels in a more energetic hydrological regime, but probably in a more arid climate. Between those phases a regional resurfacing event is needed to justify the inverted nature of some of the S1 channels. It was shown that the S2 channels postdate the majority of the wrinkle ridges in the area, but with some exceptions, which indicate that tectonic activity persisted at least until after the formation of part of the S2 channels.

The given preliminary analysis of the area represented in Figure 4.29 needs to be further developed, nevertheless it attests the existence of Hesperian water runoff in the Protva Valles area. In agreement with the same conclusions obtained for other areas of the Thaumasia Highlands (Ansan and Mangold, 2006; Mangold and Ansan, 2006), constituting one more argument in favor of a wetter Hesperian period.

4.4 Magnetic and gravity anomalies

After the analysis of the surface morphologies that are present in the East Thaumasia region, the gravity and magnetic anomalies will be briefly examined. Both datasets are presented in 1ºx1º map bins.

Gravity free-air anomalies from the shperical harmonic model MGM1025 model (Lemoine et al., 2001) obtained from Mars Global Surveyor tracking data is shown in Figure 4.30a. Valles Marineris shows a strong negative anomaly (only a part of this band with negative values is visible in the NE corner of the study area) that correlates well with the axial trough topography (Anderson and Grimm, 1998; Smith *et al.*, 1999; Zuber *et al.*, 2000). This negative anomaly corresponds to the mass deficit resultant from the through formation.

The Valles Marineris through is bordered by high positive anomalies, which correspond to the lithospheric flexural response to the mass deficit induced by the Valles Marineris formation (Smith *et al.*, 1999; Dohm *et al.*, 2009). This anomaly is patent in the study area, and corresponds to the higher positive anomalies (>150 mGal) located in the E-W trending band parallel to Valles Marineris.

Besides that anomaly, the Coprates Rise/Thaumasia Highlands arch signature is perfectly evident in the anomaly map. A positive anomaly follows the highland arch, which agrees with an excess of mass due to the large scale lithospheric buckling/thrusting. Note how the Melas Fossae/Protva Valles dextral transfer zone disrupts the arch positive anomaly.

The lowlands located East and Southeast of the arch are characterized by a strong negative anomaly parallel to the arch. Anguita *et al.* (2006) compared this anomaly with the negative signature of foreland basins in Earth orogenic provinces. The detailed analysis of the East Protva Valles hydrological record fully support this view, since a long-lived depositional basin has proved to have been active until Hesperian times. Observe how the strongest negative anomalies (~100 mGal) are located in that same area, marking perhaps a basin depocenter.

Mars currently does not possess an active internal magnetic field. The shown magnetic anomalies in Figure 4.30b correspond to the radial component of the crustal remanent anomalies derived from the MAG-ER (Mars Global Surveyor Magnetometer/Electron reflectometer) data measured at a ~400 km altitude (Connerney *et al.*, 2005). This radial component is less sensitive to the influence of ionospheric field contamination, giving a more reliable insight on the crustal anomalies (Connerney *et al.*, 2005; Johnson and Phillips, 2005).

At a global scale, magnetic anomalies are arranged in parallel approximately E-W bands with alternating field polarities. The lack of magnetization in some of the larger impact structures such as Hellas, Utopia, Argyre, Isidis and Chryse, tells us that the internal dynamo was only active very early in Mars history (prior to Early Noachian, ~4.1 Ga, Lillis *et al.*, 2008).

Anomalies are much stronger in the Southern cratered highlands, while in the Northern plains they are much weaker. This weaker magnetic signature is considered to be a product of Hesperian and Amazonian mantling of older subdued cratered crust in the Northern lowlands (Frey *et al.*, 2002; Connerney *et al.*, 2005).

Another key global characteristic of the magnetic Mars signature, is the absence of magnetization associated with the major volcano-tectonic provinces. Thermal erasure of the Early Noachian anomalies in those areas is generally invoked to explain that lack of magnetization (Johnson and Phillips, 2005).

In the study area, higher magnetizations are limited to the outer regions of the Coprates Rise/Thaumasia Highlands arch (Figure 4.30b). Anomalies fade away in the Thaumasia Planum region and in the Melas Dorsa values are already below the used threshold value (0.3 nT/deg). The association with the Syria Planum volcanic province, and the interpretation of the *HNr* unit as vulcano-sedimentar in origin, may justify the anomalies cancellation in the region.

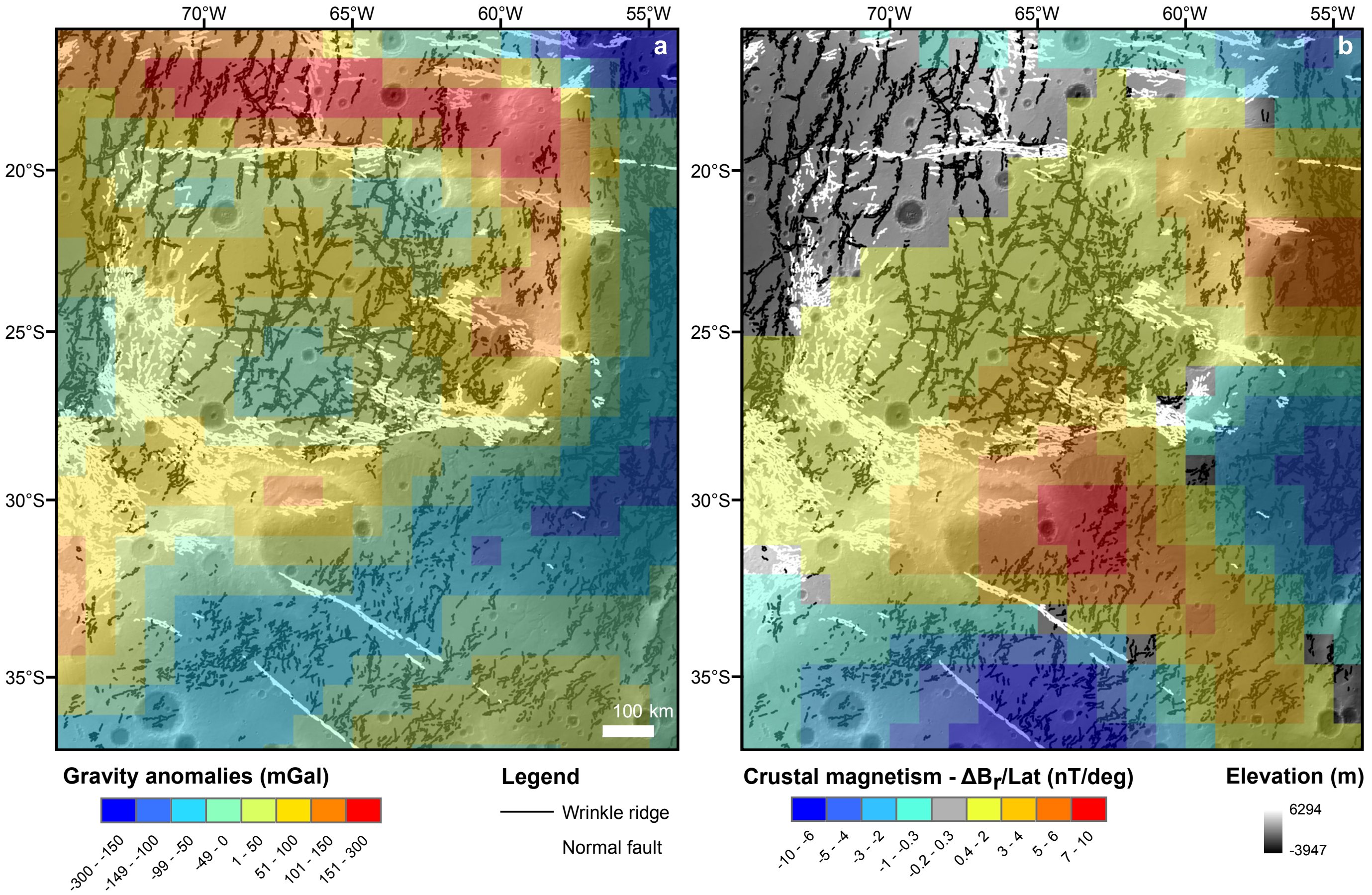

Figure 4.30 – Gravity anomalies and radial component of the crustal magnetism for the East Thaumasia region; (a) gravity anomalies from MGM1025 model (Lemoine et al., 2001); (b) radial component of the crustal magnetism derived from MAG-ER (Mars Global Surveyor Magnetometer/Electron reflectometer) data (Connerney et al., 2005). The same 0.3 nT/deg treshold used by Connerney et al. (2005) was applied to symbolize non magnetized regions.

As stated, the global scale band geometry is the most remarkable characteristic of the Martian crustal magnetic record. Yet, the reasons for this spatial arrangement of the anomalies are not fully understood, but several explanations have been advanced:

- a seafloor spreading-like mechanism was proposed to have formed the anomalies in a context of global magnetic field reversals (Connerney *et al.*, 2001; Connerney *et al.*, 2005)
- another explanation that implies a plate tectonics regime early in Mars history was proposed by Fairén *et al.*(2002); they argue that terrain accretion in a convergent plate margin may be responsible for the formation of the large bands with alternating polarities
- other explanations do not involve a plate tectonic regime early in Mars evolution; a magnetic monopolarity shell may have formed during the time the internal dynamo was active, later reworking and disruption of that monopolarity shell would produce the bands (Sprenke and Baker, 2000); cratering, volcanism, hydrothermal and tectonic activity are some of the potential processes that would contribute to the band formation
- dike emplacement was also invoked (Nimmo, 2000)
- more recently, band formation has been linked with a possible mechanism of lithospheric drift over hot-spots, that would be responsible for partial remagnetization of the crust (Kobayashi and Sprenke, 2010).

Such a great variety of possible mechanism for the formation of the anomalies difficults the interpretation of the anomaly pattern in the study area, mainly because a unique source mechanism cannot be established. Because of this, only a conjectural association of the anomalies with the mapped surface structures can be performed.

The anomalies in the Tharsis area that occur in post-Noachan terrains were interpret to be originated by the Noachian basement that underlie those younger terrains (Johnson and Phillips, 2005). The bands located in the East border of the Coprates Rise/Thaumasia Highlands arch seem to be radial to the arch. It can be further pointed, that the positive anomalies seem to be aligned with some of the main tectonic structures previously analyzed, the North Thaumasia rift, and the Melas Fossae/Protva Valles transfer zone. In this last case, the positive anomaly band better fits the surface expression of the large NW-SE escarpment that goes from Protva Valles to the Ogygis

Rupes area (the same area characterized in Figure 4.26), marking the limit between the Bosporos Planum and the lowlands located in front of the Coprates Rise buldge. Since the arch in this zone is sub-parallel to the Argyre rims, the same escarpment (as well as the anomaly), is also radial to the Argyre impact basin. For the escarpment, it is easier to accept that it could be inherited from the impact itself (other Argyre radial and concentric large scale morphological features are present around the basin, see Figure 4.1 map), but for the positive anomaly it is not obvious the reason for this spatial association.

The discussed radial nature and spatial association of the anomalies with the main tectonic structures that transect the Coprates Rise/Thaumasia Highlands arch, can be better integrated if it is assumed that the anomaly bands formed due to the disruption of a planet-wide monopolarity shell (as proposed by Sprenke and Baker, 2000). In the study area, hydrothermal and tectonic activity as well as the Argyre impact may have contributed to that disruption.

This possible association must be tested in other areas, and perhaps only a global survey will prove this potential association. Nevertheless, the physical mechanism that would link the positive polarities with the more intensely fractured zones is still not clear.

4.5 Evolutionary synthesis

In this section a summary evolutionary synthesis will be presented. This synthesis will incorporate the observations made during the dissertation and will try to include in a logic succession of events the complex surface morphologies mapped and characterized in the previous chapters.

The Argyre impact basin formed during Early Noachian times (Hiesinger and Head III, 2002). The Argyre basin is a multiring impact basin presenting a radial and concentric fracture pattern formed far away from the impact region (Figure 4.31a). Some of the concentric fractures were later reactivated as thrust faults forming, among others, the Ogygis Rupes lobate scarps. The Midde-Late Noachian reactivation of impact radial fractures may have contributed to the formation of the Protva Valles/Ogygis Rupes NE dipping escarpment, which as seen is a major boundary that segments different styles and intensities of deformation. The current topography, with a depressed region in the North suggests that this structure may have been reactivated as a normal fault, while the formation of the Coprates Rise bulge may have induced a dextral shear component. This possible dextral component is also supported by the segmentation and offset of the Ogygis Rupes lobate scarps in the SE corner of the mapped area (Figure 4.31b).

The formation of the Thaumasia Highlands/Coprates Rise arch may have begun in the Early Noachian, probably as a more continuous structure. Middle-Late Noachian times correspond to a stage of great activity in the study area. The uprise of the Thaumasia Highlands/Coprates Rise arch was followed by an intense hydrologic activity nowadays best represented in the highlands. Sedimentation starts to be focused in the lowlands formed due to the large scale buckling. Two volcanic edifices formed, possibly linked with some of the fractures that transect the Coprates Rise.

The Melas Fossae/Protva Valles dextral transfer structure formed, and lead to the differentiation of two provinces presenting different styles of deformation. The analysis of the structures located in the front of the arch suggests that the Melas Fossae/Protva Valles transfer system is a major structure that separates a section of the arch more probably associated with a thrusting structure (the Coprates Rise), while buckling is perhaps the only mechanism responsible for the formation of the arch section located immediately South of the transfer zone.

As noted before, lithospheric buckling is responsible for the occurrence of several tilted eroded crater rims. The two craters located west of Protva Valles may have contributed for the localization and development of the Melas Fossae/Protva Valles transfer zone.

The Melas Dorsa folding may have been also initiated during this period, but it was during the Late Noachian-Early Hesperian that the folding peaked, with the formation of the fold axial grabens. The fold hinge plunges to the North, interacting with a similar, but more incipient, buckle structure located more to the East, Felis Dorsa. As previously mentioned, the flank asymmetry that characterizes Melas Dorsa may be indicative of an East dipping fold/thrust structure.

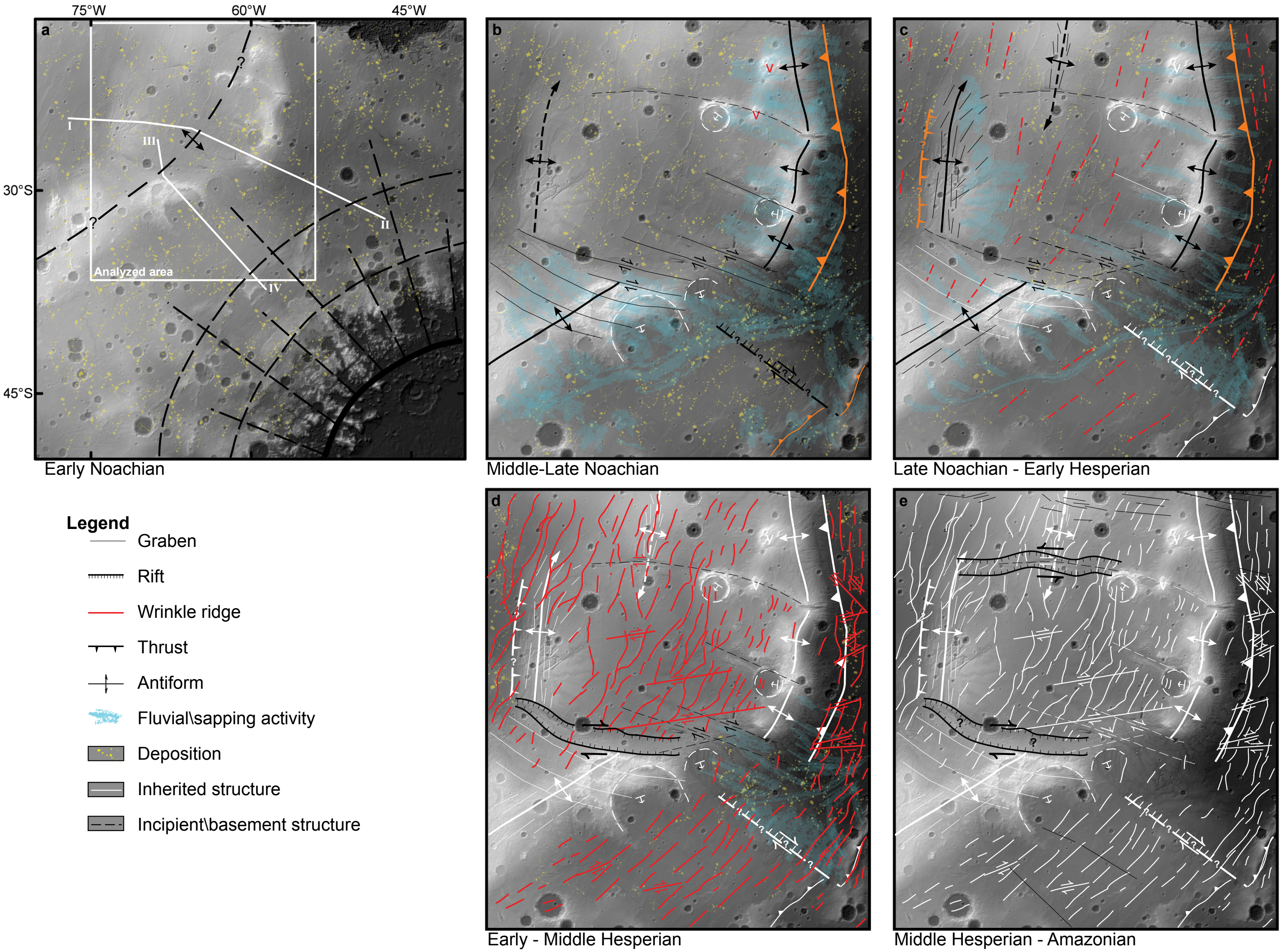

Early Noachian

Middle-Late Noachian

Late Noachian - Early Hesperian

Early - Middle Hesperian

Middle Hesperian - Amazonian

Figure 4.31 – Evolutionary synthesis for the Thaumasia Planum region. See text for discussion. See next figure for the <style face='normal' font='default' size='100%'>Directional Statistics</style></title></titles><pages><st

The tectonic activity responsible for the buckling/thrusting in Melas Fossae was also responsible for aquifer disruption and formation of sapping valleys, especially in the Eastern flank of this large scale fold. Hydrologic activity decreased and deposition of materials focused even more in the intermountain plains. The *HNr* unit was emplaced during this period embaying the older Noachian terrains.

South of Melas Fossae buckling continued, while fold hinge extension formed grabens parallel to the buckle axis. The buckle/thrust front of the Coprates Rise continued active during this stage, with the Melas Fossae/Protva Valles transfer zone being responsible for this differential structural behavior.

The need to locally invoke more than one episode of wrinkle ridge formation has already been emphasized. It is obvious that wrinkle ridge formation peaked after the emplacement of the *HNr* unit, but Figure 4.31c portrays the possibility that wrinkle ridge formation may have locally started during the *HNr* unit emplacement.

Early-Middle Hesperian tectonic activity was characterized by a thin-skinned deformation regime in the plain units (Figure 4.31d). The large scale buckles/thrusts become progressively inactive, and wrinkle ridges formed as the surface manifestation of basement *décollements*. Conjugated transpressive wrench faults formed coevally with the pure compressive structures East of Coprates Rise and in the Thaumasia Planum regions.

During this stage the Melas Fossae/Protva Valles transfer zone, which was partially covered by the emplacement of the *HNr* unit, was reactivated, which lead to the development of the oblique rift structure of Melas Fossae. The rifting style was controlled by the previously formed dextral basement structures.

Hydrologic activity during this period was concentrated in the Protva Valles region. Sapping and hydrothermal activity may have contributed to the formation of the younger valleys in this area, in an increasingly dry environment. Deposition during this stage seems to be restricted to the outer regions of the belt (west of Melas Dorsa and east of Coprates rise).

After the main phase of wrinkle ridge formation (Early-Middle Hesperian) the North Thaumasia Planum rift formed (Figure 4.31e). As described in chapter 2, this rift corresponds to an array of sinistral pull-apart basins that were probably formed due to the reactivation of an older basement structure. It is not clear if the Melas Fossae rift was still active at the time of formation of the North Thaumasia rift. However if that is the case, the Thaumasia Minor plate, as outlined by Montgomery *et al.* (2009), may have suffered an anticlockwise rotation, since the sinistral transtensive regime in the North may have been contemporary with the dextral transtension in the Melas Fossae region.

During that period, two sets of narrow grabens cut all the formed structures in the Bosporos Planum region. A mechanism of post-orogenic gravitational spreading was invoked by Anguita *et al.* (2006) to explain this type of later structures. In the Northern edge of the mapped area, Valles Marineris parallel faulting developed probably in response to the trough formation.

Figure 4.31 illustrates the proposed evolutionary stages. From one stage to the next, inherited structures are represented in white. The presented evolutionary scheme does not intend to strictly restrict the activity of a certain structure to a given time interval. The aim of the chosen symbology is to show how some of the structures were active, in some cases were reactivated, or have influenced the following stages.

The presented analysis points to a long-lasting tectonic evolution forming a great variety of structures, driven by an almost constant remote σ_1. Table 4.5 summarizes the several horizontal principal stress directions derived from the analysis of several types of tectonic structures.

As shown in Figure 4.19, the circular distribution of shortenings is bimodal. North of Melas Fossae shortening vectors strike ~N107ºE while in the Bosporos Planum a ~N160ºE was measured. Excluding the wrinkle ridges located in the Bosporos Planum, all the remaining structures are compatible with a σ_1 comprised between N100-120ºE. It can be concluded that the mapped tectonic structures located North of the Melas Fossae/Protva Valles transfer zone developed in a regional σ_1 striking ~N110ºE, while South of the transfer zone the regional σ_1 trended ~N160ºE. This does not mean two different tectonic phases (separated in time), but shows the local rotation of the σ_1 trends, justified by the activity of the dextral transfer structure that segments two distinct provinces. All the mentioned stress markers are small scale tectonic structures. However, the large scale buckles are locally perpendicular to those same trends, showing the coupled evolution of all the tectonic structures.

The analysis of this small fraction of the Thaumasia Highlands/Coprates Rise arch is not self-elucidative about the physical mechanism causative of the stresses which created the mapped tectonic structures. What can be concluded is that the σ_1 in the region are centered in Tharsis, making great circles that cross the Syria Planum/Noctis Labyrinthus region as well as the Tharsis Montes region. In the presented analysis it was sustained that the different convergence vectors are not product of different remote stresses, but are better interpreted and integrated as local re-orientations of the stress field.

Table 4.5 – This table summarizes the σ_1 azimuths obtained from the analysis of different stress markers mapped in the East Thaumasia region.

Stress marker	σ_1 azimuth
NFs strike	~117º
Melas Dorsa NFs strike	~105º
NFs extension	108.9º
Pure WRs strike	106º
Oblique WRs bisector angle	102.5º
WRs shortening (north of Melas Fossae)	~107º
WRs shortening (south of Melas Fossae)	~160º
WRs shortening (total)	111.5º

Tharsis lithospheric membrane/flexural loading models obtained from the integration of present day topography and gravity predict for the analyzed region a principal stress trajectory trending approximately N120ºE (Banerdt *et al.*, 1982; Banerdt and Golombek, 2000; Golombek and Phillips, 2010). Another model that integrates topography and crustal thickness, and that models stress fields induced by horizontal gradients of the gravitational potential energy give for the East Thaumasia region a more E-W aligned σ_1 (Dimitrova *et al.*, 2006). Both regional stress trajectories can be considered to be consistent with the stress trajectories locally inferred from the mentioned stress markers (Table 4.5). This strongly suggests that despite the higher degree of structural complexity that the present work revealed, the formation of all the structures may still be a product of Tharsis mass loading induced stresses.

The presented evolutionary scheme is generally inline with the idea of a Noachian-Hesperian orogeny along the Thaumasia Highlands/Coprates Rise as proposed by other authors (Anguita *et al.*, 2001; Webb and Head, 2002; Anguita *et al.*, 2006). During Noachian times, a thick-skinned tectonic regime probably involving the entire lithosphere would have been the prevailing tectonic style. With the erosion of the high-standing relieves, plain units formed over a fractured basement on inter-mountainous depressions. The basin located east of Coprates Rise resembles Earth foreland basins (as previously pointed by Anguita *et al.*, 2006). Those basins in our planet occur in front of contractional belts due to the flexural response induced by the orogenic load (DeCelles and Giles, 1996; Singh, 2003). A characteristic of this kind of basins is the existence of a forebulge depozone that corresponds to a flexural uplift of the basement. In Figure 4.32a an uplifted region is visible in the lowlands east of Coprates Rise (this uplifted region is labeled FB?). This region is located outside the area mapped in detail, which makes that this possible forebulge zone must be better analyzed in future works.

As argued throughout this chapter, the Melas Fossae/Protva Valles transfer zone is a major tectonic structure that separates two different sectors of the Thaumasia Highlands/Coprates Rise arch. Figure 4.32a show an interpretative sketch of the lithospheric structure north of the transfer zone, while in Figure 4.32b a interpretative sketch is given for a cross section that pass over Melas Fossae and transect the Thaumasia Highlands. Since subsurface structures and depths were inferred, the elevation axis scale was not provided. At depth, a basement isoline (dotted line) was drawn, in order to represent the style of deformation in the two sectors. The more superficial plain units are sketched, as well as the inferred blind structures responsible for the wrinkle ridges at the surface.

A major thrust is probably concealed by the younger plain materials located east of Coprates Rise; a tectonic wedge is hypothesized to exist in this area. As pointed before, the asymmetric morphology of Melas Dorsa may be indicative of a blind thrust beneath the bulge. The possible double vergence of the fold-thrust belt in that region suggests a more advanced degree of convergence for the North sector.

Bivergence is commonly associated with mature collisional orogens in our planet (Persson, 2001). It is tempting to compare the proposed structural setting for the region located north of the Melas Fossae/Protva Valles transfer zone with a pop-up wedge. Indeed, Anguita *et al.* (2006) compared the Thaumasia block structure with the southeastern sector of the Eurasian Plate.

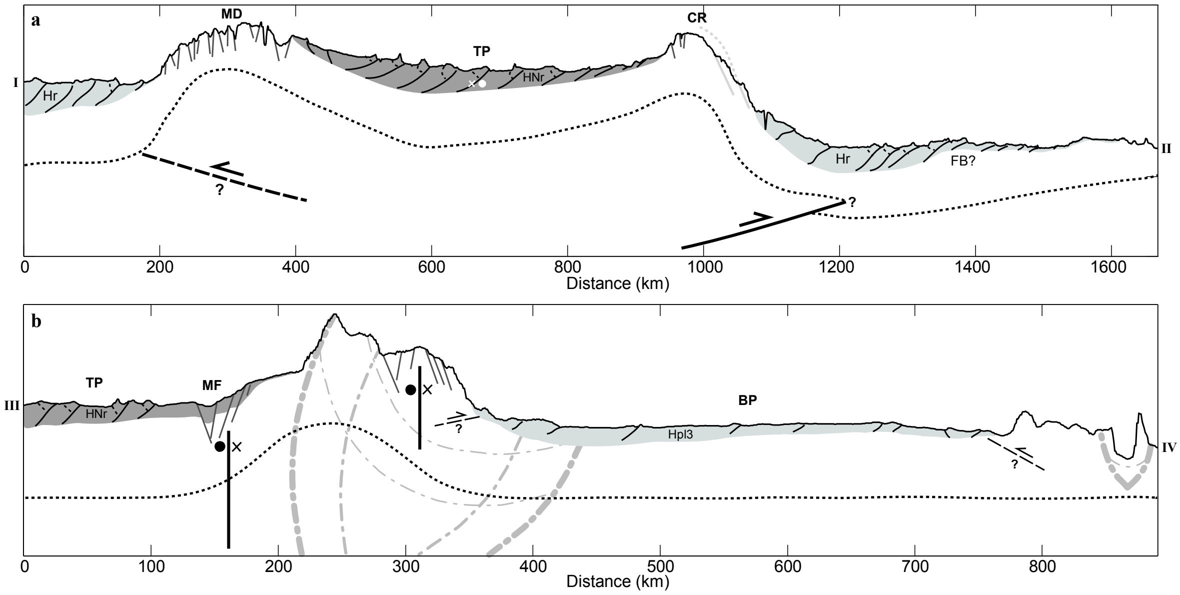

Figure 4.32 – Interpretative cross sections (see Figure 4.31a for section location); only the more superficial units were drawn (for example, bellow the *Hr* unit an older unit with the same age of the *HNr* unit is expected to be present); the doted line drawn at depth correspond to the interpreted strains accommodated by the basement unit; MD – Melas Dorsa, CR – Coprates Rise, TP – Thaumasia Planum, MF – Melas Fossae, BP – Bosporos Planum; (a) an immature bivergent orogenic belt is proposed to explain the surface morphologies observed in the sector located North of Melas Fossae; (b) south of Melas Fossae a major thrust system is probably not present and crater tilting is probably product of buckling, the dextral shear sense associated with Melas Fossae is also shown.

The incipient development of the main thrusts, the quasi undisrupted geometry of the main bulges and the large basin existent between Melas Dorsa and Coprates Rise are some of the arguments that difficult a comparison of the North sector with Earth orogenic belts. Furthermore, wrinkle ridges located in front of Coprates Rise, despite displaying a more complex arrangement (recall the transpressive nature of some of those structures), are still very different from the much more complex imbricated foreland compressive structures formed in the outer areas of collisional belts (such as in the Zagros frontal fold-thrust belt (McQuarrie, 2004)).

The structure and morphologies of the sector located north of Melas Fossae are more easily correlated with an early phase of an orogenic process. Thus, the architecture of the North sector is in some aspects similar to Earth colisional belts, but the apparent simple organization and comparatively small strains point instead to an early/embryonic stage of orogenic evolution.

South of Melas Fossae an even more initial stage seems to be represented. The bulge is dominated by a large tilted impact crater. The presented strain analysis of the foreland region of this section suggested that the region suffered a less intense strain. These arguments support the idea that a major thrust structure is not present in this section of the bulge, which was probably formed only due to buckling. The more distinctive characteristic of this zone is the dextral transtensive kinematics that increases when approaching the Melas Fossae region.

A new perspective on the formation and segmentation of the large-scale compressive structures that forms the Eastern border the Thaumasia Plateau was given. A full analysis of the remaining Thaumasia Highlands using the set of tools presented in this dissertation can help in the future to favor one of the possible mechanisms already proposed for the formation of the Thaumasia Highlands/Coprates Rise arch.

4.6 Conclusion

The major contribute of this chapter is the better description and morphometric characterization of the surface morphologies of the East Thaumasia region. This characterization helped to establish a more precise along-arch segmentation of part of the Thaumasia Highlands/Coprates Rise belt.

The introduced mapping procedure was applied and new tools were used to estimate the amount of compressive strain associated with wrinkle ridges and to analyze the hydrologic activity in the region. Those constitute examples of new morphometric analytical tools that can be developed from the base automatic lineament mapping procedure.

The close relation between the hydrologic and tectonic activities was examined. The hydrological flows inferred from the channel scarps followed the regional pathways created by the large scale buckles. In the Protva Valles region, hydrological activity spanned until Hesperian times, with the development of a braided river system with lakes and alluvial fans.

A more detailed evolutionary model for the region was proposed. Unlike previous models, the performed analysis revealed that all the tectonic structures are compatible with a unique long-lasting regional event. This event was not necessarily continuous in time, since different sets of structures formed sequentially. But, perhaps a common origin for the causative stresses can be favored, since through time the regional stress trends did not change considerably.

Earth collisional orogens presenting double vergence are possible good analogues for the structural setting of the region located north of the Melas Fossae/Protva Valles transfer zone. This transfer zone is a first order structure that separates a more mature sector in the North of a more undeveloped compressive structure in the South. The general structure in both areas is nevertheless more akin to an initial stage of orogenic evolution.

5 Concluding remarks

The introduced set of new methodologies proved to be a very promising tool to analyze not only the tectonic structures, but on a broader sense the geology and geomorphology of Mars surface. The introduced lineament mapping framework allows a thematic morphometric analysis having as fundamental structure the notion of scarp. Throughout the present work several practical examples of possible applications of this generic morphometric scarp characterization method were given.

The chosen test area which corresponds to the Eastern border of the Thaumasia Plateau, was used to compare and evaluate qualitatively and quantitatively the proposed lineament mapping procedure. This comparison reinforces the need for an objective lineament mapping procedure, since significant differences were found in the comparison of two human-mapped lineament datasets. The lineament map obtained semi-automatically proved to be more complete, despite its dependence in data quality and resolution.

Even if the tectonics of the selected area is perhaps one of the most intensely studied on Mars, the new introduced tools allowed the recognition and characterization of new types of tectonic structures. A good example of this was obtained through the mapping and strain analysis performed for the North Thaumasia Planum rift. A new style of deformation was identified for this area, interpreted as a rift formed by several pull-apart basins denoting a regional left-lateral shear component.

In chapter 4 an integrated analysis of all the mapped scarps in the East Thaumasia Plateau border was performed. Distensive and compressive structures and strains were analyzed and the need for accounting with transtensive and transpressive regimes was stressed.

The surface hydrologic activity was briefly analyzed, revealing the interplay between tectonics and hydrological activity in the region. The Protva Valles area was analyzed in more detail, showing a long history of water surface runoff, with a distinct Hesperian phase of activity characterized by braided channel morphologies and lakes formed during and after wrinkle ridge development in the area.

Finally, a more detailed evolutionary synthesis was presented. This synthesis highlights the importance of the Melas Fossae/Protva Valles transfer zone, which segments two different sectors of the Thaumasia Highlands/Coprates Rise arch. North of the transfer zone, a collisional double vergent orogen was hypothesized, while in the South, a simpler buckling structure lacking a major thrust was favored. The analyzed section of the Thaumasia Plateau is interpreted as representing an early stage of collisional orogenesis.

6 Further work

It was constantly recognized along the present work that some of the proposed methodologies can still be improved. From a technical point of view, the proposed methodology to estimate normal faults extension should in the future incorporate a variable fault dip angle. Measuring the slope of the scarps is not enough since those ancient scarps were eroded, which will force the use of some kind of scarp degradation model.

A larger margin for future developments exists for the wrinkle ridge strain estimation technique. The estimation of shortenings beyond the spatial resolution of the used altimetric data constitutes one of the main challenges.

Beyond the applicability to paleotectonic studies, the brief hydrologic characterization demonstrated how the lineament database, with its unique morphometric characterization capabilities, can be used to study other geomorphologic structures on Mars. Other applications will be sought.

In terms of datasets, the mapping results can certainly be improved with a better spatial resolution and data quality. Data fusion techniques as the one advanced by Lin *et al.* (2010) are promising techniques that will improve the quality of Mars elevation data.

If a better spatial resolution is needed to better analyze and characterize small scale structures, a global analysis using coarser resolutions will allow a quick lineament mapping at a global scale. This mapping will produce an intractable amount of lineaments, which will certainly justify the implementation of automatic classification methods. Another alternative is to make the scarp classification a cooperative effort, by providing the global lineament database to the planetary science community which will be encouraged to share their scarp classification results.

Paleotectonic characterization of other planets and moons can surely take advantage of the same lineament mapping procedure. Even if quality elevation data is not available, the proposed methodology can easily be adapted to analyze other types of gridded datasets such as imagery or radar data. In our planet, regions with low deposition and erosive rates are particularly suited to the application of the developed methodologies. Ocean floors and desertic tectonized regions constitute some of the regions were the developed methodologies can be easily applied.

The task of lineament mapping is transversal to others remote sensing studies. An example of the adaptation of some of the presented techniques to other domains, is for example the automatic mapping and characterization of ripple migration on Mars dunes (Silvestro *et al.*, 2010; Silvestro *et al.*, 2010).

In the last chapter, the analysis of the East Thaumasia region raised several questions that should be addressed in future works. Only a small portion of Tharsis volcano-tectonic province was mapped and analyzed in this work. The application of the developed tools to the mapping and characterization of the entire province can, in a near future, contribute to the better comprehension of the geologic and tectonic evolution of Mars. The mapping and strain characterization of the remaining Thaumasia Plateau Highlands is a priority, since it may help to clarify the mechanism behind the complex Thaumasia Plateau tectonic evolution.

7 References

Abramov, O.,McEwen, A., 2004. An evaluation of interpolation methods for Mars Orbiter Laser Altimeter (MOLA) data. Int. J. Rem. Sens. Vol. 25, Number 3, 669-676.

Acuña, M.H., Connerney, J.E.P., Ness, N.F., Lin, R.P., Mitchell, D., Carlson, C.W., McFadden, J., Anderson, K.A., Rème, H., Mazelle, C., Vignes, D., Wasilewski, P.,Cloutier, P., 1999. Global distribution of crustal magnetization discovered by the Mars Global Surveyor MAG/ER experiment. Science 284, 790-793.

Aksoy, E., Inceoz, M.,Koçyigit, A., 2007. Lake Hazar Basin: A Negative Flower Structure on the East Anatolian Fault System (EAFS), SE Turkey. Turk. J. Earth Sci. 16, 319-338.

Alves, E.I., Barata, M.T., Vaz, D.A., Pereira, L.C.G., Baptista, A.R.,Chorro, M.J., 2008. Martian Tectonics, Water and Life. In: L.A. Costas (Editor), Planet Mars Research Focus. Nova Science Publishers.

Anderson, E.M., 1951. The dynamics of faulting and dyke formation with applications to Britain. 2nd ed. Oliver and Boyd, Edinburgh, 206 pp.

Anderson, R.C., Dohm, J.M., Golombek, M.P., Haldemann, A.F.C., Franklin, B.J., Tanaka, K.L., Lias, J.,Peer, B., 2001. Primary centers and secondary concentrations of tectonic activity through time in the western hemisphere of Mars. J. Geophys. Res. 106(E9), 20563-20586.

Anderson, R.C., Dohm, J.M., Haldemann, A.F.C., Pounders, E., Golombek, M.,Castano, A., 2008. Centers of tectonic activity in the eastern hemisphere of Mars. Icarus 195(2), 537.

Anderson, S.,Grimm, R.E., 1998. Rift processes at the Valles Marineris, Mars: Constraints from gravity on necking and rate-dependent strength evolution. J. Geophys. Res. 103(E5), 11113.

Anguita, F., Farelo, A.-F., López, V., Mas, C., Muñoz-Espadas, M.-J., Márquez, A.,Ruiz, J., 2001. Tharsis dome, Mars: New evidence for Noachian-Hesperian thick-skin and Amazonian thin-skin tectonics. J. Geophys. Res. 106(E4), 7577-7590.

Anguita, F., Fernández, C., Cordero, G., Carrasquilla, S., Anguita, J., Núnez, A., Rodríguez, S.,García, J., 2006. Evidences for a Noachian-Hesperian orogeny in Mars. Icarus 185, 331-357.

Ansan, V.,Mangold, N., 2006. New observations of Warrego Valles, Mars: Evidence for precipitation and surface runoff. Planet. Space Sci. 54(3), 219.

Antoine, J., Barache, D., Cesar Jr., R.,Costa, L., 1996. Multiscale shape analysis using the continuous wavelet transform, Proceedings of IEEE ICIP'06, pp. 101-105.

Argialas, D.P.,Mavrantza, O.D., 2004. Comparison of edge detection and hough transform techniques for the extraction of geologic features. Int. Arch. Photogram. Rem. Sens. Spatial Inform. Sci. 34, Part XXX.

Armijo, R., Meyer, B., Navarro, S., King, G.,A., B., 2002. Asymmetric slip partitioning in the Sea of Marmara pull-apart: a clue to propagation processes of the North Anatolian Fault? Terra Nova 14(2), 80-86.

Bandeira, L., Saraiva, J.,Pina, P., 2007. Impact crater recognition on Mars based on a probability volume created by template matching. IEEE Trans. Geosc. Rem. Sens. 45(12), 4008-4015.

Banerdt, W.B.,Golombek, M.P., 2000. Tectonics of the Tharsis Region of Mars: Insights from MGS Topography and Gravity, Lunar and Planet. Sci. Conf., XXXI, abstract 2038, Houston.

Banerdt, W.B., Phillips, R.J., Sleep, N.H.,Saunders, R.S., 1982. Thick shell tectonics on one-plate planets: applications to Mars. J. Geophys. Res. 87(B12), 9723-9733.

Barka, A., Akyüz, H.S., Cohen, H.A.,Watchorn, F., 2000. Tectonic evolution of the Niksar and Tasova-Erbaa pull-apart basins, North Anatolian Fault Zone: their significance for the motion of the Anatolian block. Tectonophysics 322(3-4), 243-264.

Bibring, J.P., Langevin, Y., Mustard, J.F., Poulet, F., Arvidson, R., Gendrin, A., Gondet, B., Mangold, N., Pinet, P., Forget, F.,team, O., 2006. Global mineralogical and aqueous mars history derived from OMEGA/Mars express data. Science 312(5772), 400-404.

Bistacchia, N., Massironia, M.,Baggio, P., 2004. Large-scale fault kinematic analysis in Noctis Labyrinthus (Mars). Planet. Space Sci. 52(1-3), 215-222.

Bobillo-Ares, N.C., Bastida, F.,Aller, J., 2000. On tangential longitudinal strain folding. Tectonophysics 319(1), 53.

Borraccini, F., Di Achille, G., Ori, G.G.,Wezel, F.C., 2007. Tectonic evolution of the eastern margin of the Thaumasia Plateau (Mars) as inferred from detailed structural mapping and analysis. J. Geophys. Res. 112(E05005).

Borraccini, F., Lanci, L., Wezel, F.C.,Baioni, D., 2005. Crustal extension in the Ceraunius Fossae, northern Tharsis region, Mars. J. Geophys. Res. 110, EO6006.

Brew, G., Lupa, J., Barazangi, M., Sawaf, T., Al-Iman, A.,Zaza, T., 2001. Structure and tectonic development of the Ghab basin and the Dead Sea fault system, Syria. J. Geol. Soc. London 158(4), 665-674.

Bue, B.D.,Stepinski, T.F., 2006. Automated classification of landforms on Mars. Comput. Geosci. 32(5), 604-614.

Bue, B.D.,Stepinski, T.F., 2007. Machine Detection of Martian Impact Craters From Digital Topography Data. IEEE Trans. Geosc. Rem. Sens. 45 (1), 265-274.

Carr, M.H., 2006. The surface of Mars. Cambridge University Press, New York, 307 pp.

Chen, S., Zhou, X., Tang, L., Wang, Y., Lü, D., Sun, M.,Qu, D., 2010. Wrench-related folding: A case study of Bohai Sea basin, China. Mar. Petrol. Geol. 27(1), 179.

Clifton, A.E.,Schlische, R.W., 2003. Fracture populations on the Reykjanes Peninsula, Iceland: Comparison with experimental clay models of oblique rifting. J. Geophys. Res. 108 (B2), 2074.

Colton, S.L., Smart, K.J.,Ferrill, D.A., 2006. Wrinkle ridge detachement depth and undetected shortening at Solis Planum, Mars, Lunar and Planet. Sci. Conf. XXXVII, abstract 1729, League City.

Connerney, J.E.P., Acuna, M.H., Ness, N.F., Kletetschka, G., Mitchell, D.L., Lin, R.P.,Reme, H., 2005. Tectonic implications of Mars crustal magnetism. PNAS 102(42), 14970-14975.

Connerney, J.E.P., Acuña, M.H., Wasilewski, P.J., Kletetschka, G., Ness, N.F., Rème, H., Lin, R.P.,Mitchell, D.L., 2001. The global magnetic field of Mars and implications for crustal evolution. Geophys. Res. Lett. 28(21), 4015-4018.

Davis, G.H.,Reynolds, S.J., 1996. Structural Geology of Rocks and Regions. Wiley, 800 pp.

DeCelles, P.G.,Giles, K.A., 1996. Foreland basin systems. Basin Research 8(2), 105.

Di Achille, G.,Hynek, B.M., 2010. Ancient ocean on Mars supported by global distribution of deltas and valleys. Nature Geoscience 3(7), 459-463.

Dimitrova, L.L., Holt, W.E., Haines, A.J.,Schultz, R.A., 2006. Toward understanding the history and mechanisms of Martian faulting: The contribution of gravitational potential energy. Geophys. Res. Lett. 33(8), L08202.

Dohm, J.M.,Tanaka, K.L., 1999. Geology of the Thaumasia region, Mars: plateau development, valley origins, and magmatic evolution. Planet. Space Sci. 47(3-4), 411-431.

Dohm, J.M., Tanaka, K.L.,Hare, T.M., 2001a. Geologic map of the Thaumasia Region, Mars. In: s. Geologic Investigation Series I-2650 (Editor), Atlas of Mars: Thaumasia Region. U.S. Geological Survey.

Dohm, J.M., Tanaka, K.L.,Hare, T.M., 2001b. Paleotectonic Map of the Thaumasia Region, Mars. In: s. Geologic Investigation Series I-2650 (Editor), Atlas of Mars: Thaumasia Region. U.S. Geological Survey.

Dohm, J.M., Tanaka, K.L.,Hare, T.M., 2001c. Paleoerosional Map of the Thaumasia Region, Mars. In: s. Geologic Investigation Series I-2650 (Editor), Atlas of Mars: Thaumasia Region. U.S. Geological Survey.

Dohm, J.M., Williams, J.-P., Anderson, R.C., Ruiz, J., McGuire, P.C., Komatsu, G., Davila, A.F., Ferris, J.C., Schulze-Makuch, D., Baker, V.R., Boynton, W.V., Fairén, A.G., Hare, T.M., Miyamoto, H., Tanaka, K.L.,Wheelock, S.J., 2009. New evidence for a magmatic influence on the origin of Valles Marineris, Mars. J. Volcanol. Geoth. Res. 185(1-2), 12.

Evertsz, C.J., Berkner, K.,Berghorn, W., 1995. A local multiscale characterization of edges applying the wavelet transform, Proc. Nato A.S.I., Fractal Image Encoding and Analysis.

Fairén, A.G., Ruiz, J.,Anguita, F., 2002. An Origin for the Linear Magnetic Anomalies on Mars through Accretion of Terranes: Implications for Dynamo Timing. Icarus 160(1), 220.

Fassett, C.I.,Head III, J.W., 2008. The timing of valley network activity: constraints from buffered crater counting. Icarus 195, 61-89.

Fernández, C.,Anguita, F., 2007. Oblique rifting at Tempe Fossae. J. Geophys. Res. 112(E9), E09007.

Fournier, M.,Petit, C., 2007. Oblique rifting at oceanic ridges: Relationship between spreading and stretching directions from earthquake focal mechanisms. J. Struct. Geol. 29(2), 201.

Freeman, H., 1961. On the Encoding of Arbitrary Geometric Configurations. IEEE Trans. Electronic Computers EC-10, 260-268.

Frey, H.V., Roark, J.H., Shockey, K.M., Frey, E.L.,Sakimoto, S.E.H., 2002. Ancient lowlands on Mars. Geophys. Res. Lett. 29(10), 1384.

Fueten, F., Stesky, R.M.,MacKinnon, P., 2005. Structural attitudes of large scale layering in Valles Marineris, Mars, calculated from Mars Orbiter Laser Altimeter data and Mars Orbiter Camera imagery. Icarus 175(1), 68.

Gaber, A., Ghoneim, E., Khalaf, F.,El-Baz, F., 2009. Delineation of paleolakes in the Sinai Peninsula, Egypt, using remote sensing and GIS. J. Arid Environ. 73(1), 127.

Gagnon, J.-S., Lovejoy, S.,Schertzer, D., 2006. Multifractal earth topography. Nonlin. Processes Geophys. 13(5), 541-570.

Glennie, K.W., 1970. Chapter 4 - Wadis and Desert Fluviatile Sediments, Desert Sedimentary Environments. Elsevier, pp. 29.

Golombek, M.P., Anderson, F.S.,Zuber, M.T., 2001. Martian wrinkle ridge topography: Evidence for subsurface faults from MOLA. J. Geophys. Res. 106(E10), 23811.

Golombek, M.P.,Phillips, R.J., 2010. Mars tectonics. In: T.R. Watters and R.A. Schultz (Editors), Planetary Tectonics. Cambridge University Press, New York.

Hartmann, W.K., 2005. Martian cratering 8: Isochron refinement and the chronology of Mars. Icarus 174(2), 294.

Hartmann, W.K.,Neukum, G., 2001. Cratering Chronology and the Evolution of Mars. Space Sci. Reviews 96(1/4), 165-194.

Hauber, E.,Kronberg, P., 2001. Tempe Fossae, Mars: A planetary analogon to a terrestrial continental rift? J. Geophys. Res. 106(E9), 20587-20602.

Heipke, C. et al., 2007. Evaluating planetary digital terrain models - The HRSC DTM test. Planet. Space Sci. 55(14), 2173-2191.

Hiesinger, H.,Head III, J.W., 2002. Topography and morphology of the Argyre Basin, Mars: implications for its geologic and hydrologic history. Planet. Space Sci. 50(10-11), 939.

Howard, A.D., 1988. Groundwater sapping on Earth and Mars. In: A.D. Howard, R.C. Kochel and H.R. Holt (Editors), Sapping features of the Colorado Plateau, NASA Spec. Publ., SP-491, pp. 1-4.

Howard, A.D., Moore, J.M.,Irwin, R.P., III, 2005. An intense terminal epoch of widespread fluvial activity on early Mars: 1. Valley network incision and associated deposits. J. Geophys. Res. 110(E12S14).

Irwin, R.P., III, Howard, A.D., Craddock, R.A.,Moore, J.M., 2005. An intense terminal epoch of widespread fluvial activity on early Mars: 2. Increased runoff and paleolake development. J. Geophys. Res. 110(E12S15).

Johnson, C.L.,Phillips, R.J., 2005. Evolution of the Tharsis region of Mars: insights from magnetic field observations. Earth Planet. Sci. Lett. 230(3-4), 241.

Jones, T.A., 2006. MATLAB functions to analyze directional (azimuthal) data-I: Single-sample inference. Comput. Geosci. 32(2), 166.

Kim, J.R.,Muller, J.P., 2009. Multi-resolution topographic data extraction from Martian stereo imagery. Planet. Space Sci. 57(14-15), 2095.

Knighton, D., 1998. Fluvial forms and processes: a new perspective. Arnold Publication Series, New York, 383 pp.

Kobayashi, D.,Sprenke, K.F., 2010. Lithospheric Drift on Early Mars: Evidence in the Magnetic Field. Icarus In Press.

Koike, K., Nagano, S.,Kawaba, K., 1998. Construction and analysis of interpreted fracture planes through combination of satellite-image derived lineaments and digital elevation model data. Comput. Geosci. 24(6), 573-583.

Kumar, P.,Foufoula-Georgiou, E., 1997. Wavelet analysis for Geophysical applications. Rev. Geophys. 35(4), 385-412.

Lamb, M.P., Howard, A.D., Johnson, J., Whipple, K.X., Dietrich, W.E.,Perron, J.T., 2006. Can springs cut canyons into rock? J. Geophys. Res. 111(E7), E07002.

Landis, J.R.,Koch, G.G., 1977. The Measurement of Observer Agreement for Categorical Data. Biometrics 33(1), 159.

Lemiszki, P.J., Landes, J.D.,Hatcher Jr., R.D., 1994. Controls on hinge-parallel extension fracturing in single-layer tangential-longitudinal strain folds. J. Geophys. Res. 99(B11), 22,027–22,041.

Lemoine, F.G., Neumann, G.A., Chinn, D.S., Smith, D.E., Zuber, M.T., Rowlands, D.D., Rubincam, D.P.,Pavlis, D.E., 2001. Solutions for Mars Geophysical Parameters from Mars Global Surveyor Tracking Data. Eos (Fall supp.) 82(47), Abs. P42A-0545, F721.

Lillis, R.J., Frey, H.V., Manga, M., Mitchell, D.L., Lin, R.P., Acuña, M.H.,Bougher, S.W., 2008. An improved crustal magnetic field map of Mars from electron reflectometry: Highland volcano magmatic history and the end of the martian dynamo. Icarus 194(2), 575.

Lin, S.-Y., Muller, J.-P., Mills, J.P.,Miller, P.E., 2010. An assessment of surface matching for the automated co-registration of MOLA, HRSC and HiRISE DTMs. Earth Planet. Sci. Lett. In Press, Corrected Proof.

Little, S.A., 1994. Wavelet Analysis of Seafloor Bathymetry: An Example. In: A. Press (Editor), Wavelets in Geophysics. Efi Foufoula-Georgiou an Praveen Kumar (eds.), pp. 167-182.

Liu, C., Frazier, P.,Kumar, L., 2007. Comparative assessment of the measures of thematic classification accuracy. Remote Sensing of Environment 107(4), 616.

Malin, M.C., Bell Iii, J.F., Cantor, B.A., Caplinger, M.A., Calvin, W.M., Clancy, R.T., Edgett, K.S., Edwards, L., Haberle, R.M., James, P.B., Lee, S.W., Ravine, M.A., Thomas, P.C.,Wolff, M.J., 2007. Context Camera Investigation on board the Mars Reconnaissance Orbiter. J. Geophys. Res. 112(5), E05S04.

Mallat, S.,Zhong, S., 1992. Characterization of signals from multiscale edges. IEEE Trans. Pattern Anal. Mach. Intell. 14(7), 710-732.

Mallat, S.G., 1989. A theory for multiresolution signal decomposition: the wavelet representation. IEEE Trans. Pattern Anal. and Mach. Intel. 11(7), 674-693.

Mallat, S.G.,Hwang, W.L., 1992. Singularity detection and processing with wavelets. IEEE Trans. Inf. Theory 38(2), 617-643.

Mangold, N.,Ansan, V., 2006. Detailed study of an hydrological system of valleys, a delta and lakes in the Southwest Thaumasia region, Mars. Icarus 180(1), 75.

Mangold, N., Quantin, C., Ansan, V., Delacourt, C.,P., A., 2004. Evidence for Precipitation on Mars from Dendritic Valleys in the Valles Marineris Area. Science 305(5680), 78-81.

Mardia, K.V.,Jupp, P.E., 1999. Directional Statistics. Wiley, 430 pp.

Marzo, G.A., Roush, T.L., Lanza, N.L., McGuire, P.C., Newsom, H.E., Ollila, A.M.,Wiseman, S.M., 2009. Association of phyllosilicates and the inverted channel in Miyamoto crater, Mars. Geophys. Res. Lett. 36(11), L11204.

Masoud, A.,Koike, K., 2006. Tectonic architecture through Landsat-7 ETM+/SRTM DEM-derived lineaments and relationship to the hydrogeologic setting in Siwa region, NW Egypt. J. Afr. Earth. Sci. 45(4-5), 467-477.

McClay, K.,Dooley, T., 1995. Analogue models of pull-apart basins. Geology 23(8), 711-714.

McClay, K.R.,White, M.J., 1991. Analogue modelling of orthogonal and oblique rifting. Mar. Petrol. Geol. 12, 137-151.

McEwen, A.S., Eliason, E.M., Bergstrom, J.W., Bridges, N.T., Hansen, C.J., Delamere, W.A., Grant, J.A., Gulick, V.C., Herkenhoff, K.E., Keszthelyi, L., kirk, R.L., Mellon, M.T., Squyres, S.W., Thomas, N.,Weitz, C.M., 2007. Mars reconnaissance orbiter's high resolution imaging science experiment (HiRISE). J. Geophys. Res. 112(5), E05S02.

McQuarrie, N., 2004. Crustal scale geometry of the Zagros fold-thrust belt, Iran. J. Struct. Geol. 26(3), 519.

Mège, D.,Masson, P., 1996. Amounts of crustal stretching in Valles Marineris, Mars. Planet. Space Sci. 44(8), 749-782.

Mège, D.,Masson, P., 1996. Stress models for Tharsis formation, Mars. Planet. Space Sci. 44(12), 1471.

Montési, L.G.J.,Zuber, M.T., 2001. Crustal Thickness Control on Martian Wrinkle Ridge Spacing, Lunar and Planet. Sci. Conf., XXXII, abstract 1879, Houston.

Montési, L.G.J.,Zuber, M.T., 2003. Clues to the lithospheric structure of Mars from wrinkle ridge sets and localization instability. J. Geophys. Res. 108(E6), 5048.

Montgomery, D.R., Som, S.M., Jackson, M.P.A., Schreiber, B.C., Gillespie, A.R.,Adams, J.B., 2009. Continental-scale salt tectonics on Mars and the origin of Valles Marineris and associated outflow channels. GSA Bulletin 121(1/2), 117-133.

Morley, C., 2009. Geometry of an oblique thrust fault zone in a deepwater fold belt from 3D seismic data. J. Struct. Geol. 31(12), 1540.

Mueller, K.,Golombek, M., 2004. Compressional structures on Mars. Annu. Rev. Earth Planet. Sci 32, 435-464.

Mustard, J.F. et al., 2008. Hydrated silicate minerals on Mars observed by the Mars Reconnaissance Orbiter CRISM instrument. Nature 454(7202), 305.

Nahm, A.L.,Schultz, R.A., 2010. Evaluation of the orogenic belt hypothesis for the formation of the Thaumasia Highlands, Mars. J. Geophys. Res. 115(E04008).

Neukum, G., Jaumann, R.,Team, H.C.-I., 2004. HRSC: The High Resolution Stereo Camera of Mars Express. ESA Special Publications SP-1240.

Nimmo, F., 2000. Dike intrusion as a possible cause of linear Martian magnetic anomalies. Geology 28(5), 391-394.

Oakey, G., 1994. A structural fabric defined by topographic lineaments: Correlation with Tertiary deformation of Ellesmere and Axel Heiberg Islands, Canadian Arctic. J. Geophys. Res. 99(B10), 20311-20321.

Okubo, C.H.,Schultz, R.A., 2006. Variability in Early Amazonian Tharsis stress state based on wrinkle ridges and strike-slip faulting. J. Struct. Geol. 28(12), 2169.

Okubo, C.H., Shultz, R.A.,Stefanelli, G.S., 2004. Gridding Mars Orbiter Laser Altimeter data with GMT: effects of pixel size and interpolation methods on DEM integrity. Comput. Geosci. 30, 59-72.

Orosei, R., Bianchi, R., Coradini, A., Espinasse, S., Federico, C., Ferriccioni, A.,Gavrishin, A.I., 2003. Self-affine behavior of Martian topography at kilometer scale from Mars Orbiter Laser Altimeter data. J. Geophys. Res. 180(E4), 8023.

Parker, T., Gorsline, D., Saunders, R., Pieri, D.,Schneeberger, D., 1993. Coastal Geomorphology of the Martian Northern Plains. J. Geophys. Res. 98(E6), 11061-11078.

Peacock, D.C.P.,Sanderson, D.J., 1997. Geometry and development of normal faults. In: S. Sengupta (Editor), Evolution of geological structures in micro- to macro-scales. Chapman and Hall, London, pp. 27-46.

Persson, K.S., 2001. Effective indenters and the development of double vergent orogens: Insights from analogue sand models. In: H.A. Koyi and N.S. Mancktelow (Editors), Tectonic Modeling: A Volume in Honor of Hans Ramberg. Geological Society of America Memoir 193, Boulder, pp. 191-206.

Podwysocki, M.H., Moik, J.G.,Shoup, W.C., 1975. Quantification of geologic lineaments by manual and machine processing techniques, Proceedings of the NASA Earth Resources Survey Symposium, pp. 885-905.

Polit, A.T., Schultz, R.A.,Soliva, R., 2009. Geometry, displacement-length scaling, and extensional strain of normal faults on Mars with inferences on mechanical stratigraphy of the Martian crust. J. Struct. Geol. 31, 662-673.

Rãdoane, M., Rãdoane, N.,Dumitriu, D., 2003. Geomorphological evolution of longitudinal river profiles in the Carpathians. Geomorphology 50(4), 293.

Schlische, R.W., Withjack, M.O.,Eisenstadt, G., 2002. An experimental study of the secondary deformation produced by oblique-slip normal faulting. AAPG Bulletin 86 (5), 885-906.

Schultz, R.A., 2000. Fault-population statistics at the Valles Marineris Extensional Province, Mars: implications for segment linkage, crustal strains, and its geodynamical development. Tectonophysics 316(1-2), 169-193.

Schultz, R.A., 2000. Localization of bedding plane slip and backthrust faults above blind thrust faults: Keys to wrinkle ridge structure. J. Geophys. Res. 105(E5), 12035.

Schultz, R.A., 2002. Stability of rock slopes in Valles Marineris, Mars. Geophys. Res. Lett. 29(19), 1932.

Schultz, R.A., Okubo, C.H.,Wilkins, S.J., 2004. Displacement-Length Scaling of Faults on Earth, Mars, and Beyond, Lunar and Planet. Sci. Conf., XXXV, abstract 1157, League City.

Schultz, R.A.,Tanaka, K.L., 1994. Lithospheric-scale buckling and thrust structures on Mars: The Coprates rise and south Tharsis ridge belt. J. Geophys. Res. 99(E4), 8371-8385.

Silvestro, S., Fenton, L.K.,Vaz, D.A., 2010. Ripple migration and small modifications of active dark dunes in Nili Patera (Mars), Lunar and Planet. Sci. Conf. XLI, abstract 1820, The Woodlands.

Silvestro, S., Fenton, L.K., Vaz, D.A., Bridges, N.T.,Ori, G.G., 2010. Ripple migration and dune activity on Mars: Evidence for dynamic wind processes. Geophys. Res. Lett. in press.

Singh, B.P., 2003. Evidence of growth fault and forebulge in the Late Paleocene (~57.9-54.7 Ma), western Himalayan foreland basin, India. Earth Planet. Sci. Lett. 216(4), 717.

Skinner, J.A., Jr., Hare, T.M.,Tanaka, K.L., 2006. Digital Renovation of the Atlas of Mars 1:15,000,000-Scale Global Geologic Series Maps, Lunar and Planet. Sci. Conf., XXXVII, abstract 2331, League City.

Sleep, N.H., 1994. Martian Plate Tectonics. J. Geophys. Res. 99(E3), 5639-5655.

Smart, K.J., Ferrill, D.A.,Colton, S.L., 2006. En Echelon Segmentation of Wrinkle Ridges in Solis Planum, Mars, and Implications for Counter-Clockwise Rotation of Shortening Direction, Lunar and Planet. Sci. Conf., XXXVII, abstract 1966, League City.

Smith, D.E., Sjogren, W.L., Tyler, G.L., Balmino, G., Lemoine, F.G.,Konopliv, A.S., 1999. The Gravity Field of Mars: Results from Mars Global Surveyor. Science 286(5437), 94.

Smith, D.E. et al., 2001. Mars Orbiter Laser Altimeter: Experiment summary after the first year of global mapping of Mars. J. Geophys. Res. 106(E10), 23689.

Smith, M.J.,Wise, S.M., 2007. Problems of bias in mapping linear landforms from satellite imagery. Int. J. Appl. Earth Obs. Geoinf. 9(1), 65-78.

Smits, P.C., Dellepiane, S.G.,Schowengerdt, R.A., 1999. Quality assessment of image classification algorithms for land-cover mapping: a review and a proposal for a cost-based approach. Int. J. Remote Sens. 20(8), 1486.

Soille, P., 2002. Morphological Image Analysis - Principles and Applications. Sringer-Verlag, Berlin, 391 pp.

Solomon, S.C., Aharonson, O., Aurnou, J.M., Banerdt, W.B., Carr, M.H., Dombard, A.J., Frey, H.V., Golombek, M.P., Hauck, S.A., II, Head, J.W., III, Jakosky, B.M., Johnson, C.L., McGovern, P.J., Neumann, G.A., Phillips, R.J., Smith, D.E.,Zuber, M.T., 2005. New Perspectives on Ancient Mars. Science 307(5713), 1214-1220.

Solomon, S.C.,Head, J.W., 1982. Evolution of the Tharsis Province of Mars: the importance of heterogeneous lithospheric thickness and volcanic construction. J. Geophys. Res. 87(B12), 9755-9774.

Spagnuolo, M.G., Figueredo, P.H.,Ramos, V.A., 2008. Reinterpretation of Tractus Fossae region as an asymmetric rift system on Mars. Icarus 198(2), 318-330.

Sprenke, K.F.,Baker, L.L., 2000. Magnetization, Paleomagnetic Poles, and Polar Wander on Mars. Icarus 147(1), 26.

Stepinski, T.F.,Collier, M.L., 2004. Extraction of Martian valley networks from digital topography. J. Geophys. Res. 109(E11005).

Strayer, L.M., Erickson, S.G.,Suppe, J., 2004. Influence of growth strata on the evolution of fault-related folds e distinct element models. In: K.R. McClay (Editor), Thrust Tectonics and Hydrocarbon Systems. AAPG Memoir 82, pp. 413-437.

Tanaka, K.L., 1986. The Stratigraphy of Mars. J. Geophys. Res. 91(B13), E139-E158.

Tanaka, K.L., Skinner Jr, J.A., Crumpler, L.S.,Dohm, J.M., 2009. Assessment of planetary geologic mapping techniques for Mars using terrestrial analogs: The SP Mountain area of the San Francisco Volcanic Field, Arizona. Planet. Space Sci. 57(5-6), 510.

Taylor, B., Crook, K.,Sinton, J., 1994. Extensional transform zones and oblique spreading centers. J. Geophys. Res. 99(B10), 19707–19718.

Tchalenko, J.S., 1970. Similarities between shear zones of different magnitudes. Geological Society of America Bulletin 81, 1625-1640.

Tripathi, N.K., Gokhale, K.V.G.K.,Siddiqui, M.U., 2000. Directional morphological image transforms for lineament extraction from remotely sensed images. Int. J. Remote Sens. 21(17), 3281-3292.

Tron, V.,Brun, J.-P., 1991. Experiments on oblique rifting in brittle-ductile systems. Tectonophysics 188, 71-84.

Tso, B.,Mather, P.M., 2001. Classification methods for remotely sensed data. Taylor & Francis, New York, 352 pp.

Vaz, D.A., Barata, M.T.,Alves, E.I., 2006. Automatic detection and classification of fault scarps on MOLA data, Lunar and Planet. Sci. Conf., XXXVII, abstract 1571, League City.

Vaz, D.A., Barata, M.T., Alves, E.I.,Pereira, L.C.G., 2007. Interpretation of Tempe Terra (Mars) Tectonics Using a New Automatic Feature Extraction Technique, 13ª Conferência Portuguesa de Reconhecimento de Padrões, Lisboa.

Vaz, D.A., Di Achille, G., Barata, M.T.,Alves, E.I., 2008. Manual and automatic lineament mapping: comparing results, Lunar and Planet. Sci. Conf., XXXIX, abstract 1058, League City.

Venugopal, V., Roux, S.G., Foufoula-Georgiou, E.,Arneodo, A., 2006. Revisiting multifractality of high-resolution temporal rainfall using a wavelet-based formalism. Water Resour. Res. 42, W06D14.

Vidal, A., Mueller, K.,Golombek, M.P., 2003. Axial surface mapping of wrinkle ridges on solis planum, mars from mola topography: constraints on subsurface blind thrust geometry, Lunar and Planet. Sci. Conf. XXXIV, abstract, 1125, League City.

Watters, T.R., 1993. Compressional Tectonism on Mars. J. Geophys. Res. 98(E9), 17049-17060.

Watters, T.R., 2004. Elastic dislocation modeling of wrinkle ridges on Mars. Icarus 171(2), 284-294.

Webb, B.M.,Head, J.W., 2002. Noachian tectonics of Syria Planum and the Thaumasia Plateau, Lunar Planet. Sci. XXXIII, abstract 1358, Houston.

Wenzel, M.J., Manga, M.,Jellinek, A.M., 2004. Tharsis as a consequence of Mars' dichotomy and layered mantle. Geophys. Res. Lett. 31(4), L04702.

Wernicke, B., 1995. Low-angle normal faults and seismicity: A review. J. Geophys. Res. 100(B10), 20159-20174.

Wilkins, S.J.,Schultz, R.A., 2003. Cross faults in extensional settings: Stress triggering, displacement localization, and implications for the origin of blunt troughs at Valles Marineris, Mars. J. Geophys. Res. 108(E6), 5056.

Wise, D.U., 1982. Linesmanship and the practice of Linear Geo-art. Geol. Soc. Am. Bull. 93(9), 886-888.

Wu, J.E., McClay, k., Whitehouse, P.,Dooley, T., 2009. 4D analogue modelling of transtensional pull-apart basins. Mar. Petrol. Geol. 26, 1608-1623.

Wyrick, D.Y., Buczkowski, D.L., Bleamaster, L.F.,Collins, G.C., 2010. Pit Crater Chains Across the Solar System, Lunar and Planet. Sci. Conf. XLI, abstract 1533, The Woodlands.

Xu, S.-S., Nieto-Samaniego, A.F., Alaniz-Álvarez, S.A.,Velasquillo-Martínez, L.G., 2006. Effect of sampling and linkage on fault length and length-displacement relationship. Int. J. Earth Sci. 95(5), 841-853.

Zuber, M.T., Smith, D.E., Solomon, S.C., Muhleman, D.O., Head, J.W., Garvin, J.B., Abshire, J.B.,Bufton, J.L., 1992. The Mars Observer Laser Altimeter Investigation. J. Geophys. Res. 97(E5), 7781-7797.

Zuber, M.T., Solomon, S.C., Phillips, R.J., Smith, D.E., Tyler, G.L., Aharonson, O., Balmino, G., Banerdt, W.B., Head, J.W., Johnson, C.L., Lemoine, F.G., McGovern, P.J., Neumann, G.A., Rowlands, D.D.,Zhong, S., 2000. Internal Structure and Early Thermal Evolution of Mars from Mars Global Surveyor Topography and Gravity. Science 287(5459), 1788.

8 Annexes

Annex 1

Classified lineament map of the Eastern Thaumasia region.

Annex 2

Oblique perspective of the Eastern Thaumasia region. Some of the mapped and classified lineaments were overlaid on MOLA elevation data. See Annex 1 for a map view.

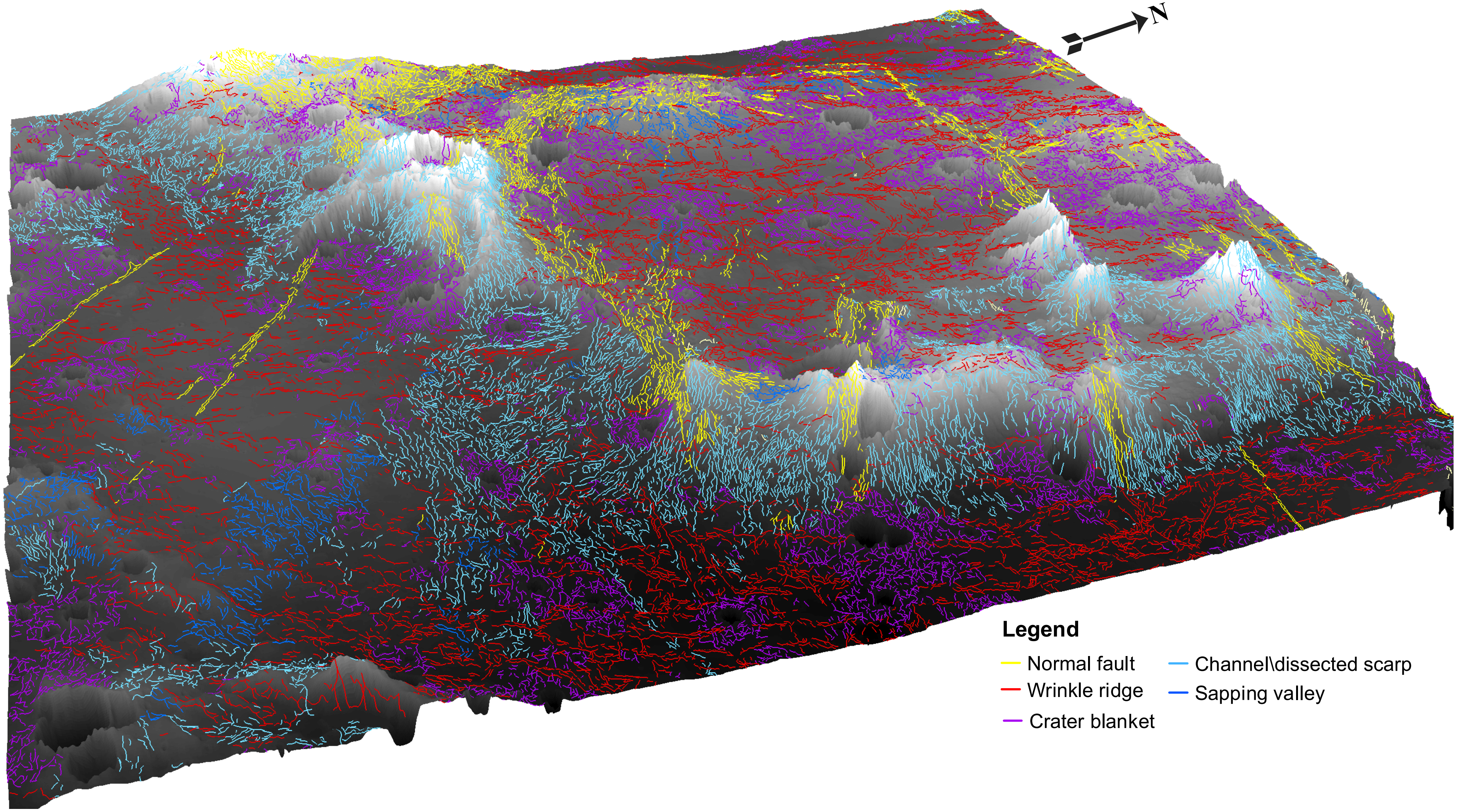
N
Legend
Normal fault
Wrinkle ridge
Crater blanket
Channel\dissected scarp
Sapping valley